

REPORT DOCUMENTATION PAGE

1a. REPORT SECURITY CLASSIFICATION
Unclassified

1b. RESTRICTIVE MARKINGS

AD-A210 084

3. DISTRIBUTION/AVAILABILITY OF REPORT
Approved for public release, distribution unlimited

5. MONITORING ORGANIZATION REPORT NUMBER(S)

F08671-8800036 AFOSR TR 33-0084

6a. NAME OF PERFORMING ORGANIZATION
Carnegie Mellon University6b. OFFICE SYMBOL
(If applicable)7a. NAME OF MONITORING ORGANIZATION
AFOSR6c. ADDRESS (City, State, and ZIP Code)
Carnegie Mellon University
Pittsburgh, PA 152137b. ADDRESS (City, State, and ZIP Code)
Bolling AFB
Washington, D.C. 20332-64488a. NAME OF FUNDING/SPONSORING
ORGANIZATION Air Force Office
of Scientific Research8b. OFFICE SYMBOL
(If applicable)
AFOSR/NA9. PROCUREMENT INSTRUMENT IDENTIFICATION NUMBER
AFOSR No. 86-01428c. ADDRESS (City, State, and ZIP Code)
Bolling AFB
Washington, D.C. 20332-6448

10. SOURCE OF FUNDING NUMBERS

PROGRAM
ELEMENT NO.
61102FPROJECT
NO.
Q302TASK
NO.
/B2WORK UNIT
ACCESSION NO.

11. TITLE (Include Security Classification)

The Effect of Transients on Crack Tip Stress Fields During Thermal Fatigue Loading (u)

12. PERSONAL AUTHOR(S)

Cunningham, S. E., and Griffin, J. H.

13a. TYPE OF REPORT

Final

13b. TIME COVERED

FROM 4/1/86 TO 3/31/89

14. DATE OF REPORT (Year, Month, Day)

89 April 25

15. PAGE COUNT

121

16. SUPPLEMENTARY NOTATION

17. COSATI CODES

18. SUBJECT TERMS (Continue on reverse if necessary and identify by block number)

FIELD	GROUP	SUB-GROUP

Thermal mechanical fatigue, fracture mechanics, thermal stress, thermal transients. (JES) ↴

19. ABSTRACT (Continue on reverse if necessary and identify by block number)

A method is developed for evaluating the effect of cyclic thermal loading on crack tip stress fields. In its development, advantage is taken of the periodic nature of fatigue loading and only harmonic loadings are considered. Formulating the problem in this way permits the extraction of time as an explicit variable and replaces its role with a dependence on the frequency of the thermal loading. The means for evaluating the effect of thermal transients on crack tip stress fields is the stress intensity factor which is calculated from numerically defined stress and displacement fields using a path independent integral. Results obtained indicate that stress intensity factors of cracked components exposed to thermal fatigue conditions have a significant dependence on the frequency of the thermal cycle and the crack geometry. Numerical estimates for Mode I thermal stress intensity have been obtained for the case of a titanium alloy that was heated using intense light sources. It was found that they can be as high as 25 percent of the critical Mode I mechanical stress intensity. The approach is also used to consider direct resistance heating of specimens. Electrical resistance heating induces a singularity in the heat source term at the crack tip. Unlike

20. DISTRIBUTION/AVAILABILITY OF ABSTRACT

 UNCLASSIFIED/UNLIMITED SAME AS RPT. DTIC USERS

21. ABSTRACT SECURITY CLASSIFICATION

Unclassified

22a. NAME OF RESPONSIBLE INDIVIDUAL

J. H. Griffin

22b. TELEPHONE (Include Area Code)

412/268-3860

22c. OFFICE SYMBOL

NH

19. ABSTRACT (Continued)

heating with light sources, the stress intensities induced by resistance heating increase with the frequency of the thermal loading and may become quite large at higher frequencies.

The approach is extended to composite materials. In composite materials stresses at the crack tip can be induced by thermal transients (in the same manner as homogeneous materials) and also by changes in temperatures which are uniform in space because of differences in the thermal expansion rates of the constituents (unlike homogeneous materials). The relative importance of these two mechanisms is investigated in the context of ceramic composites.

AIR FORCE OFFICE OF SCIENTIFIC RESEARCH (AFSC)
1989
Approved for public release and is
unlimited. AFR 190-12.
REF ID: A6429
AFOSR
Information Division

AFOSR-TK-89-0684

Approved for public release;
distribution unlimited.

THE EFFECT OF TRANSIENTS ON CRACK TIP STRESS FIELDS DURING THERMAL FATIGUE LOADING

(AFOSR-86-0142)

FINAL REPORT

Submitted to
Air Force Office of Scientific Research
Bolling Air Force Base
Washington, D.C. 20332

by

J. H. Griffin and S. E. Cunningham
Department of Mechanical Engineering
Carnegie Mellon University
Pittsburgh, Pennsylvania 15213

February, 1989



Accession For	
NTIS CRAZI	<input checked="" type="checkbox"/>
DTIC TAB	<input type="checkbox"/>
Unpublished	<input type="checkbox"/>
Justification	
By	
Distribution	
Comments	
Approved by	
Date	
Comments	

A-1

TABLE OF CONTENTS

Title	page
LIST OF FIGURES	iii
LIST OF TABLES	v
I. INTRODUCTION	1
II. TRANSIENT UNIFORM HEAT SOURCE IN A CENTER CRACKED PLATE	6
III. EXTENSIONS OF THE UNIFORM HEAT SOURCE PROBLEM	35
IV. ELECTRIC POTENTIAL HEAT SOURCE IN A CENTER- CRACKED PLATE	51
V. IMPLICATIONS FOR FATIGUE TESTING	66
VI. A PILOT STUDY OF COMPOSITE MATERIALS	71
VII. CONCLUSIONS AND RECOMMENDATIONS	97
REFERENCES	98
APPENDIX A. HEAT SOURCE INDUCED BY AN ELECTRIC CURRENT IN A CRACKED PLATE	101
APPENDIX B. GRIDS FOR FINITE ELEMENT ANALYSIS	107
APPENDIX C. COMPLEMENTARY EIGENFUNCTIONS FOR A CRACK .	116
APPENDIX D. WEIGHTS AND ABSCISSAS FOR THE SQUARE ROOT GAUSS-TYPE QUADRATURE	118

LIST OF FIGURES

	Title	page
1.	Center crack geometry of the posed problem.	28
2.	Magnitude of the temperature field induced by uniform heating	29
3.	Integration contour for the path independent integral.	30
4.	Integration paths for the test problems.	31
5.	Amplitude of the stress intensity normalized by the crack tip temperature for the uniform heating case.	32
6.	Amplitude of the stress intensity as a function of crack tip temperature.	33
7.	Amplitude of the stress intensity as a function of crack tip temperature.	34
8.	Edge-crack geometry.	50
9.	Stress intensity normalized by the temperature at the crack tip.	60
10.	Magnitude of the electric potential temperature field along the x-axis for different normalized frequencies.	61
11.	Amplitude of the stress intensity as a function of the crack tip temperature.	62
12.	Amplitude of the stress intensity as a function of the crack tip temperature.	63
13.	Stress intensity normalized by crack tip temperature for $a/W=1/3$.	64
14.	Stress intensity normalized by crack tip temperature for $a/W=1/6$.	65
15.	Geometry of the composite problem.	86
16.	Dependence of the eigenvalue on material constants.	87
17.	Traction conditions for the test problem	88
18.	Temperature magnitude as a function of dimensionless frequency and diffusivity ratio for the composite problem.	89
19.	Variation of the crack tip temperature with frequency for the composite problem.	91
20.	Stress intensity factor variation with frequency and diffusivity ratio.	92
21.	Stress intensity variation with expansion ratio for the degenerate case.	93

22.	Variation of the stress intensity and eigenvalue with ratio of elastic modulus.	94
23.	Stress intensity variation with frequency for composites of Titanium and SiC.	95
24.	Stress intensity variation with frequency for composites of Glass and SiC.	96
A1.	Flow past an infinite cascade of plates.	106
B1.	Finite element grid for homogeneous stress analysis, coarse.	109
B2.	Finite element grid for homogeneous stress analysis, medium.	110
B3.	Finite element grid for homogeneous stress analysis, fine.	111
B4.	Finite element grid for composite stress analysis, coarse.	113
B5.	Finite element grid for composite stress analysis, medium.	114
B6.	Finite element grid for composite stress analysis, fine.	115

LIST OF TABLES

	Title	page
1.	Loading conditions and reported stress intensity solutions for test problems.	24
2.	Results of test problem calculations for center-crack geometry.	25
3.	Dimensionless stress intensity factor and temperature field results for center-crack geometry, end temperature prescribed non-zero.	26
4.	Dimensionless stress intensity factor and temperature field results for center-crack geometry, uniform heat source.	27
5.	Loading conditions and reported stress intensity solutions for test problems.	42
6.	Results of test problem calculations using edge-crack geometry.	43
7.	Dimensionless stress intensity factor results for the sinusoidally varying end temperature, edge-crack geometry.	44
8.	Dimensionless stress intensity factor results for the sinusoidally varying uniform heat source, edge-crack geometry	45
9.	Dimensionless stress intensity factor and temperature field results, $a/W = 1/6$ for the sinusoidally varying heat source, center crack geometry	46
10.	Dimensionless stress intensity factor and temperature field results, $L/W = 4.0$ for the sinusoidally varying heat source, center crack geometry	47
11.	Dimensionless stress intensity factor results for the antisymmetric problem of sinusoidally varying end temperature, center-crack geometry.	48
12.	Dimensionless stress intensity factor results for the antisymmetric problem of sinusoidally varying uniform heat source, center-crack geometry	49
13.	Convergence check of finite difference solution for singular heat source	57
14.	Dimensionless stress intensity factor and temperature field results, electric potential heat source	58
15.	Dimensionless stress intensity factor and temperature field results, electric potential heat source, $a/W = 1/6$	59
16.	Material properties for example composites.	83
17.	Ratios of material properties and the associated eigenvalue for example	

	composites.	84
18.	Stress intensity increase at a frequency of 1 cycle/min for example composites	85
B1.	Finite element grids for the homogeneous problems.	108
B2.	Finite element grids for the composite problems.	112

I. INTRODUCTION

This report discusses the work accomplished during the Air Force Office of Scientific Research Grant AFOSR-86-0142. There were three primary objectives of this work. The first was to develop a method for estimating the stress intensity factors induced by temperature gradients in thermo-mechanical fatigue. The second was to use this method to estimate the importance of the thermal contribution relative to the mechanical contribution. To do this, we take into account several factors, for example, the dependence of the stress intensity on the frequency, the crack geometry and the mode of thermal loading (i.e. heat lamp vs. electric resistance heating). The final goal was to extend the developed method to composite material applications and perform a preliminary study to assess the relative importance of thermal transient effects in composite materials. All these objectives have been met and a detailed discussion follows.

Gas turbine engine components typically undergo complex mechanical and thermal operating conditions which may give rise to crack propagation and eventual fatigue failure. Although the role of mechanical loading in fatigue has been investigated, it is of fundamental importance to understand how cyclic thermal conditions affect crack growth and fatigue failure. This study is an attempt to estimate the importance of cyclic thermal loads in thermo-mechanical fatigue.

Laboratory tests are currently used to assess the safe thermomechanical fatigue limits of engine components. However, there are three aspects of the thermal loading which potentially vary widely between laboratory simulations and actual in-service conditions. These are the frequency of the thermal cycle, the symmetry of the temperature field about the crack axis, and the geometry of the initial crack.

The frequency of the thermal cycle is related to the heating rate which may be significantly higher or lower in engine environments than in fatigue testing situations. Currently, heating rates in fatigue testing are limited to a level which is believed to not induce significant thermal stresses at the crack tip. Consequently, it is unknown how accurately results of stress intensity testing can be applied to engine fatigue standards. Determining the variation of the stress field with frequency provides a means of accounting for the high heating rates in both engine components and lab specimens thus improving the

validity and accuracy of the test method. Further, having a means to account for rapid thermal cycling also may provide an economic benefit in that it may be possible to increase the rate at which specimens are cycled.

Test specimens are usually symmetrically heated with respect to the crack axis. This is a fundamental difference from what happens to engine components in that cracks are usually subjected to temperature gradients that may induce significant thermal stresses at the crack tip. The reason is related to the thermal boundary conditions specified along the axis of the crack tip. The symmetry condition on this axis is identical to the insulation condition of the open crack: the normal gradient of the temperature is zero. The antisymmetry condition, on the other hand, is that the temperature itself is zero along this boundary. This gives rise to a discontinuity in the boundary condition at the crack tip and results in a thermal field which changes as the crack grows. The effect of this thermal field/crack interaction is currently unaccounted for in fatigue analysis.

The effect of geometry on stress intensity is also being investigated. Cracks can be located on the specimen edge or in its center. The important distinction in the crack location is that the edge cracked component corresponds to a simply-connected region while the center cracked component corresponds to a multiply-connected region. Thus, an additional aspect to be investigated is the effect of geometry on stress intensity.

The means for evaluating the importance of each of these phenomena is the stress intensity factor, K . The stress intensity factor is a quantitative measure of the strength of the elastic stress field near the crack tip and is of interest because of the general belief that it is a dominant parameter in controlling crack instability. We can use the standard definitions of stress intensity factor for thermoelastic problems since it has been shown that the local behavior of the thermal stresses near the crack tip is the same as the behavior of mechanical stresses, that of the $r^{1/2}$ singularity [1].

The first work dealing with two-dimensional stress fields associated with cracks was published by Florence and Goodier [2] and Sih [1]. The method of complex representation of the elastic state was used to derive the theoretical stress intensity factors in infinite two-dimensional cracked regions subjected to uniform heat flow for both the symmetric and antisymmetric problems. The expressions derived in [1] for the thermoelastic crack-tip stress field are identical to those given by Irwin [3] for traction boundary condition problems. It is noted that the real parts of the crack-tip stress field are identical to the singular terms of the Williams [4] eigenfunction relations.

Several investigators have used stress intensity factors in studying problems of thermoelastic stress intensity in cracked regions subjected to nonuniform temperature

fields. Early work of Konishi and Atsumi [5] and of Sekine [6,7,8] used singular integral equations to estimate the normal thermal stress components on the crack plane in semi-infinite plates with uniform heat flow perpendicular to the crack. From these solutions the stress intensity factors were evaluated. This method has also been used by Shail [9] and Das [10] for determining stress intensity factors in an externally cracked infinite solid for both even and odd temperature distributions, by Das [11] for cracked infinite cylinders with constant temperature and by Herrmann and Kuemmerling[12] for cracked infinite cylinders with a point source of heat.

Because of the finite domains of the present analysis, however, solution by these methods is not appropriate and an alternative way to evaluate the stress intensity factor from numerically defined stress fields is required. Path independent integrals have been developed to estimate the stress intensity factors at cracks and notches when numerical approaches, such as the finite element method, are used to compute singular stress distributions. The path independent integrals offer the distinct advantage that the errors in the analysis stem only from the numerical approximations used and not from additional sources [13] and so offer a relatively accurate result with modest computational effort.

Several path independent integrals for thermoelastic stress problems have been developed. The integral of Gurtin [14] consists of the well-known J-integral for isothermal stress fields and three additional terms which relate to the temperature field. However, the development of the integral relies on specifying the temperature field to be symmetric about the crack axis and zero along the crack surfaces, requirements that are not in general met. Wilson and Yu [15] have developed an integral similar to the J-integral which consists of an additional area integral containing, not only the temperature field but also the gradient of the temperature field. Aoki et al. [16,17,18] have derived another set of path independent integrals for thermoelastic problems. As in the integral of Wilson and Yu, each of these integrals require area integration of the gradient of the temperature distribution, implying that a highly accurate temperature solution near the crack tip is necessary in order to evaluate the stress intensity factor precisely. Finally, Kuo and Riccardella [19] have developed line integrals for thermoelastic stress fields which eliminate the need for area integration but in doing so, restrict the problem to one where no body forces or distributed heat sources are permitted.

The appropriate integral for our work follows from the development of the H-integral by Sinclair, Okajima and Griffin [13] and takes into account the Duhamel-Neumann analogy (for example, [20]) for modeling the thermoelastic problem. The path-independent integral consists of the H-integral and an additional area integral containing the

temperature field. Although the derived integral loses some computational efficiency through calculation of the area integral, it does not require the gradient of the temperature distribution. Since our temperature distributions are, in general, numerically determined, calculating thermal gradients would be prohibitively inaccurate.

In our approach to studying thermal fatigue loading, we concentrate on the effect that the thermal cycle has on thermally induced crack tip stresses. Since any periodic function can be represented exactly as a Fourier series of harmonic functions, we assume all thermal cycles are harmonic in time. By this assumption, we can consider the derived solutions to the harmonic thermal cycles as Fourier components of the true solution to general thermal cycling cases. The actual solution may be approximated by its fundamental harmonic or as closely as desired by adding higher frequency components.

Considering only sinusoidal thermal loadings provides the advantage that we can eliminate time as an explicit variable. Without time as a variable, there is no need to track stress fields as a function of time. Instead, its role is replaced by the parametrical dependence of frequency. With this, we can calculate stress intensity factors for sinusoidal thermal loadings as a function of frequency of the thermal cycle.

The thermal loadings we consider are selected after careful evaluation of fatigue testing. We choose simple loading conditions which, when combined through linear superposition, describe more complex loading cases. The goal in our approach is to develop stress intensity solutions to simple problems that can be combined later to represent stress intensities of a large variety of fatigue loading cases. With this, we have outlined an approach to calculating thermal stress intensities as functions of frequency in fatigue loading. We evaluate the importance of the stress intensity by comparing it to those induced in mechanical fatigue, for example, the results of Wilson and Warren [21].

We begin in Section 2 by addressing the basic problem of a symmetrically and uniformly heated center-cracked fatigue specimen, presenting the formulation, a discussion of the solution methods, and the results of this simple analysis. In Section 3, we consider extensions of the basic problem. First, we investigate some geometrical variations, considering both edge-cracked regions and crack- and sample-length scaling. Secondly, we address the issue of antisymmetric fatigue heating and the importance of Mode II stress intensity factors. Because specimen heating is often accomplished by applying an electric potential to the specimen, we investigate this mode of heating in Section 4. Evaluating electric potential heating is important because it induces a singular heat source at the crack tip which may serve to give a much different dependence on frequency than the regular heating fields studied in Sections 2 and 3. In Section 5, we close the analysis of the

homogeneous linear elastic material by investigating the implications the results obtained have in actual fatigue testing.

Finally, in the interest of understanding the effects of thermal transients in composite materials, we extend our approach of fatigue analysis to bimaterial composites. In Section 6 we discuss the fundamentals of a pilot study performed to investigate the rudimentary effects of diffusivity and thermal expansion mismatches in bimaterial composites in which cracks occur normal to the interface. This particular geometry was selected for initial investigation because of its physical interest: it can correspond to the problem of a crack turning at or penetrating the interface.

The intent of the composite analysis is to perform a parametrical study to establish the importance of differences in thermal diffusivity relative to differences in the thermal expansion and elastic modulus for composite materials. These effects may be especially important in materials with low diffusivity such as ceramic composites. Our resulting improvement in understanding these mechanisms should allow the development of composites with improved durability for high temperature applications.

II. TRANSIENT UNIFORM HEAT SOURCE IN A CENTER CRACKED PLATE

Formulation

In order to investigate the effects of transient thermal loadings on crack tip stress fields, we formulate the following problem. Our analysis is directly applicable to fatigue testing so we choose a geometry which represents typical fatigue test specimens. This is the center-cracked plate pictured in Figure 1. Geometrical symmetry permits analysis of only the upper right quadrant of the center-cracked plate, the region shaded in the figure. For simplicity, we assume the plate to be in a state of plane strain. The region, R , of our analysis, then, is rectangular in the x, y plane and is defined by :

$$R = \{x, y \mid 0 \leq x \leq W, 0 \leq y \leq L\} \quad (1)$$

where R is assumed to be homogeneous, isotropic and linear elastic. The boundary of R is denoted by ∂R and contains the crack of length a along the line

$$0 < x < a, y = 0 \quad (2)$$

We seek then, the two-dimensional thermoelastic stress vector $\sigma = (\sigma_x, \sigma_y, \tau_{xy})$ and displacement vector $u = (u, v)$ satisfying the plane-strain uncoupled quasi-static equations of thermoelasticity. These equations are derived by neglecting the effects of elasticity on the temperature and ignoring the inertial term in the equation of motion. The result is the degeneration of heat conduction and elasticity into two separate problems. With these simplifying assumptions, the temperature field is determined solely by conduction and the stress and displacement fields are computed for each instantaneous temperature distribution according to the equations of linear thermoelasticity.

The temperature distribution, T , varies with time, t , and satisfies the planar heat conduction equation in R :

$$\nabla^2 T(x, y, t) = \frac{1}{D} T_n(x, y, t) - H(x, y, t) \quad (3)$$

where ∇^2 is the Laplacian operator in two dimensions, D , the thermal diffusivity, is equal to the thermal conductivity divided by the heat capacity and the density, and the subscript following a comma denotes differentiation with respect to that variable. The forcing function $H(x,y,t)$ is a net distributed heat source per unit area term which takes into account the effects of radiation and convection from the surface. The boundary conditions imposed on the temperature field are that the plate is insulated along the right edge and along the crack faces, and the temperature is symmetric along the y -axis and along the uncracked portion of the x -axis. Since the conditions of insulation and symmetry are identical (the normal temperature gradient equals zero) these conditions may be stated:

$$\begin{aligned} T_{,x} &= 0 \text{ on } x = W \quad (0 < y < L) \\ T_{,x} &= 0 \text{ on } x = 0 \quad (0 < y < L) \\ T_{,y} &= 0 \text{ on } y = 0 \quad (0 < x < W) \end{aligned} \tag{4}$$

Along the remaining edge of the boundary, a spatially constant temperature is imposed:

$$T(x,y,t) = \Theta_0(t) \text{ on } y = L \quad (0 < x < W) \tag{5}$$

The equations of uncoupled quasi-static linear thermoelasticity are identical to those of linear elasticity with the exception of the stress displacement law. This being true, the stress field obeys the equations of equilibrium in the absence of a body force field, which hold in the region R :

$$\begin{aligned} \sigma_{x,x} + \tau_{xy,y} &= 0 \\ \sigma_{y,y} + \tau_{xy,x} &= 0 \end{aligned} \tag{7}$$

The stress and displacement vectors must also satisfy the plane-strain stress-displacement relations in R :

$$\begin{aligned} \sigma_x &= \frac{2\mu}{(1-2\nu)} [(1-\nu)u_{,x} + \nu v_{,y}] - \beta T \\ \sigma_y &= \frac{2\mu}{(1-2\nu)} [(1-\nu)v_{,y} + \nu u_{,x}] - \beta T \\ \tau_{xy} &= \mu(u_{,y} + v_{,x}) \end{aligned} \tag{8}$$

where β combines material constants in the form, $\beta = \alpha E / (1 - 2v)$ for the plane strain case ($\beta = \alpha E / (1 - v)$ for the plane stress case) and the constants α, E, v , and μ represent the coefficient of linear thermal expansion, the elastic modulus, Poisson's ratio, and the shear modulus, respectively.

The boundary conditions for the thermoelastic problem are: traction-free conditions on the upper and right edges of the region and along the crack face,

$$\begin{aligned}\sigma_y &= 0, \tau_{xy} = 0 \text{ on } y = L \quad (0 < x < W) \\ \sigma_x &= 0, \tau_{xy} = 0 \text{ on } x = W \quad (0 < y < L) \\ \sigma_y &= 0, \tau_{xy} = 0 \text{ on } y = 0 \quad (0 < x < a)\end{aligned}\tag{9}$$

and symmetry conditions along the y-axis and along the x-axis in the region not containing the crack,

$$u = 0 \text{ and } \tau_{xy} = 0 \text{ on } x = 0 \quad (0 < y < L)\tag{10}$$

$$v = 0 \text{ and } \tau_{xy} = 0 \text{ on } y = 0 \quad (a < x < W).\tag{11}$$

The means for evaluating the importance of transient temperature fields on crack tip stress fields is the stress intensity factor, K . The stress intensity factor is a quantitative measure of the strength of the elastic stress field near the crack tip and is defined for the crack-opening mode, Mode I, by the relation

$$K_I = \lim_{x \rightarrow a^+} \sqrt{2\pi(x-a)} \sigma_y \quad \text{on } y = 0\tag{12}$$

and for the edge-sliding mode, Mode II, by the relation

$$K_{II} = \lim_{x \rightarrow a^+} \sqrt{2\pi(x-a)} \tau_{xy} \quad \text{on } y = 0\tag{13}$$

Considering transient temperature fields typically implies that the stress and displacement vectors, and consequently, the stress intensity factor must be computed at instantaneous points. Herein we impose a fundamental condition: we consider only temperature fields which vary sinusoidally in time. In essence, the temperature field, $T(x,y,t)$, is taken as the sum of harmonic components in which ω is the frequency of the

excitation and T_s and T_c are the spatially varying magnitudes of their respective components:

$$T(x,y,t) = T_s(x,y) \sin \omega t + T_c(x,y) \cos \omega t \quad (14)$$

By representing the temperature in this form and considering only harmonic heat sources, $H(x,y,t) = h(x,y) \cos \omega t$ ¹, we benefit in two ways. First, the need for instantaneous computations is eliminated since time is no longer an explicit variable. This is because we calculate the stress and displacement fields induced by each of the spatial functions, $T_s(x,y)$ and $T_c(x,y)$, independently. Then, if K_s and K_c are the resultant stress intensity factors associated with these fields, respectively, the total stress intensity factor induced by the temperature field $T(x,y,t)$ is also obtained by harmonic sum:

$$K(\omega,t) = K_s(\omega) \sin \omega t + K_c(\omega) \cos \omega t \quad (15)$$

Secondly, because any periodic function can be represented exactly by Fourier series of sinusoidal functions, solutions derived with this approach may be considered as Fourier components of a solution to a more complex periodic temperature profile. This is important in fatigue studies where actual thermal cycling experiments may not always utilize sinusoidal temperature fields and the in-service conditions the experiments are intended to simulate may also be more complex than harmonic functions.

The stress intensity factors in (15) are denoted as functions of the frequency. Eliminating time explicitly requires its role to be replaced by the parametrical dependence on ω . This is because substitution of (14) into (3) results in coupled equations for T_s and T_c in which frequency appears as a parameter:

$$\begin{aligned} \nabla^2 T_c &= \frac{\omega}{D} T_s - h(x,y) \\ \nabla^2 T_s &= -\frac{\omega}{D} T_c \end{aligned} \quad (16)$$

A range of frequencies must therefore be analyzed before a general solution can be obtained.

¹If the heat source has a sine component as well, its contribution may be readily computed by introducing a 90 degree phase shift in the solution computed here.

Problem definition

The goal of this analysis is to form a basis for understanding how transient temperature fields affect stress fields in a region containing a crack. A desired result would be to apply solutions to fatigue testing cases so that we can make estimates of the importance of the thermal field with respect to mechanically induced stresses the specimen may experience. The trouble with this is that many different variations in loadings are generally used and it would be impossible to explicitly calculate temperature fields corresponding to each case. Instead, we choose to use the linearity of the stress and displacement equations and hence their vector solutions in defining the loading conditions to be investigated. By carefully choosing specific thermal loading cases and obtaining their stress field solutions, superposition may be used to represent a variety of cases by linear combination of the conditions and so more general solutions may be obtained.

In order to define the appropriate loading conditions, we examine fatigue testing a little more closely. In general, two methods of heating are utilized to cycle specimen temperatures. These are a heat lamp with forced air cooling, and direct resistance heating with grip cooling. Grips hold the specimens in place and often extend the width of the specimen at distances considered remote from the crack. In order to account for heat conduction out of the crack region, two alternatives are considered. First, it would be possible to consider conduction conditions on these ends in which the heat flux is proportional to the temperature at the ends. However, this approach would require varying the proportionality constant depending on the grip configuration and would consequently require a number of simulations in order to represent the entire range of possible conduction conditions found in practice. Instead, we consider the condition in which no heat sources are applied and the temperature at the end is held spatially constant, varying only harmonically in time. Then, rather than attempting to apply heat flux proportionality constants to the test rig configurations, we need only measure the temperature at the grip location, scale the constant temperature solution appropriately and add it to the solution corresponding to the proper mode of heating. Thus, only one solution to account for boundary conduction needs to be obtained for each frequency.

In particular, we will first investigate in detail the case of symmetrically heating a specimen by heat lamp and cooling it by forced air. In later chapters, other thermal loading cases will be considered for comparison. This first method of heating can be modeled by a sinusoidally varying uniform heat source, $H(x,y,t) = h_0 \cos \omega t$, where h_0 is spatially constant. So, in addition to the constraints imposed on the stress and displacement vectors

in Equations (1) through (11), the following conditions will be satisfied by the temperature field:

$$a. h(x,y) = 0, \Theta_0(t) = T_0 \cos \omega t \quad (17)$$

$$b. h(x,y) = h_0, \Theta_0(t) = 0 \quad (18)$$

where h_0 and T_0 are constants, $h(x,y)$ is the heat source distribution of Equation (16) and $\Theta_0(t)$ is the edge temperature of Equation (5).

With this we have developed an approach for establishing the effect of thermal transients on the mechanical state of an elastic region containing a crack. The temperature solutions are spatially one-dimensional and are obtained in closed form. The stress and displacement fields are numerically calculated with finite element methods. A path independent integral developed for thermoelastic problems is used to compute the stress intensity factor.

Solutions to the Temperature Fields

The closed form representation of temperature for the case with temperature varying as $T_0 \cos(\omega t)$ on the boundary $y=L$ is derived by standard separation of variables method and by invoking the Duhamel integral [22]:

$$\frac{T(y,t)}{T_0} = \cos \omega t + 4 \omega \sum_{n=1,3,5}^{\infty} \frac{(-1)^{(n-1)/2}}{n\pi} \frac{\cos \frac{n\pi y}{2L}}{(\lambda_n^2 + \omega^2)} (\lambda_n \sin \omega t - \omega \cos \omega t) \quad (19)$$

A similar expression for the temperature in which a uniform heat source varying as $\cos(\omega t)$ is applied internally and the temperature at the end is zero is obtained by variation of parameters method [22]:

$$\frac{T(y,t)}{h_0 L^2} = -4 \frac{D}{L^2} \sum_{n=1,3,5}^{\infty} \frac{(-1)^{(n-1)/2}}{n\pi} \frac{\cos \frac{n\pi y}{2L}}{(\lambda_n^2 + \omega^2)} (\omega \sin \omega t + \lambda_n \cos \omega t) \quad (20)$$

in each case, λ_n are the eigenvalues,

$$\lambda_n = \left(\frac{n\pi}{2L} \right)^2 D \quad , \quad n = 1, 3, 5, \dots \quad (21)$$

Figure 2 graphically depicts the temperature field according to (20) for various frequencies.

Solution to the Thermoelastic Stress Fields

The stress and displacement fields are calculated using the finite element method which is an indirect approach to solving partial differential equations describing a desired quantity in a continuum. In this case, the desired quantity is the stress/displacement field and the continuum is the linear elastic solid of the two-dimensional geometry of Figure 1. In theory, the continuum is divided into a number of 'finite elements'. An approximation function (algebraic polynomial) is chosen to represent the variation of the desired quantity at discrete points (nodes) within the element and on its boundary. The number of nodes for each element determines the order of the polynomial. By using the physical properties of the continuum and the appropriate physical laws, a set of simultaneous equations is obtained. Solution of these equations results in a representation of the desired quantity at nodal locations within the solid.

The ABAQUS finite element code is a packaged program designed for the numerical modeling of structural response. Its features include its ability to perform linear and nonlinear stress analyses; static and dynamic analyses; and coupled and uncoupled heat transfer analyses. Full control of the finite element selection is afforded the user. The code is capable of handling elements with up to 27 nodes for the three-dimensional stress analysis case.

The uncoupled thermoelasticity problem can also be handled by ABAQUS, making it an ideal code for the present work. If the temperatures are specified at the nodal points within the material and appropriate material constants (including thermal expansion coefficient) are input, the code will interpolate the nodal temperature field to interior Gauss integration points to calculate the thermally induced strain field. The stress field is then determined by the stress-strain relations.

Four-node bilinear elements were chosen for the analyses. In order to check the spatial convergence of the solution, three grid sizes of uniform refinement were employed: $\Delta x = 1/6$ (coarse mesh), $1/12$ (medium mesh), and $1/24$ (fine mesh). (A full description of the grids used in the finite element analysis is contained in Appendix B.) Square elements, $\Delta x = \Delta y$, were used in all analyses. Uniform refinement of the grid size permits a quantitative evaluation of how well the solution converges. Moreover, an extrapolated

value which approximates the result of a grid uniformly finer than the finest used in the calculation can also be computed. The extrapolation scheme used models the error distribution in the numerical analysis as

$$\epsilon = K - K_{\text{ext}} = \epsilon_0 \Delta^c \quad (22)$$

where ϵ is the absolute percentage error in the stress intensity solution K (because of the singularity at the crack tip, this method is inapplicable for determination of stress field convergence, rather it is extended to the stress intensity solution), K_{ext} is the extrapolated solution, ϵ_0 is the error for the unit grid size, Δ is the finite element mesh size, and c is a convergence measure. This extrapolation scheme reduces to a Richardson approximation if $c = 1$. Uniform refinement implies the grid sizes are scaled proportionally. In this case, they are reduced by a factor of 2 with each refinement. Thus the extrapolated value can be derived by algebraic manipulation of the finite element results from the three grids:

$$K_{\text{ext}} = \frac{K_C K_F - K_M^2}{K_C + K_F - 2 K_M} \quad (23)$$

Here the subscripts C, M, and F refer to the coarse, medium and fine finite element solutions, respectively. The solution converges rapidly if $c > 1$. If $c < 0$, the solution diverges. Between these limits, $0 < c < 1$, impaired convergence is obtained.

$$c = -0.693 \ln \left| \frac{K_M - K_{\text{ext}}}{K_C - K_{\text{ext}}} \right| \quad (24)$$

Obtaining the Stress Intensity Factor

The finite element analysis results in solutions to the stress and displacement vectors at discrete points within the solid. In order to assess these results in terms of crack tip stress fields, stress intensity values are needed. The path independent integral is a method which calculates stress intensity values from the data acquired in the finite element and finite difference analyses. It offers the distinct advantage that the errors in the analysis stem only from the numerical approximations used and not from additional sources (i.e. the singularity at the crack tip). For this reason, path independent integrals offer a relatively accurate result with only modest computational effort.[13].

The appropriate integral for the thermoelastic case is developed following Sinclair, Okajima and Griffin [13], taking into account the Duhamel-Neumann analogy for modeling thermoelastic problems [20]. In general, the analogy states that the displacements produced by a temperature T are the same as those produced by a body force equal to $-\beta \nabla T$ and normal surface tractions equal to βT , acting on a body of the same shape but with no variation in temperature. In essence, the effect of the temperature change is the same as that obtained by normal surface tractions equal to βT and body forces equal to $-\beta \nabla T$. By formulating the problem in this way, it is clear that we maintain the exact same eigenfunctions and eigenvectors as those for bodies with no temperature field (those of Williams [4]) and we need only develop a new path independent integral which takes into account body forces proportional to the gradient of the temperature. To do this, we introduce new stress and displacement fields, denoted by the superscript R (for resolved tractions and body forces) and related to those fields satisfying the equations of thermoelasticity (7) through (11) by the relations

$$\begin{aligned}\sigma_x &= \sigma_x^R - \beta T \\ \sigma_y &= \sigma_y^R - \beta T \\ \tau_{xy} &= \tau_{xy}^R \\ u &= u^R \\ v &= v^R\end{aligned}\tag{25}$$

where β is as defined in (8). The new stress field satisfies the equations of linear elasticity in which the body force and normal surface tractions are supplemented by $-\beta \nabla T$ and βT , respectively. These are the same as those presented earlier with the following exceptions: the equations of equilibrium in the presence of a body force field:

$$\begin{aligned}\sigma_x^R, x + \tau_{xy}^R, y - \beta T, x &= 0 \\ \sigma_y^R, y + \tau_{xy}^R, x - \beta T, y &= 0\end{aligned}\tag{26}$$

on R , the stress-displacement relations for a homogeneous and isotropic, linear elastic solid,

$$\sigma_x^R = \frac{2\mu}{(1-2v)} [(1-v)u, x + v v, y]$$

$$\begin{aligned}\sigma_y^R &= \frac{2\mu}{(1-2v)} [(1-v)v_{yy} + v u_{xx}] \\ \tau_{xy}^R &= \mu(u_{xy} + v_{xx})\end{aligned}\quad (27)$$

on R , traction boundary conditions on the crack face, and on the upper and right edges of the region.

$$\begin{aligned}\sigma_y^R &= -\beta T, \quad \tau_{xy}^R = 0 \text{ on } y=0 \quad (0 < x < a) \\ \sigma_y^R &= \beta T, \quad \tau_{xy}^R = 0 \text{ on } y=L \quad (0 < x < W) \\ \sigma_x^R &= \beta T, \quad \tau_{xy}^R = 0 \text{ on } x=W \quad (0 < y < L)\end{aligned}\quad (28)$$

The superscripts on u and v have been omitted since the displacements compatible with σ^R are equal to those produced by the original field by the Duhamel-Neumann theorem. We now have a problem we can handle analytically and, as long as the temperature field is not more singular than logarithmic behavior, there is no contribution to the stress intensity factor from the temperature field in the superposition (substituting σ_y of Equation (25) into Equation (12)). Thus, the stress intensity factor associated with the original problem is equal to that associated with the fields σ^R and u . We turn now to developing the path independent integral for regions containing body forces.

Following the procedure in Sinclair, et al.,[13] we invoke Betti's reciprocal theorem in the plane for regions with body forces. For the case with a body force field equal to $-\beta \nabla T$, stress and displacement fields σ^R and u , respectively, Betti's reciprocal theorem can be stated

$$\begin{aligned}\int_{\Gamma} [(\sigma_x^R u^* + \tau_{xy}^R v^* - \sigma_x^* u - \tau_{xy}^* v) n_x + (\sigma_y^R v^* + \tau_{xy}^R u^* - \sigma_y^* v - \tau_{xy}^* u) n_y] dS \\ - \beta \int_A (T_x u^* + T_y v^*) dA = 0\end{aligned}\quad (29)$$

The starred functions are the complementary eigenfunction stress and displacement fields satisfying the same field equations, namely the complementary fields contained in Sinclair et al., specializing $\lambda=1/2$ and $\alpha=\pi$. These fields are given for this special case in Appendix C. The integration is performed in a counter-clockwise direction along any closed path Γ in R . dS and dA refer to line and area elements, respectively, n_x and n_y are the components

of the unit outward normal to Γ and A is the area enclosed by Γ . On choosing the contour, we proceed as in [13] and pick any path which includes the crack faces and an inner circular arc starting at the crack face above the axis of symmetry and ending on the face below it (Figure 3). The choice of the crack faces is based on the homogeneous traction conditions of the complementary eigenfunction stress field along the faces. We take full advantage of the crack face conditions by substituting the thermoelastic stress field for σ^R via the relations of (25) since σ_y^R does not generally equal zero on this boundary while σ_y is identically zero there. In the limit as the radius of the inner arc tends to zero, the only contribution of the inner arc to the integral emanates from the singular parts of the stress fields. Since all stress fields now obey homogeneous crack face traction conditions the counter-clockwise integration of the inner arc now equals the integration along the outer path summed with the area integration. By scaling the contribution of the circular arc so that in the limit, the stress intensity factor is recovered, we obtain the appropriate expression for K :

$$K = \int_{\Sigma_1} \{(\sigma_x u^* + \tau_{xy} v^* - \sigma_x^* u - \tau_{xy}^* v) n_x + (\sigma_y v^* + \tau_{xy} u^* - \sigma_y^* v - \tau_{xy}^* u) n_y\} dS \\ - \beta \int_A (T_x u^* + T_y v^*) dA + \beta \int_{\Sigma_1 + \Sigma_2} [(Tu^*) n_x + (Tv^*) n_y] dS \quad (30)$$

where Σ_1 and Σ_2 are the outer path and crack face portions, respectively, of the contour Γ . This expression is simplified by invoking the divergence theorem to combine the area integral and the second line integral as a single area integral. Thus, the path independent integral which defines the stress intensity factor for a body subjected to a temperature T , satisfying the equations of thermoelasticity (7) through (11), is

$$K = \int_{\Sigma_1} \{(\sigma_x u^* + \tau_{xy} v^* - \sigma_x^* u - \tau_{xy}^* v) n_x + (\sigma_y v^* + \tau_{xy} u^* - \sigma_y^* v - \tau_{xy}^* u) n_y\} dS \\ + \beta \int_A T(u^*,_x + v^*,_y) dA \quad (31)$$

The resulting path independent integral is the sum of an area integral containing the temperature field and a line integral containing the stress and displacement fields.

Numerical computation of K requires compatible quadratures to accurately determine the stress intensity factor. Both the temperature and displacement fields are determined at nodal locations, while the stress field is most accurate at the interior Gauss integration points. However, the ABAQUS code does interpolate these stress values to node locations if so desired and integration was performed using these interpolated nodal values.

Integration using Simpson's rule is based on the use of parabolic arcs rather than straight lines to approximate the integrand [23] and is accurate to order $(\Delta x)^4$. This technique uses nodal values of the function. Thus, it is well suited for the evaluation of the line integral since this approach does not require evaluation of the function near its singularity, the crack tip.

Solution of the area integral is not as straightforward. Upon evaluation of $u_{i,j}^*$, the area integral becomes (in cylindrical coordinates with the origin at the crack tip)

$$\int_A \beta T \frac{1}{\sqrt{r}} \cos \frac{3\theta}{2} dr d\theta \quad (32)$$

for the Mode I stress intensity factor. The behavior of the complementary eigenfunction displacement field results in an integrable square root singularity in the integrand in one coordinate (the other remains nonsingular). Because of this singularity and the fact that the integrand must be numerically evaluated throughout the area, a quadrature which can handle this singularity is required. A Gauss-Legendre quadrature was developed following [24] to approximate the general form of the integral:

$$\int_a^b f(x) \frac{1}{\sqrt{x}} dx \sim \sum_{i=1}^N w_i f(x_i) \quad (33)$$

Defining the integral in this manner removes the difficulty in integrating the singularity since we require $f(x)$ to be regular. If $f(x)$ is a polynomial, this approximation is exact when used with the proper weights, w_i , and abscissas, x_i . For this particular square root weight function, the abscissas are the zeros of the Legendre polynomials, $P_n(\sqrt{x})$ [25]. Values for the weights and abscissas were calculated for up to 96 interior points and are tabulated in Appendix D.

For the nonsingular integration (over θ), standard Gauss-Legendre quadrature is used. Tabulated values of weights and abscissas for this method are common. Numerical

results of the area integral using these two Gauss-type quadratures converged rapidly when tested on several problems:

$$\begin{aligned}f(x) &= 1.0 \\f(x) &= 1 - 2x \\f(x) &= 5 - 6x^2 \\f(x) &= \sqrt{x} \\f(x) &= \ln(x)\end{aligned}$$

With the first three functions, the value converged to the sixth decimal point with only six interior Gauss points. Convergence on the last two functions was somewhat slower. For the square root function, the value converged to the fourth decimal point after 48 interior points; for the logarithmic function, the value converged to the third point after 48 interior points.

In order to verify the stress analysis and stress intensity calculation techniques, we perform several test problems. In each of the test problems, static loadings are applied to center-cracked geometries. The loading conditions for each of these problems are detailed in Table 1 and include (i) uniaxial tension applied at $y=L$, no temperature distribution, (ii) displacements applied on the boundary $y=L$, no temperature distribution, and (iii) a spatially constant temperature distribution with the ends fixed from vertical displacement. Normalized stress intensity factors, taken from the literature are also presented in Table 1 and are exact for infinitely long specimens. Note that width correction factors, taken from the literature, are also included in the table.

In general, excellent agreement with the quoted values for all test problems is observed in the results which are listed in Table 2. The calculations were performed in plane-strain with a Poisson ratio of 0.3. The results are tabulated as normalized stress intensity factors divided by the appropriate reported solution described in Table 1 such that an exact value equals unity. The normalized crack length, $a/W = 1/3$ for all cases listed in Table 2. The normalizing factor is

$$K = \frac{K_I}{\sigma_0 \sqrt{\pi a}} \quad (34)$$

where σ_0 refers to the applied load. For test case (i), σ_0 is simply the traction applied at $y=L$. For test case (ii), σ_0 is given by

$$\sigma_0 = \frac{v_0}{1-v^2} \frac{E}{L} \quad (35)$$

For test case (iii), σ_0 is given by

$$\sigma_0 = -\frac{\alpha ET_0}{1-v} \quad (36)$$

The normalized crack length, a/W , for the values quoted is 1/3. In addition, stress intensity values were obtained for $a/W = 1/2$ and the accuracy of the results was found to be consistent with that computed for the shorter crack length.

In addition to the individual values generated by coarse, medium and fine grids, the extrapolated stress intensity factors obtained by using Equation (23), and convergence measures from (24) are included in the tables. Further, path independence of the integral was demonstrated by performing the integration along two different paths: one which takes advantage of one boundary of the specimen, another which remains in specimen interior. The paths of integration are illustrated in Figure 4. In each case, the two contours converge to similar values of the stress intensity factor. The variation of the two paths is of the order of 20 per cent for the coarse grid and converges to approximately 2 per cent for the fine grid (less than 1 percent for the extrapolated values). However, slower convergence was observed with the contour on the boundary, probably due to the difficulty in satisfying the boundary conditions in the finite element analysis, resulting in relatively large errors along the portion of the integration path which is on the boundary. For this reason, the interior contour was selected for all successive calculations.

Numerical Results

Keeping the normalized crack length constant and equal to 1/3, dimensionless stress intensity factors were computed for dimensionless frequencies ranging from 0 to 8.² This range is representative of typical thermal cycle frequencies used in fatigue testing. For example, the high-strength nickel alloy IN100 has a diffusivity of 0.00649 in.²/s³. If the

²The dimensionless frequency, ω^* , is related to the frequency, ω , by the relation $\omega^* = \omega L^2 / (D \pi)$.

³For $k=100$ Btu in/(ft² hr °F), $\rho=0.28$ lb/in³, $C_p=0.106$ cal/g°C and $D=k/(\rho C_p)$.

total specimen length is 2 inches ($2L = 2$ in.), the normalized frequency $\omega^* = 2.5$ corresponds to a real frequency of approximately $\omega = 0.5$ cycles/min. Results of the computations are tabulated in Table 3 for the case with the sinusoidally varying end temperature and in Table 4 for the case with sinusoidally varying uniform heat source. As listed, the results are the dimensionless magnitude, K , and phase lag, Φ , of the harmonic stress intensity factor:

$$\frac{K_I}{\frac{-\alpha E \tau_0}{(1-\nu)} \sqrt{\pi a}} = K \cos(\omega t - \Phi) \quad (37)$$

where the dimensioning parameter τ_0 refers to the end temperature T_0 in Table 3 and the magnitude of the heat source $h_0 L^2$ in Table 4. If K_s and K_c are the dimensionless stress intensity factors associated with the $\sin(\omega t)$ and $\cos(\omega t)$ components of the temperature field (Equations (14) and (15)), then the dimensionless magnitude K is obtained by taking the square root of the sum of the squares of K_s and K_c :

$$K = \sqrt{K_s^2 + K_c^2} \quad (38)$$

and the phase lag, Φ , is obtained thus:

$$\Phi = \arctan \frac{K_s}{K_c} \quad (39)$$

Because the temperature in the vicinity of the crack tip is of interest, Tables 3 and 4 also include the magnitude, T_1 , and phase, Φ_1 , of the dimensionless crack tip temperature:

$$\frac{T}{\tau_0} = T_1 \cos(\omega t - \Phi_1) \quad (40)$$

In all cases, the values quoted are obtained from the numerical analyses using the extrapolation method described previously (23). The convergence of the stress intensity factors was found to be well behaved.

It is of interest to assess the variation in stress intensity with frequency for the uniform heating condition in which the stress intensity factor is normalized by the temperature at the centerline (the crack tip). With this normalization we can observe the trend in stress intensity with frequency when a specific temperature is maintained within the sample if the temperature at the end is maintained as zero. These data are plotted in Figure 5. It is noted that the maximum stress intensity occurs for the static case, $\omega = 0$.

Using linear superposition we can evaluate the Mode I stress intensity for different fatigue conditions in which uniform, symmetric, heating is applied. By measuring the temperature and phase lag at two locations within the sample (for example, at the crack tip and at a distance L from it), we can derive the stress intensity factor for specific frequencies of thermal cycle using the data presented in Tables 3 and 4. First consider a specimen that is uniformly heated and in which the temperature at the crack tip, T_1 is measured with respect to the end temperature, T_0 . The phase lag of the measured crack tip temperature is then called Φ_1 . With this information, we can combine the heat source results with the boundary temperature results to estimate the contribution of thermal cycling on stress intensity. To maintain the crack tip temperature at T_1 , a sufficient magnitude of the heat is required at a specific phase lag from the boundary temperature. Since we have analyzed the temperatures at the crack tip in all the problems, we need only find the magnitude of the heat source and the phase required to maintain the crack tip at a specific temperature. In other words, if T_{1B} and Φ_{1B} are the magnitude and phase of the crack tip temperature in the case where T_0 is specified on the boundary $y=L$, and T_{1H} and Φ_{1H} are the analogous values in the cases where a symmetric heat source is present, then

$$T_1 \cos(\omega t - \Phi_1) = T_{1B} \cos(\omega t - \Phi_{1B}) + \gamma T_{1H} \cos(\omega t - \Phi_{1H} - \kappa) \quad (41)$$

where γ is a scaling factor for the heat source center temperature and κ is the required phase lag of the heat source. These two parameters are determined by the measurements T_1 and Φ_1 , and the results presented in Tables 3 and 4:

$$\gamma = \frac{\sqrt{T_1^2 + T_{1B}^2 - 2 T_1 T_{1B} \cos(\Phi_1 - \Phi_{1B})}}{T_{1H}} \quad (42)$$

and

$$\kappa = \arctan \frac{T_1 \sin \Phi_1 - T_{1B} \sin \Phi_{1B}}{T_1 \cos \Phi_1 - T_{1B} \cos \Phi_{1B}} - \Phi_{1H} \quad (43)$$

By establishing γ and κ , the stress intensities may also be found. If K_{tot} represents the total dimensionless stress intensity factor in the specimen with crack tip temperature $T_1 \cos(\omega t - \Phi_1)$ relative to the end temperature, $T_0 \cos \omega t$, then

$$K_{tot} = \sqrt{K_B^2 + (\gamma K_H)^2 + 2\gamma K_B K_H \cos(\Phi_B - \Phi_H - \kappa)} \quad (44)$$

where K_B and Φ_B correspond to the magnitude and phase of the stress intensity with boundary temperature prescribed and K_H and Φ_H are the respective values of the stress intensity with an applied heat source. For the static case, if the crack tip temperature is maintained at the same level as the end temperature then the stress intensity is zero since the temperature is uniform within the plate. This is consistent with Equations (41) through (44). If $T_1 = T_0$ and $\omega = 0$ ($\Phi_1 = 0$), then from (42), $\gamma = 0$. Since K_B is 0 in the static case, we have $K_{tot} = 0$.

Two examples of this type of superposition are considered and results are plotted in Figures 6 and 7. In these plots, the combined stress intensity, K_{tot} , is plotted as a function of T_1/T_0 for several frequencies. Two phase lags are illustrated and correspond to the crack tip temperature in phase and 180° out of phase with the end temperature. It is noted that the stress intensity is zero for all frequencies in the uniform heating case when the crack tip temperature is equal to and in phase with the end temperature. What this says is that all temperatures in the plate vary according to $T_0 \cos \omega t$ when this constraint is imposed at both the end of the specimen and at the crack tip. In order for this to occur numerically, the sum of the phases Φ_H , Φ_B and κ must add to $\pm 180^\circ$ in Equation (44). (This is true as long as γ is non-zero which is the case for nonzero frequency.) The sum of Φ_H and Φ_B from Tables 3 and 4 is equal to -90° to the third decimal point for each nonzero frequency. Determining κ from Equation (43) is straightforward and equal to -90° leading to a sum of -180° . These data confirm the accuracy of the numerical values in the tables.

Summary of Results

In this section, we have developed a method to estimate the variation of thermal fatigue stress intensities as a function of frequency for the basic problem of a uniform heat source in a center-cracked plate. Resulting values of stress intensity were computed for a range of frequencies and show that the static case, $\omega = 0$, gives the strongest stress intensity. Further, the stress intensity depends on the phase and magnitude of the temperature at the specimen end relative to the temperature along the centerline. In order to estimate the stress intensity for specific fatigue test cases, laboratory data, specifically the relative temperature values, are required.

Table 1
Loading conditions and reported stress intensity solutions for test problems

The plane strain solutions are normalized such that

$$K = \frac{K_I}{\sigma_0 \sqrt{\pi a}}$$

Test Case	Applied Conditions	Reported Solutions (Center crack geometry)	Reference
(i)	$\sigma_y = \sigma_0$ at $y=L$ $T = 0$	$K = F_1(a/W)$ $F_1(1/3) = 1.07$	[26]
(ii)	$v=v_0$ at $y=L$ $T = 0$ $\sigma_0 = \frac{v_0}{(1-v^2)} \frac{E}{L}$	$K = 1.0$	[26]
(iii)	$v=0$ at $y=L$ $T = T_0$ $\sigma_0 = -\frac{\alpha ET_0}{1-v}$	$K = 1.0$	[26]

Table 2
Results of test problem calculations using center-crack geometry
Reported as normalized stress intensity factor, precise value for K_{ext} is 1.0

Test Case	Integration Path ⁴	Coarse Grid	Medium Grid	Fine Grid	K_{ext}	c
(i)	I	0.9280	0.9980	0.9960	0.9955	5.95
	B	1.0953	1.0439	1.0224	1.0075	1.23
(ii)	I	0.8220	0.9870	0.9796	0.9800	3.95
	B	1.0960	1.0330	1.0065	0.9873	1.25
(iii)	I	0.8725	0.9883	0.9798	0.9804	3.64
	B	1.0910	1.0330	1.0065	0.9841	1.12

⁴ I refers to the interior path; B to the boundary path.

Table 3
 Dimensionless stress intensity factor and temperature field results for
 center-crack geometry,
 end temperature prescribed non-zero, $\tau_0 = T_0$

ω^*	K	Φ	T_1	Φ_1
	($\times 10^{-3}$)	(radians)		(radians)
0	0.0	-1.571	1.0	0.0
0.5	47.623	-0.937	0.841	0.716
1.0	69.175	-0.528	0.610	1.202
1.5	76.899	-0.277	0.452	1.532
2.0	79.348	-0.102	0.349	1.784
3.0	78.512	0.139	0.229	2.183
4.0	74.793	0.312	0.163	2.513
8.0	55.627	0.710	0.0577	3.544

Table 4
Dimensionless stress intensity factor and temperature field results
for center crack geometry, uniform heat source
 $\tau_0 = h_0 L^2$

ω^*	K (x 10 ⁻³)	Φ (radians)	T ₁	Φ_1 (radians)
0	36.125	-3.141	0.5	0.0
0.5	30.391	-2.505	0.421	0.584
1.0	22.071	-2.098	0.307	0.940
1.5	16.359	-1.847	0.229	1.140
2.0	12.657	-1.673	0.179	1.447
3.0	8.358	-1.432	0.122	1.407
4.0	5.980	-1.260	0.0904	1.486
8.0	2.416	-0.864	0.0419	1.592

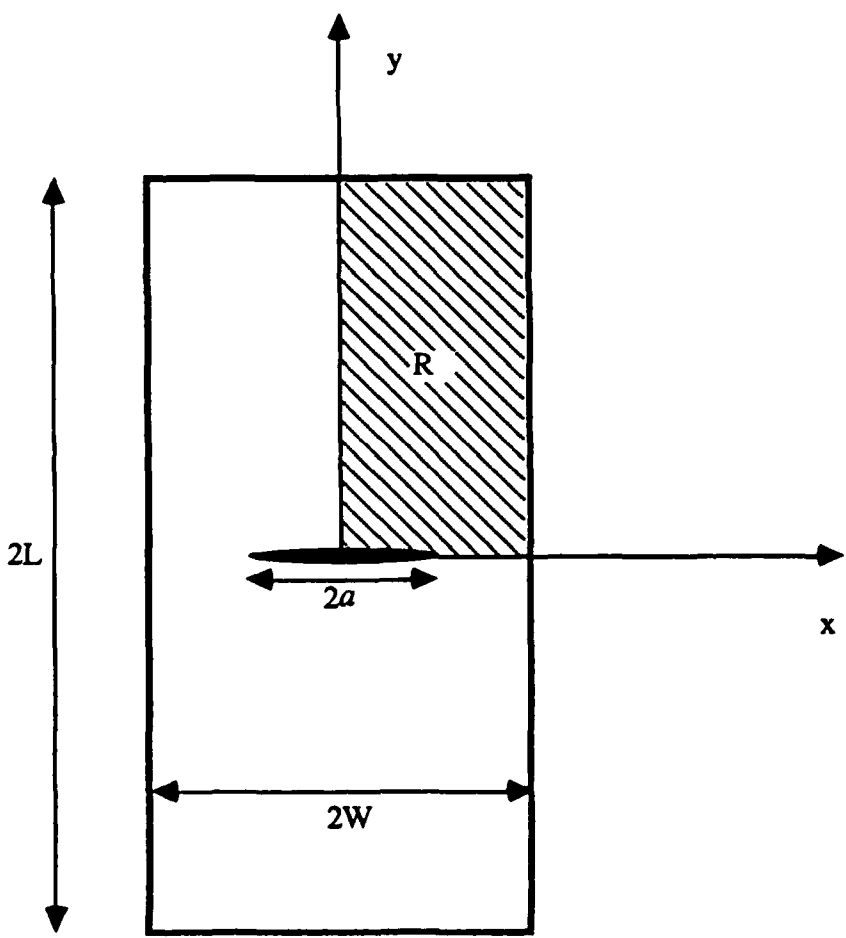


Figure 1. Center-Crack Geometry of the posed problem

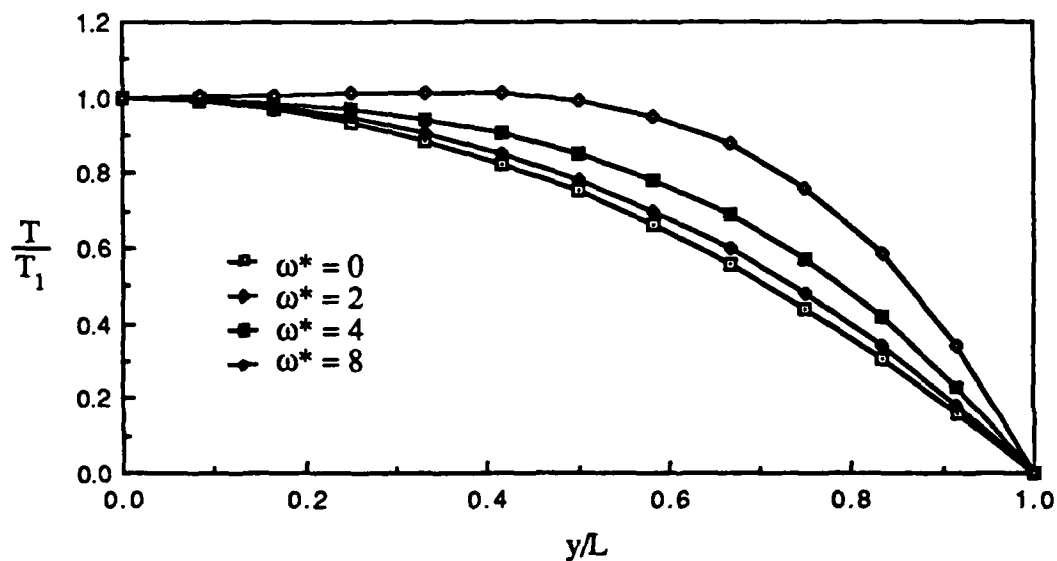


Figure 2. Magnitude of the temperature field induced by uniform heating⁵.

⁵The dimensionless frequency, ω^* , is related to the frequency, ω , by the relation $\omega^* = \omega L^2 / (D\pi)$.

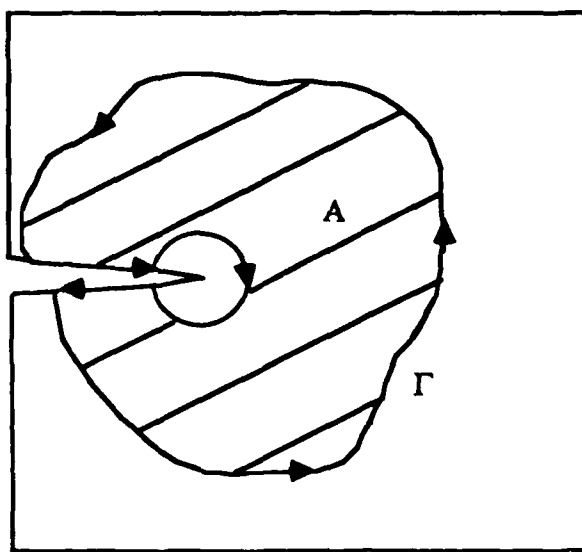


Figure 3. Integration contour for path independent integral

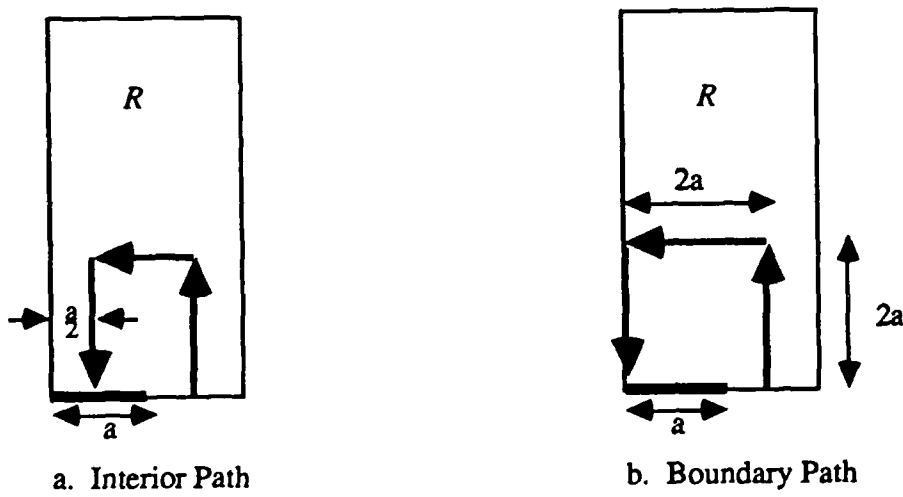


Figure 4. Integration paths for the test problems. Areas shown represent the upper quadrant for the center crack geometry.

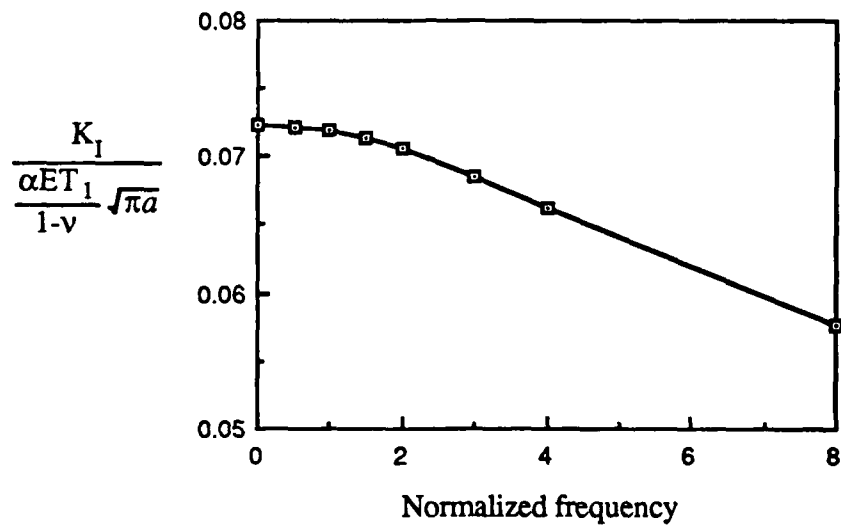


Figure 5. Amplitude of the stress intensity normalized by the crack tip temperature for the uniform heating case.

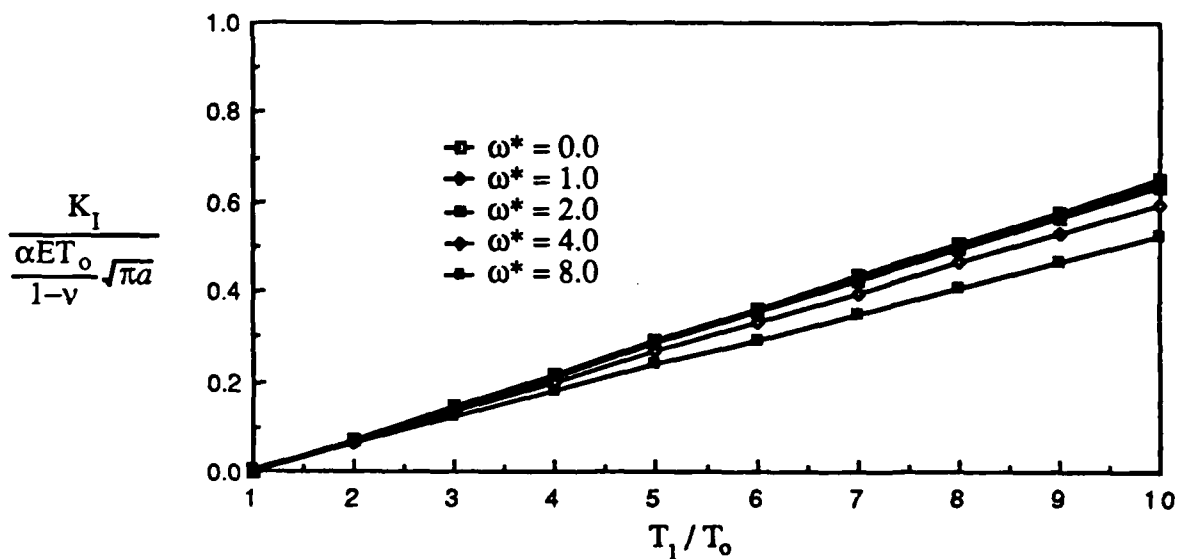


Figure 6. Amplitude of the stress intensity as a function of the crack tip temperature. The temperature at the crack tip, T_1 , is maintained by uniform heating and is in phase with the end temperature, T_o .

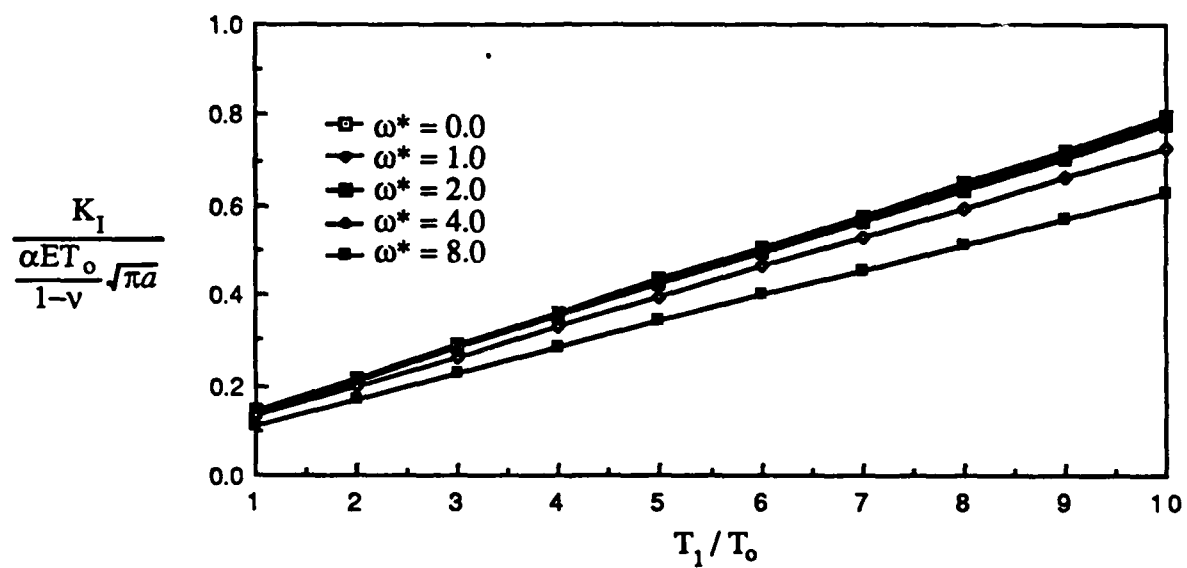


Figure 7. Amplitude of the stress intensity as a function of the crack tip temperature and dimensionless frequency. The temperature at the crack tip, T_1 , is maintained by uniform heating and is 180° out of phase with the end temperature, T_0 .

III. EXTENSIONS OF THE UNIFORM HEAT SOURCE PROBLEM

In this section, we consider several extensions to the uniform heat source problem formulated and solved in Chapter II. First, because fatigue test specimens are not all geometrically equivalent to the center-crack geometry, we will investigate some geometrical differences: edge-crack geometries and plate and crack length scaling dependence, in particular. Secondly, because specimen heating may not always be symmetric, we will consider antisymmetric temperature fields which give rise to Mode II stress intensities. These, when combined linearly with the symmetric heating results, will lead to predictions of the stress intensity in more general thermal fatigue situations. Differences in problem formulation and solution will be discussed in the pertinent sections, below.

Geometrical variations

a. Edge-Crack Geometry

In fatigue testing, cracks can be located on the specimen edge or in its center. The important distinction in the crack location is that the edge-cracked component corresponds to a simply-connected region while the center-cracked component corresponds to a multiply-connected region. In our investigation of this geometric variation, we use the same formulation as that already presented and the edge-crack geometry of Figure 8. The region R of the analysis is, by symmetry, the upper half of the rectangular plate shaded in the figure and corresponds to the same region investigated in the center-crack problem:

$$R = \{x, y \mid 0 \leq x \leq W, 0 \leq y \leq L\} \quad (45)$$

A crack of length a is contained on the boundary $0 \leq x \leq a$ along the line $y = 0$. The boundary conditions along the edge containing the crack are the only variation from the formulation already presented. The condition on the temperature problem is that the edge remains insulated which is identical to the condition of symmetry imposed on the center-crack problem (4). Because of this, the temperature fields for the two geometries are identical and will not be reiterated here.

The conditions for the stress field, however, are different along the edge containing the crack. On this boundary, traction-free conditions are imposed:

$$\sigma_x = 0, \tau_{xy} = 0 \text{ on } x = 0 \text{ (} 0 < y < L \text{)} \quad (46)$$

The remaining conditions, Equations (9) and (11), still hold.

With this, we have the formulation for the edge-cracked geometry. Solution is accomplished with the same methods described in the previous section: temperature values at nodal locations are calculated from the closed form temperature fields of Equations (19) and (20) and are used as input to the finite element calculations. The path independent integral derived in Equation (31) is again used to calculate the dimensionless stress intensity factors.

To verify the stress intensity calculations for the edge-cracked geometry several test problems are again performed. The three static test problems described for the center-crack geometry are again used in addition to a fourth test case in which is applied a static temperature distribution proportional to x/W with ends fixed from vertical displacement. Table 5 contains descriptions of the loading conditions for each of the test problems and width and bending correction factors taken from the literature. Results of the test cases, normalized such that an exact value equals unity, are listed in Table 6 for coarse, medium and fine mesh sizes. The calculations were performed in plane-strain with Poisson's ratio equal to 0.3. Unless specified, results quoted are for normalized crack lengths of 1/3. In general, excellent agreement with the quoted values for all test problems is observed for the fine mesh, with errors of less than two per cent generally observed.

Dimensionless stress intensity factors for the posed edge-crack problem were computed for the same range of frequencies as the center-crack problem and are tabulated in Table 7 for the case with sinusoidally varying end temperature and in Table 8 for the case with sinusoidally varying uniform heat source. Again, the listed values are the dimensionless magnitude, K , and the phase lag, Φ , of the harmonic stress intensity factor. It is noted that the stress intensity values obtained are much lower than those of the center-cracked geometry, often by a factor of five. Similar trends of decreasing stress intensity beyond a dimensionless frequency of about 2.0 are observed.

b. Crack and sample length scaling effects.

Although nondimensionalizing provides a way to generalize the problem so that many different sizes of samples can be evaluated with only one calculation, it does not take into account variations in ratios of crack length and the sample dimensions. In this section, we investigate the dependence of length scaling on the stress intensity factor by computing the stress intensity factor as a function of frequency for shorter relative crack lengths, $a/W=1/6$, and longer relative sample lengths, $L/W = 4.0$. For comparison, the case in which the heat source varies sinusoidally was used in these scaling calculations. Results obtained by setting the normalized crack length equal to half that used in the original calculations, are tabulated in Table 9. Results of doubling the relative sample length are listed in Table 10.

The stress intensity results listed are nondimensionalized by the square root of the crack length. From Tables 4 and 9, since the values of normalized stress intensity are nearly the same, it is apparent that the stress intensity factor scales approximately as $a^{1/2}$ (the crack length normalization factor). Further, this scaling is independent of the frequency. The $a^{1/2}$ scaling is consistent with stress intensities generated by mechanical loads.

To assess the effects of scaling the sample length, we compare the results of Tables 4 and 10. Doubling the length of the sample relative to the width apparently reduces the stress intensity in the sample by a factor of approximately four, $(L/W)^2$, for the same temperature value at the crack tip. It is noted, however, that this solution may be particular to this situation and may not be a general result since, by lengthening the sample, the temperature constraint at the end $y=L$ would probably be affected as well.

Asymmetrical temperature distributions

The equations and boundary conditions which define the temperature fields are linear and so the fields themselves may be combined via linear superposition. This implies that an asymmetric temperature field can be decomposed as the sum of a symmetric field and an antisymmetric field. If we consider the uniform heat source and the symmetric end temperature conditions as the symmetric contribution and a linearly varying heat source and antisymmetric end temperature conditions as the antisymmetric contributions, we can obtain the coefficients to the first terms in a Taylor series approximation to a more general class of problems. These antisymmetric fields will be developed and investigated in this section.

The constraints imposed in the formulation of the antisymmetric problem are that the temperature at the end $y=+L$ is the negative of the temperature at the end $y=-L$. This gives the antisymmetric condition of temperature equal to zero along the x -axis, not

including the crack ($a < x < W$). Along the crack faces, the condition of insulation (normal gradient equal to zero) still holds. Thus, a discontinuity in the temperature boundary conditions occurs at the point $x = a$, and the temperature fields cannot be obtained in closed form. In addition, the heat source will be imposed as one that varies linearly in the y -direction:

$$h(x,y) = h_o \frac{y}{L} \quad (47)$$

for a constant h_o . The coupled equations defining the temperature field (16) are elliptic and so the fields T_s and T_c may be calculated using finite difference methods as described below.

The boundary conditions pertaining to the stress field are identical to those of the symmetric problem with the exception of those along the x -axis in the region $a < x < W$. Again, antisymmetric conditions are imposed :

$$\sigma_y = 0 \text{ and } u = 0 \text{ on } y = 0 \quad (a < x < W) \quad (48)$$

The stress field solution will again be obtained numerically using the finite element method already discussed.

a. The finite difference method

Finite difference methods employ Taylor series expansions to express derivatives of analytic functions by arithmetic operations. In our analysis we employ representations of derivatives involving error of order $(\Delta x)^2$. When these difference formulas are substituted into the coupled equations for temperature, a set of linear algebraic equations is obtained. The method originally chosen for solving these equations was Gauss-Seidel iteration with an absolute convergence criterion. The iterative method starts with a guess for the unknown vector and cycles through the equations replacing the solution for the unknowns until each solution satisfies the convergence criterion. This continues until a change in each unknown from the previous iteration to the current iteration is less than an acceptable value. This value was set to be no greater than 10^{-6} . With a criterion this small, however, convergence was too slow for the two-dimensional fields and with greater values, errors in the temperatures were unacceptably large. Because of this, an alternate method, Gauss-Jordan elimination, was selected and used for the more complex temperature fields. This

technique uses row and column combination until a lower- or upper-triangular array of equations results. The unknown vector is then solved for directly.

Using Gauss-Jordan elimination provides a further advantage over iteration in that accuracy of the solution depends only on the grid size used and round-off errors rather than the additional error associated with iteratively solving the set of algebraic equations with too large a convergence criterion. In order to check the spatial convergence of the solution, three grid sizes of uniform refinement were employed in the analysis: $\Delta x = 1/6$ (coarse mesh), $1/12$ (medium mesh), and $1/24$ (fine mesh). Square elements, $\Delta x = \Delta y$, were used in all temperature analyses. Uniform refinement of the grid size permits use of the extrapolation scheme discussed in the finite element section to model the error distribution in the numerical analysis as

$$\epsilon = T - T_{ext} = \epsilon_0 \Delta^c \quad (49)$$

where ϵ is the error in the temperature solution T at a particular node location, T_{ext} is the extrapolated solution, ϵ_0 is the error for the unit grid size, Δ is the finite difference mesh size, and c is the convergence measure.

To verify the numerical solution method, we use several techniques. First, the closed form one-dimensional representations of the symmetric temperature problem (Equations (19) and (20)) are compared with the values obtained inputting the appropriate boundary conditions and forcing function for the symmetric problems. Secondly, a one-dimensional antisymmetric problem in which the conditions $T=0$ at $y=0$ and $T=T_0$ at $y=L$ was formulated and solved in closed form and compared with a numerical solution. Finally, boundary values for three different known temperature distributions were input to the code and the resulting numerical solutions compared with the known distributions. These three temperature distributions and their respective forcing functions are:

$$\frac{T(x,y)}{h_0 L^2} = 1 - \frac{x^2 + y^2}{4} ; \frac{h(x,y)}{h_0 L^2} = -1 \quad (50)$$

$$\frac{T(x,y)}{h_0 L^2} = 1 - \frac{y^4}{4} ; \frac{h(x,y)}{h_0 L^2} = -3 y^2 \quad (51)$$

$$\frac{T(r, \theta)}{T_0} = \sqrt{r} \sin \frac{\theta}{2} ; h(r, \theta) = 0 \quad (52)$$

where the spatial variables x and y are normalized to the specimen length, L , $r = (x^2 + y^2)^{1/2}$ and $\theta = \arctan(x/y)$. In general, all three verification techniques yielded numerical solutions which converged rapidly to the desired solutions, within one per cent error for the mesh sizes 1/6, 1/12 and 1/24.

b. Numerical results

Again the crack length was maintained as $W/3$ and dimensionless Mode II stress intensity factors were computed for dimensionless frequencies ranging from 0 to 8 with the same dimensioning parameters as those in the symmetric problem:

$$\frac{K_{II}}{\frac{-\alpha E t_0}{(1-v)} \sqrt{\pi a}} = K \cos(\omega t - \Phi) \quad (53)$$

Results of the computations are tabulated in Table 11 for the case with sinusoidally varying end temperature and in Table 12 for the case with sinusoidally varying linear heat source⁶. The tables also contain the temperature magnitudes and phase lags (T_1 and Φ_1) at the location $x = 0$, $y = 0^+$ and not at the crack tip since the temperature is constrained to be zero there.

In general, the stress intensity magnitudes vary much less with frequency than those of the symmetric problem and are generally much lower at specific frequencies than the corresponding Mode I stress intensities.

Summary of Results

In this section we considered several extensions to the basic problem formulated and analyzed in the previous section. First, in considering edge-crack geometries, we found that the edge-crack region results in stress intensities much lower than the center-crack region. Secondly, we found that the stress intensity is proportional to $a^{1/2}$. This is consistent with stress intensities induced by mechanical loads. In a particular problem in which specimen length scaling was examined, the stress intensity scaled as the inverse of

⁶The temperature fields for these specific problems were found to converge adequately.

the square of the length. However, this is not considered a general result since the temperature constraint at the specimen end would probably change with the scaling. Finally, antisymmetric temperature fields were evaluated and Mode II stress intensities calculated. In general, we found these stress intensities to be smaller than the Mode I stress intensities but in order to evaluate the significance of the Mode II values, representative cases would have to be evaluated.

Table 5

Loading conditions and reported stress intensity solutions for test problems

The plane strain solutions are normalized such that

$$K = \frac{K_I}{\sigma_0 \sqrt{\pi a}}$$

Test Case	Applied Conditions	Reported Solutions (Edge crack geometry)	Reference
(i)	$\sigma_y = \sigma_0$ at $y=L$ $T = 0$	$K=F_2(a/W)$ $F_2(1/3)=1.7864$	[26]
(ii)	$v=v_0$ at $y=L$ $T = 0$ $\sigma_0 = \frac{v_0}{(1-v^2)} \frac{E}{L}$	$K=G(a/W, L/W)$ $G(1/3, 2)=1.2467$	[27]
(iii)	$v=0$ at $y=L$ $T = T_0$ $\sigma_0 = -\frac{\alpha ET_0}{1-v}$	$K=G(a/W, L/W)$ $G(1/3, 2)=1.2467$	[27]
(iv)	$v=0$ at $y=L$ $T = 2 T_0 \frac{x}{W}$ $\sigma_0 = -\frac{\alpha ET_0}{1-v}$	$K=0.5$	[15]

Table 6
 Results of test problem calculations using edge-crack geometry
 Reported as normalized stress intensity factor, precise value is 1.0

Test	Coarse	Medium	Fine		
Case	Grid	Grid	Grid	K_{ext}	c
(i)	0.8000	0.9403	0.9660	0.9718	1.17
(ii)	0.8711	0.9808	0.9839	0.9840	2.47
(iii)	0.8510	0.9843	0.9849	0.9850	3.64
(iv) ⁷	0.9280	0.9746	0.9814	0.9826	1.33

⁷ $a/W = 1/2.$

Table 7
 Dimensionless stress intensity factor results
 for the sinusoidally varying end temperature,
 Edge crack geometry

$$\tau_0 = T_0$$

ω^*	K	Φ
	($\times 10^{-3}$)	(radians)
0	0.0	-1.571
0.5	9.324	-0.883
1.0	13.504	-0.415
1.5	15.060	-0.107
2.0	15.510	0.125
3.0	15.252	0.481
4.0	14.461	0.767
8.0	10.392	1.620

Table 8
 Dimensionless stress intensity factor results
 for the sinusoidally varying uniform heat source,

Edge crack geometry

$$\tau_0 = h_0 L^2$$

ω^*	K	Φ
	$(\times 10^{-3})$	(radians)
0	7.072	-3.142
0.5	5.978	-2.448
1.0	4.339	-1.984
1.5	3.618	-1.677
2.0	2.530	-1.447
3.0	1.782	-1.092
4.0	1.336	-0.807
8.0	0.413	0.041

Table 9

Dimensionless stress intensity factor and temperature field results, $a/W = 1/6$
for the sinusoidally varying uniform heat source,

Center crack geometry

$$\tau_0 = h_0 L^2$$

ω^*	K	Φ	T_1	Φ
	($\times 10^{-3}$)	(radians)		(radians)
0	39.801	3.142	0.500	0
1.0	24.326	4.179	0.307	0.940
2.0	13.962	4.596	0.179	1.263
4.0	6.607	-1.287	0.0904	1.486
8.0	2.467	-0.913	0.0419	1.592

Table 10
 Dimensionless stress intensity factor and temperature field results, L/W = 4.0
 for the sinusoidally varying uniform heat source

Center crack geometry

$$\tau_0 = h_0 L^2$$

ω^*	K	Φ	T ₁	Φ
	(x 10 ⁻³)	(radians)		(radians)
0	9.459	3.142	0.500	0.0
0.5	7.956	3.834	0.421	0.585
1.0	5.775	4.297	0.307	0.940
2.0	3.303	4.592	0.179	1.263
4.0	1.541	-0.814	0.0904	1.486
8.0	0.548	0.0282	0.0419	1.592

Table 11
 Dimensionless stress intensity factor and temperature field results
 for the antisymmetric problem of sinusoidally varying end temperature,
 Center crack geometry
 $\tau_0 = T_0$

ω^*	K	Φ	T_1	Φ
	($\times 10^{-3}$)	(radians)		(radians)
0	34.319	0.0	0.146	0.0
0.5	34.364	0.409	0.144	0.287
1.0	34.484	0.798	0.137	0.564
1.5	34.608	1.151	0.128	0.826
2.0	34.674	1.462	0.118	1.068
3.0	34.492	1.967	0.0972	1.497
4.0	33.901	2.349	0.0793	1.864
8.0	27.141	3.209	0.0373	2.994

Table 12
 Dimensionless stress intensity factor and temperature field results
 for the antisymmetric problem of sinusoidally varying linear heat source,
 Center crack geometry.

$$\tau_0 = h_0 L^2$$

ω^*	K	Φ	T ₁	Φ
	(x 10 ⁻³)	(radians)		(radians)
0	4.117	0.0	0.0122	0.0
0.5	4.054	0.211	0.0120	0.208
1.0	3.878	0.411	0.0115	0.407
1.5	3.629	0.599	0.0107	0.589
2.0	3.335	0.762	0.00986	0.753
3.0	2.757	1.040	0.00815	1.024
4.0	2.263	1.253	0.00669	1.233
8.0	1.111	1.766	0.00327	1.718

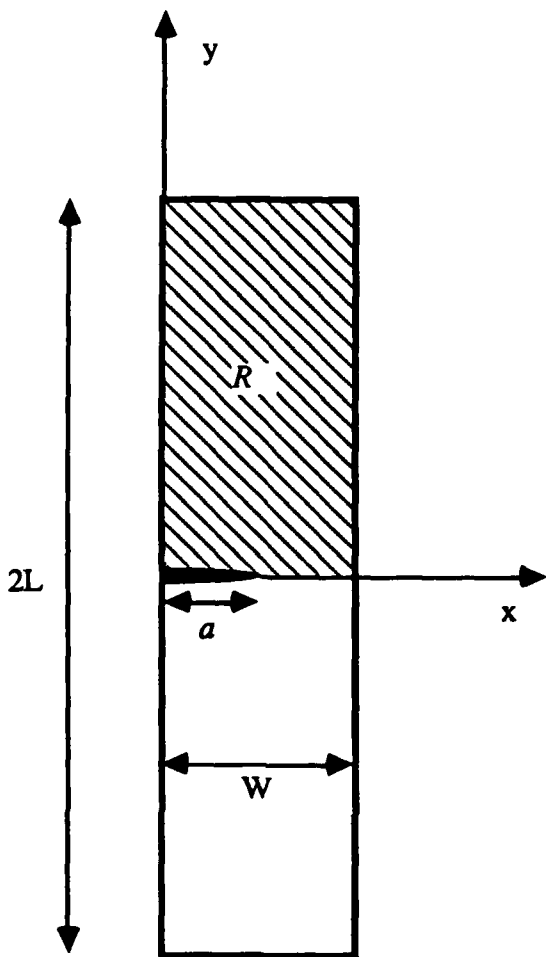


Figure 8. Edge-Crack Geometry

IV. DIRECT RESISTANCE HEATING OF A CENTER-CRACKED PLATE

An alternative method for heating fatigue specimens is to apply an electric current uniformly across the end of the specimens. The major difference between the direct current and heat lamp methods is that the insulated crack faces permit no current flow and so the heat source generated by the current is singular at the crack tip although the temperature remains bounded there. This singularity may induce a different stress intensity behavior than the regular heat source induced by conventional lamp heating.

Defining the Heat Source

The heat source induced by an electric current flowing in a plate is calculated from the electric current density vector, \mathbf{I} , by the relation

$$h(x,y) = \frac{\rho}{k} (\mathbf{I} \cdot \mathbf{I}) \quad (54)$$

where ρ is the electric resistivity and k is the thermal conductivity of the material. Thus, in order to evaluate the heat source magnitude for the center-cracked plate problem, we must first determine the resultant electric current vector in a plate of width W with a center crack exposed to a far-field electric potential. We approach this problem by taking advantage of the analogy of fluid flow around an infinite cascade of flat plates and consider the solution in the rectangular region under investigation. A full description of the derivation of the electric potential heat source is given in Appendix A. If the electric potential in the plate is ϕ , it is related to the electric current by the vector expression,

$$\mathbf{I} = -\nabla \phi / \rho \quad (55)$$

The electric potential in the region R exposed to a potential drop per unit length of ϕ_0 is derived in Appendix A as:

$$\phi = \frac{2W}{\pi} \phi_0 \ln [\alpha^2 + \beta^2 + \xi \pm 2\sqrt{\xi} (\alpha \cos \frac{\eta}{2} - \beta \sin \frac{\eta}{2})] \quad (56)$$

where

$$\begin{aligned}
 \alpha &= \cos \frac{\pi x}{2W} \cosh \frac{\pi y}{2W} \\
 \beta &= \sin \frac{\pi x}{2W} \sinh \frac{\pi y}{2W} \\
 \alpha_0 &= \cos \frac{\pi a}{2W} \\
 \xi &= \sqrt{(\alpha^2 - \beta^2 - \alpha_0^2)^2 + 4\alpha^2\beta^2} \\
 \eta &= \arctan \frac{-2\alpha\beta}{\alpha^2 - \beta^2 - \alpha_0^2}
 \end{aligned} \tag{57}$$

The heat source is proportional to the square of the gradient of ϕ and behaves asymptotically as $1/r$ near the crack tip where r is the distance from the crack tip. At points distant from the crack, the heat source magnitude approaches a constant value of ϕ_0 .

The temperature fields induced by this heat source are calculated with the finite difference routine described in detail in the previous chapter. However, the singularity of the heat source at the crack tip may cause some numerical complications which were not addressed by the verifications of the finite difference method already described. Because of this, it is important to evaluate the convergence of the temperature solution with this type of behavior in the forcing function. To do this, we consider a problem in which the heat source term varies as $1/r$ and a closed-form solution is obtainable, and compare the solution with the numerically determined values in which the appropriate boundary conditions are input. The problem we consider is the temperature distribution in a cracked disk, the region of interest readily defined in cylindrical coordinates:

$$R = \{r, \theta | 0 < r < 1, -\pi < \theta < \pi\} \tag{58}$$

with the crack located along the line $\theta = \pi, 0 < r < 1$.

We seek then, the solution to the heat conduction equation with a sinusoidally varying heat source which behaves as $1/r$:

$$\nabla^2 T = \frac{\partial^2 T}{\partial r^2} - \frac{1}{r} \cos \omega t \tag{59}$$

where the temperature, $T = T(r, \theta, t)$. We constrain the temperature on the disk boundary to be zero and the crack faces to be insulated. The solution is obtained by separation of variables technique and is a Bessel function of the first kind, of zero order, in r . The steady state distribution is found to be:

$$T = \sum_{n=0}^{\infty} \frac{H_n}{\lambda_n^4 + \omega^2} \left[\lambda_n^2 \cos \omega t + \omega \sin \omega t \right] J_0(\lambda_n r) \quad (60)$$

where the coefficients, H_n , are defined by Fourier series representation,

$$H_n = \frac{2 \int_0^1 J_0(\lambda_n r) dr}{[J_1(\lambda_n)]^2} \quad (61)$$

the eigenvalues, λ_n , are the zeros of the equation $J_0(\lambda_n) = 0$, and J_1 is the first order Bessel function of the first kind.

To obtain this temperature distribution numerically, we specialize now to the geometry of the center-cracked plate and input the appropriate gradients of the above distribution along the vertical edges and the appropriate temperature values along the top edge as boundary conditions in the finite difference code. We then check spatial convergence by performing the finite difference calculations using different mesh sizes. Four mesh sizes of uniform refinement were employed: 1/12 (coarse), 1/24 (medium), 1/48 (fine), 1/96 (superfine).

Since the crack tip is the singular point of interest, we check convergence of the solution at that location and perform the analysis for three different frequencies: $\omega = 0, 4, 8$. The results of the convergence check are listed in Table 13. The values are normalized by the exact value from the closed form solution for the cosine temperature component, T_c and for the sine temperature component, T_s . The results show good convergence with errors less than 1 per cent for the cosine component and on the order of 2 per cent for the sine component for the superfine mesh.

Stress Intensity Results

With the verification of the finite difference method, we can perform stress intensity calculations with the electric potential heat source as the forcing function in the conduction equation and the temperature constrained to be zero on the ends. The results of these calculations are listed in Table 14 for the center cracked problem for the normalized crack length of 1/3. In order to compare the stress intensity values, we again normalize by the crack tip temperature. These data are plotted in Figure 9 and show that when a specific temperature is maintained at the center of the specimen, the stress intensity factor increases with the frequency. This contrasts with the results of the uniform heat problem in which the stress intensity decreased when a specific temperature is maintained at the center line (Figure 5).

The reason for this increase is apparent from the temperature fields generated by the electric current. The electric potential method of heating gives a temperature field which is spatially dependent in both x- and y- directions. This is different from the uniform heating method which gives a one-dimensional temperature field (for the symmetric case). The gradients in the temperature in the x-direction increase with the frequency as shown in Figure 10 and the magnitude of the stress intensity is governed by the size of the temperature gradient.

In order to compare the uniform heat stress intensities with resistance heat stress intensities for the case of a specified end temperature maintained, we use the superposition procedure described in Equations (41) through (44) and the data of Table 14 and Table 3. The two examples considered in Section II for uniform heating are again investigated here. These are the temperature at the crack tip (i) in phase with the end temperature and (ii) out of phase with the end temperature. The data of Table 3 are used in conjunction with those of Table 14 in the superposition and the results are plotted in Figures 11 and 12. Comparing these results with the similar results obtained in the uniform heat problem, we observe that there is a difference. First, for the static case where the temperature at the center is in phase with the end temperature, the uniform heat solution gives zero stress intensity. This is not the case when the specimen is heated electrically because of the presence of non-zero temperature gradients in the x-direction. Secondly, the stress intensity of electrically heated specimens is observed to increase with the frequency, rather than decrease as in the uniformly heated specimens.

Unlike the uniform heat problem, with the electric resistance method of heating we have an opportunity to avoid direct measurement of the temperatures by analytically estimating the temperature values at the specimen end. For example, we can estimate this

temperature as the far-field temperature in an equivalently heated long strip⁸. The far-field solution in this case is:

$$T(x,y,t) = \frac{\sigma}{k} \phi_0^2 \frac{D}{\omega} \sin \omega t \quad (62)$$

If this temperature is taken as the end temperature, the stress intensity factor in a cracked plate with electric current heating can be estimated without directly measuring the plate temperatures⁹. We again use the superposition equations (41) through (44). The results of this superposition, where the stress intensities are normalized by the temperature at the crack tip, are plotted in Figure 13 and show the stress intensity asymptotically approaches zero as the frequency approaches zero and peaks at a normalized frequency of approximately 4.0.

It is apparent from Figure 13 that the oscillating stress intensity variation with frequency behaves differently from the observed monotonic variation of the case when a zero end temperature is prescribed (as in Figure 5). We can attribute this to the inverse dependence of the magnitude of the far-field temperature on frequency and to the importance of the phase lag of the end temperature with respect to the crack tip temperature. These two effects are manifested in three regions of the frequency, as shown in Figure 13. At very low frequencies, the end temperature is quite high (from Equation (62)) and the resulting superposition is similar to the case of a harmonic temperature applied at grips with no heat source. Since the thermal gradients are small with this mode of heating, the stress intensity factors are also small.

On the other hand, as the frequency gets large, it is clear from Equation (62) that the end temperature gets quite small. In this case, the centerline temperature is driven solely by the electric resistance heat source and the solution approaches that of the resistance heat source problem with zero end temperature (evidenced by the closeness of the solutions at frequencies greater than 16). In the middle of the frequency regime, the phase difference between the end and center temperatures plays an important role. When the temperatures are out of phase, large thermal gradients exist in the specimen causing the stress intensities to be quite large.

⁸This procedure is less accurate but has the advantage that it requires less information than the direct measurement method. In other words, it is only necessary to know the temperature range over which the specimen is cycled in order to estimate the stress intensity.

⁹In practice, the end grips are cooled and consequently the temperatures may be significantly different from those used in this estimate.

Crack length scaling

We again investigate how the stress intensity scales with crack length by performing the above calculations with a normalized crack length of 1/6. The results of the electric potential stress intensity and crack tip temperature calculations for the case in which the end temperature is zero are listed in Table 15. The results of the superposition with the far-field temperature data are shown in Figure 14. Comparing these results with those in Figure 11 it is evident that the stress intensity again scales approximately as $a^{1/2}$ at low frequencies but the scaling is frequency-dependent. At the higher frequencies (< 8.0), the stress intensity scales more closely to a factor of a .

Summary of Results

In this section, we evaluated the difference between heat lamp and electric potential methods of cycling the temperature in a specimen. In general, the stress intensity of electrically heated specimens increases with frequency rather than decreases as in heat lamp heated specimens. Further, the scaling of stress intensity with crack length varies with the frequency, scaling as $a^{1/2}$ at low frequencies and as a at higher frequencies.

Table 13

Convergence check of finite difference solution for singular heat source.

Precise value is 1.0

mesh size	$\omega = 0$		$\omega = 4$		$\omega = 8$	
	T_c	T_s	T_c	T_s	T_c	T_s
coarse	0.9557		0.9374		1.0273	
medium	0.9720		0.9628		1.0046	
fine	0.9814		0.9850		0.9904	
superfine	0.9989		1.0017		0.9830	
					1.0088	
						0.9793

Table 14
Dimensionless stress intensity factor and temperature field results

Electric potential heat source, $a/W = 1/3$

$$\tau_0 = \frac{\sigma}{k} \Phi_0^2 L^2$$

Center Crack				
ω^*	K	Φ	T_1	Φ_1
	(x 10 ⁻³)	(radians)	(radians)	
0	34.560	-3.141	0.537	0.0
0.01	34.639	-3.126	0.537	0.0129
0.1	34.365	-2.987	0.533	0.129
0.5	29.207	-2.436	0.453	0.577
1.0	21.536	-1.958	0.330	0.925
1.5	16.381	-1.639	0.247	1.117
2.0	13.135	-1.400	0.193	1.232
3.0	9.513	-1.041	0.132	1.361
4.0	7.614	-0.771	0.098	1.427
8.0	4.685	-0.081	0.046	1.483
16.0	2.964	0.527	0.0225	1.382
32.0	1.778	0.980	0.0126	1.224

Table 15
Dimensionless stress intensity factor and temperature field results

Electric potential heat source, $a/W = 1/6$

$$\tau_o = \frac{\sigma}{k} \phi_o^2 L^2$$

ω^*	K	Φ	T_1	Φ_1
	($\times 10^{-3}$)	(radians)	(radians)	
0	38.479	-3.141	0.507	0.0
0.01	38.478	-3.127	0.507	0.013
0.1	38.171	-2.995	0.503	0.130
0.5	32.435	-2.476	0.427	0.584
1.0	23.695	-2.040	0.311	0.939
2.0	13.899	-1.558	0.182	1.262
4.0	7.146	-1.034	0.092	1.485
8.0	3.500	-0.434	0.042	1.591
16.0	1.840	0.120	0.020	1.574
32.0	1.137	0.505	0.010	1.522

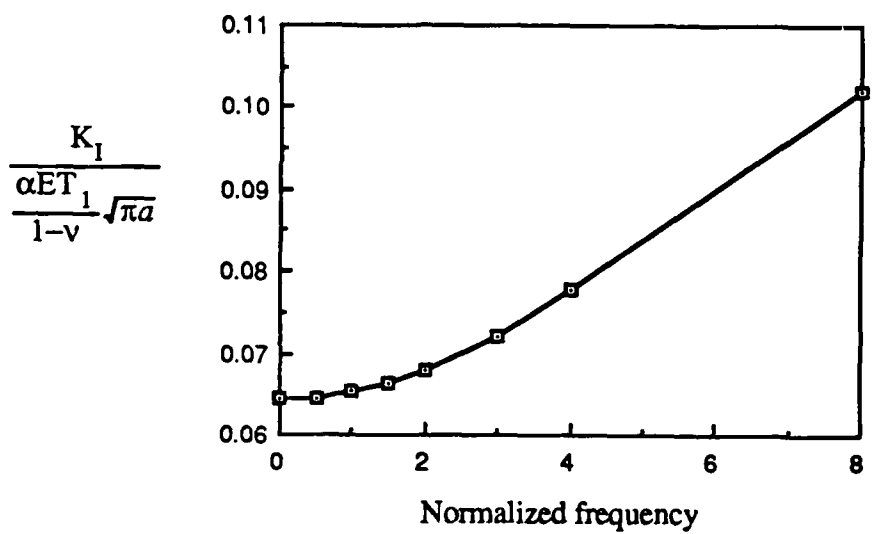


Figure 9. Stress intensity normalized by the temperature at the crack tip.

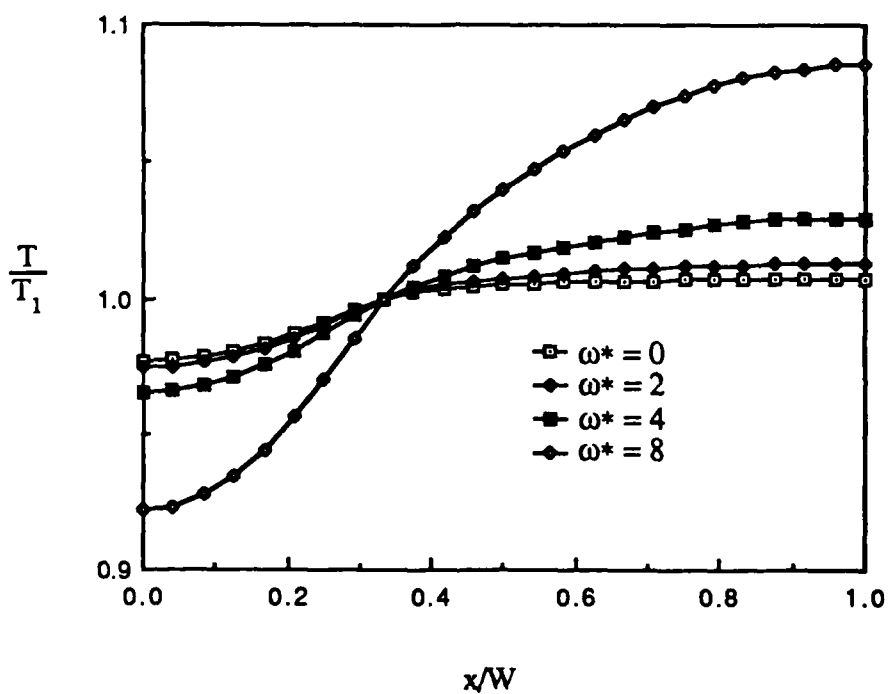


Figure 10. Magnitude of the electric potential temperature field along the x-axis for different normalized frequencies

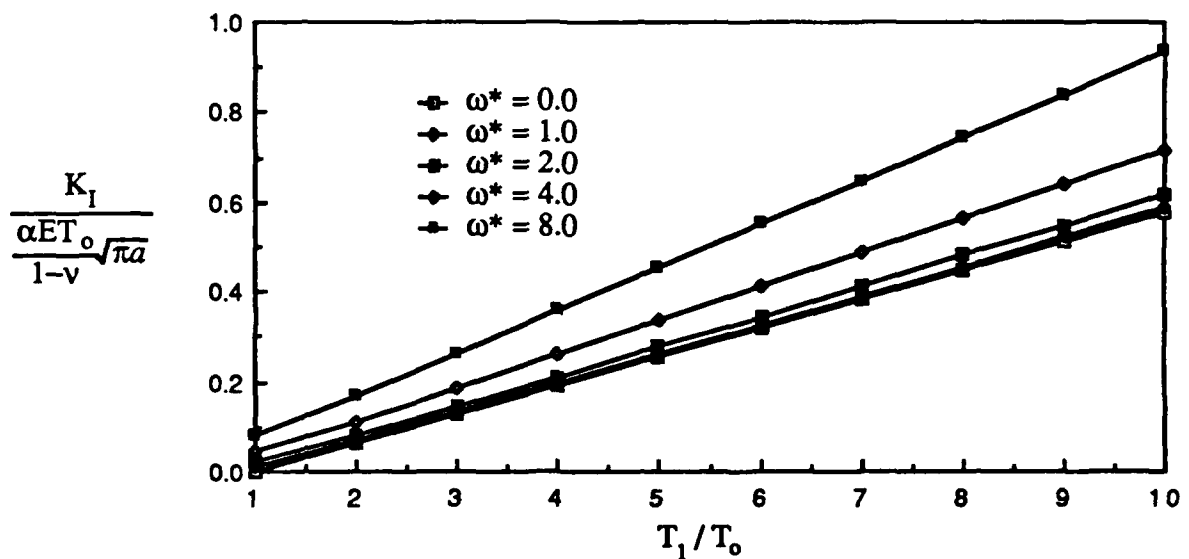


Figure 11. Amplitude of the stress intensity as a function of crack tip temperature and dimensionless frequency. The temperature at the crack tip, T_1 , is maintained by electric potential heating and is in phase with the end temperature, T_0 .

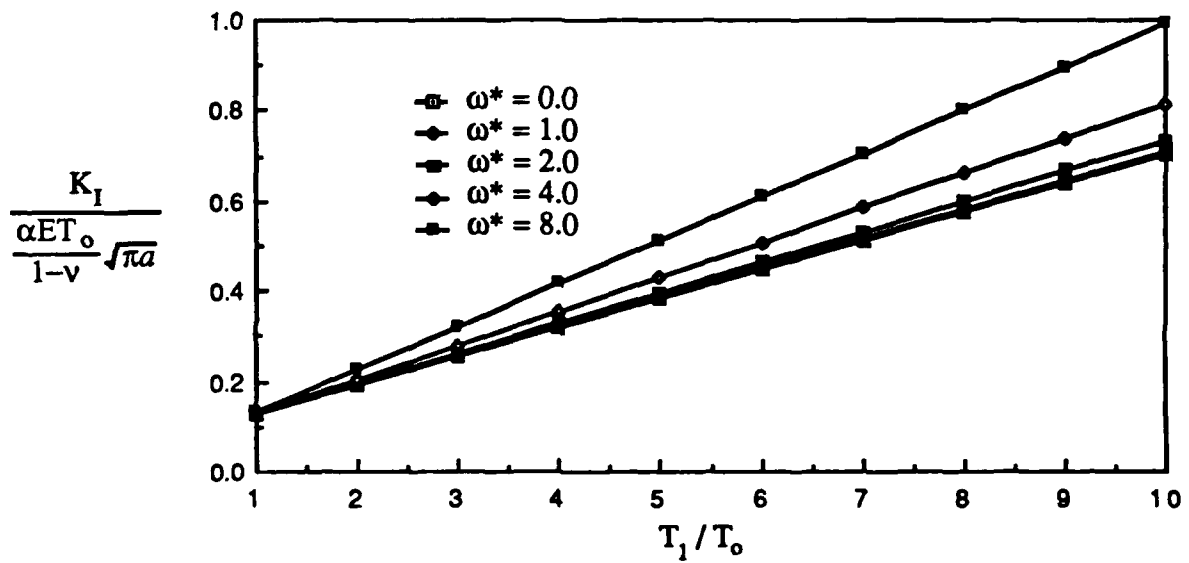


Figure 12. Amplitude of the stress intensity as a function of crack tip temperature and dimensionless frequency. The temperature at the crack tip, T_1 , is maintained by electric potential heating and is 180° out of phase with the end temperature, T_0 .

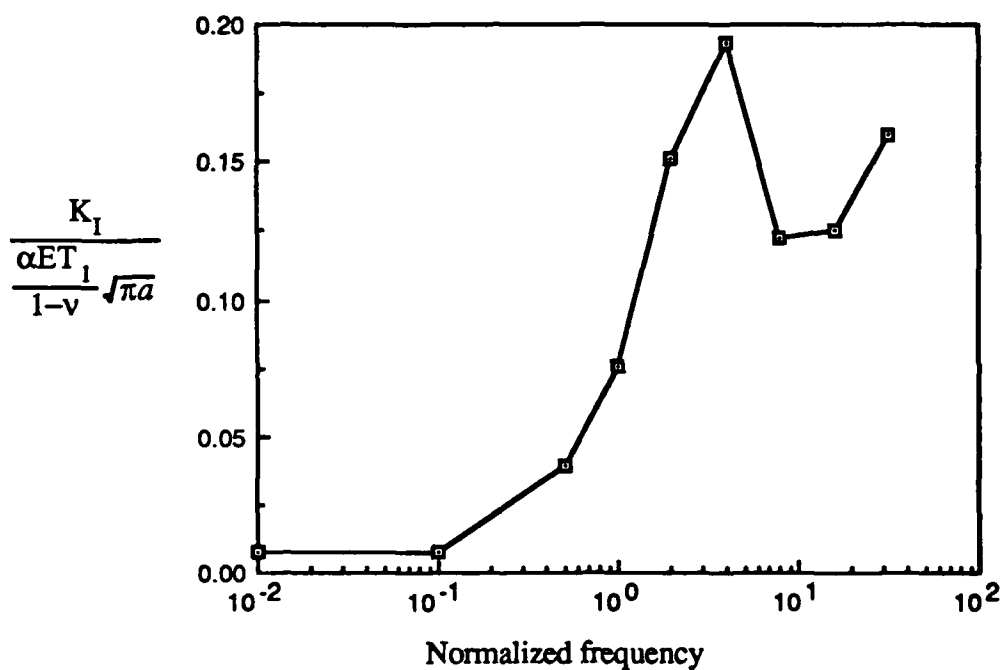


Figure 13. Stress intensity normalized by crack tip temperature for $a/W = 1/3$.

The temperature at the end is taken as the far-field solution of Equation (62).

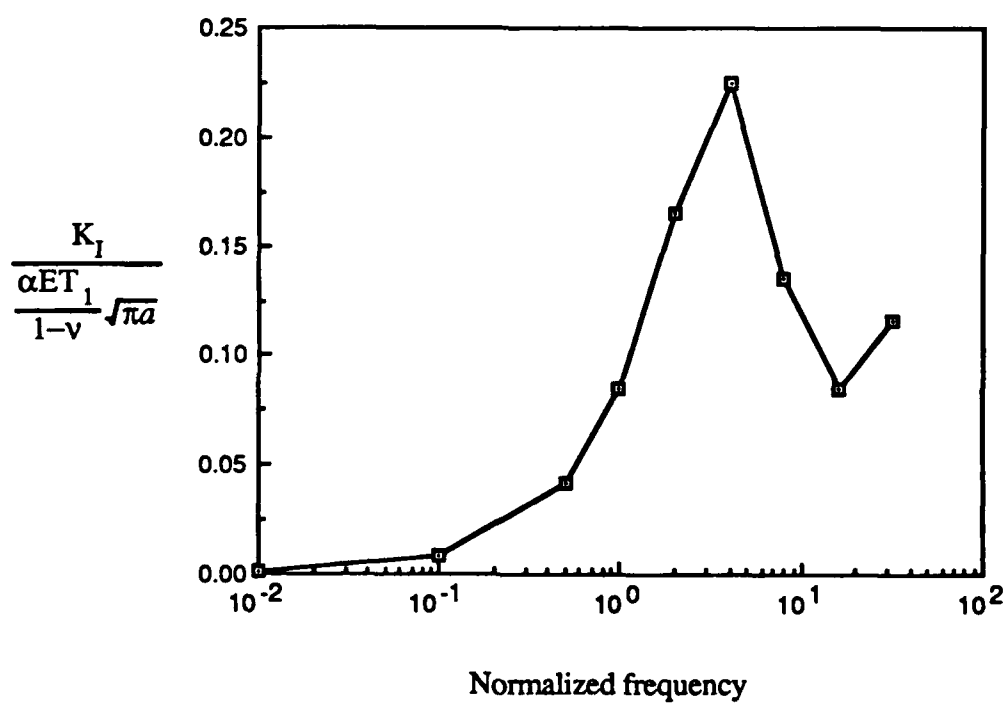


Figure 14. Stress intensity normalized by crack tip temperature for $a/W = 1/6$. The temperature at the end is taken as the far-field solution of Equation (62).

V. IMPLICATIONS FOR FATIGUE TESTING

An accurate and computationally efficient method for determining the effect of cyclic thermal loading on crack tip stress fields has been developed and has been used to estimate the effect of simple thermal transients on crack tip stress states. The method is generally applicable since it enables calculation of stress intensity values for any frequency of the thermal loading, can be used for both singly- and multiply-connected regions, and gives a dimensionless result that applies to all linear elastic homogeneous materials.

The results of the foregoing analyses indicate that stress intensity factors of cracked components exposed to thermal fatigue loading conditions have a significant dependence on the frequency of the thermal cycle. The dependence is greatest for electric potential heating methods due to the large gradients in temperature induced by the singular heat source. The fundamental difference in the dependence is that the stress intensity induced by uniform heating decreases with frequency while the stress intensity induced by electric heating increases with frequency. In addition, the scaling of the stress intensity with crack length for electric heating is found to depend, to some extent, on frequency. This contrasts with uniform heating in which the stress intensity invariably scales as $a^{1/2}$.

A primary goal of our analysis is to provide estimates of the thermal contribution to the stress intensity factor in thermo-mechanical fatigue testing. With these estimates, we can compare thermally induced stress intensities to those induced by mechanical loading. An introduction to these calculations is accomplished by considering the example case described in Wilson and Warren [21]. Samples of IN100 were thermo-mechanically fatigued within the temperature range of 300°F - 1000°F at thermal frequencies of 0.5 cycles per minute, (with the specimen dimensions and material data given, this corresponds approximately to a normalized frequency, $\omega^* = 2.0$). The maximum stress intensity occurs at the critical crack length, roughly one-third the sample width, and has a value of approximately 80 ksi $\sqrt{\text{in.}}$. Comparing these data to the data presented in Section II (uniform heat problem), a normalized value of stress intensity 20% that of the maximum mechanically induced stress intensity value reported would correspond to about 0.15. From Figure 6, if the centerline temperature is in phase with the far-field temperature, the temperature at the crack tip would have to be at least twice as great as the magnitude of the

temperature cycle. If the two temperatures were out of phase, however, the centerline temperature need only be equal to the far-field temperature in order to result in this magnitude of stress intensity.

By way of a second example, we consider actual thermal fatigue data and superposition to estimate the stress intensity factor for another case. Practically, the information required for the superposition and stress intensity calculations can be obtained by appropriately placing thermocouples to measure the temperature and phase relations at two locations (at the crack tip and at the specimen grips). We have obtained this information for titanium sheet samples from the Materials laboratories at the Wright-Patterson Air Force Base. The experiment consisted of 1.5 by 3 inch center-cracked specimens (Ti-6 Al-4 V) which were heated by four symmetrically placed lamps at two frequencies: 2.8 min per cycle (21.4 cycles per hour) and 7.4 min per cycle (8.1 cycles per hour). Thermocouples placed at both ends of the specimen confirmed the symmetry of the temperature distribution. The temperature ranges for the two cases at the two locations are as follows:

Frequency (cy/hr)	Crack tip		Grip location	
	T _{min}	T _{max}	T _{min}	T _{max}
8.1	290°F	870°F	110°F	230°F
21.4	360°F	870°F	135°F	225°F

In each case, no measurable phase lag was noted. Retesting confirmed consistency of the results.

We apply this information and the data in Tables 3, 4 and 14 to the superposition Equations (41) through (44) to evaluate the Mode I thermally induced stress intensity factor for these particular cases. For example, for the frequency of 8.1 cy/hr, T₀ = 60°F and T₁ = 290°F.

With the materials data for Ti-6 Al-4 V :

Elastic modulus (E)	16.6 x10 ⁶ psi
Density (ρ)	0.16 lb/in ³
Coefficient of thermal expansion (α)	5.1 x10 ⁻⁶ in/in/°F (at 600°F)
Thermal conductivity (k)	72.0 Btu in/ft ² /hr/°F (at 600°F)
Heat capacity (C _p)	0.125 Btu/lb/°F

actual estimates¹⁰ of the stress intensities can be made. The measured frequencies correspond to dimensionless frequencies of approximately 1.5 and 4.0. In order to make a direct comparison between uniform heating and electric resistance heating, we use the corresponding information for these frequencies from Tables 3, 4 and 14 to give the following estimates of the thermal stress intensities induced by the two different modes of heating:

Frequency	Uniform heating	Electric heating
8.1 cy/hr	1.76 ksi $\sqrt{\text{in.}}$	1.66 ksi $\sqrt{\text{in.}}$
21.4 cy/hr	1.52 ksi $\sqrt{\text{in.}}$	1.93 ksi $\sqrt{\text{in.}}$

These values may be compared to a fracture toughness of approximately 30 ksi $\sqrt{\text{in.}}$ for this particular alloy. The results above are consistent with the previous observation that the dependence of stress intensity factor on frequency is different for the two modes of heating and indicate that for higher frequencies, much larger errors in the overall stress intensity calculations may actually be occurring when electric resistance heating is used to cycle the specimen temperature in thermo-mechanical fatigue.

It is noted that the error from the dynamic temperature distribution contributes only a part of the total error stemming from the incorporation of thermal cycling in thermo-mechanical fatigue. This is because the temperature at the center does not oscillate about the same temperature as the end temperature. In fact, a static temperature gradient, which we approximate as parabolic in the y-direction, exists in addition to the dynamic oscillations about this gradient. Since the center of the specimen is measured as hotter than the end of the specimen, the stress intensity contribution from this static thermal gradient is negative. We can estimate this contribution using the static data of Table 4 and the materials information cited above as 12.5 per cent and 15 per cent of the fracture toughness for the dimensionless frequencies of 4 and 1.5, respectively.

Because the errors stemming from the dynamic part of the temperature distribution oscillate, they can either amplify or attenuate the total error induced by thermal cycling. In other words, since the static temperature yields a negative stress intensity and the error in the dynamic part can be positive or negative, summing the negative errors could give an overall error as much as about 25 per cent of the fracture toughness value. This means that

¹⁰The stress intensity values calculated are estimates in light of the assumption that the higher order terms in the Taylor's series expansion are considered small in comparison with the first term and the analysis was performed in plane strain while plane stress samples were used for testing.

the load cycle could be significantly lower than what is actually recorded. Further, since the applied maximum cyclic load often reaches only one-third to one-half the fracture toughness value, the error in the loading stemming from the cyclic thermal loads could, in fact, be significantly greater than 25 per cent.

As discussed in Section IV, the electric resistance method of heating gives an opportunity to avoid direct measurement of the temperatures by analytically estimating the temperature values at the specimen end as the far-field temperature in an equivalently heated long strip, Equation (62). If this temperature is taken as the end temperature, the stress intensity factor in a cracked plate with electric current heating can be estimated without directly measuring the plate temperatures.

It is interesting to compare this method of estimating thermally induced stress intensity factors with the method provided in [35], in which it is proposed that a static model problem be used to estimate the stress intensities induced by direct resistance heating. The results of this earlier analysis yielded axisymmetric temperature variations in the vicinity of the crack tip as $T(r) = T_b + T_e(1-r)$ which gives a resulting Mode I stress intensity factor as

$$K_I = 0.0914 \frac{\alpha E}{1-\nu} T_e \sqrt{\pi a}$$

where T_b is a constant temperature along a circular boundary at a radius of the half crack length, a , r is the dimensionless distance from the crack tip (normalized to a) and T_e is a temperature which is a function of the electrical and thermal conductivities of the specimen, the applied voltage drop per unit length and the crack length:

$$T_e = \frac{\sigma}{2k} (\phi_0 a)^2$$

With the test data and IN100 materials properties information presented in [35], the Mode I stress intensity factor at the highest voltage is calculated to be 3.8 ksi $\sqrt{\text{in.}}$.

We can estimate the Mode I stress intensity with the far-field approximation of the end temperature described above. If a complete thermal cycle is achieved in one minute then the normalized frequency corresponding to this rate of heating is approximately 4. Using the data of Table 14 and the superposition procedure described in Section II, K_I is calculated to be 3.8 ksi $\sqrt{\text{in.}}$. Although a comparison of the model problem estimate with this result shows a very close correlation for this particular case, the results depicted in Figure 13 show, in general, the model problem will give results within an order of magnitude of that predicted with the dynamic analysis discussed here.

It has been shown that, with the results presented, estimates of the thermal contribution to stress intensity in thermo-mechanical fatigue testing can be derived for a

wide variety of symmetric loading conditions. However, these calculations are not limited to symmetric temperature distributions. With the appropriate superposition and measurements of temperature at several locations within the sample, we can derive both Mode I and Mode II stress intensity values for asymmetric thermal loadings. It is of interest to evaluate how large the antisymmetric part of the temperature field has to be in order for the Mode II stress intensity to be significant compared to the Mode I value. In an example situation of a normalized frequency of 2.0, in order for the Mode I and Mode II stress intensities to be comparable, the antisymmetric end temperature would have to be five times greater than the symmetric end temperature and the center temperature five times less.

Geometrical variations have been investigated. We have found that edge-cracked specimens result in much lower stress intensity values (by a factor of approximately five) than the center-cracked specimens. This is probably due to the lack of restraint in bending that exists in the edge-cracked geometry that does not exist in the center-cracked plate.

In conclusion, the results of this analysis indicate that significant stress intensities may be induced by thermal fatigue loading. Further, the stress intensity values depend on the mode of heating used to cycle the specimen. Samples heated by direct resistance heating are subjected to a singular heat source at the crack tip which results in the stress intensity factor increasing with frequency. This behavior is opposite that of uniformly heated specimen and indicates that care should be taken when resistance heating is used at relatively high frequencies. The results obtained in the preceding sections may be used in conjunction with experimental data to improve predictions of stress intensity factors in laboratory fatigue tests and in actual fatigue service environments.

VI. A PILOT STUDY OF COMPOSITE MATERIALS

In the interest of understanding the effects of thermal transients in composite materials, an appropriate extension of the path independent integral approach is its application to bimaterial composites in which cracks occur normal to the bimaterial interface. We select this particular geometry for investigation because of its physical interest: it can correspond to the problem of a crack in the matrix or in a fiber, turning at or penetrating the interface between the fiber and the matrix; and because the corresponding eigenvalues are real. Real eigenvalues permit the interpretation of the eigenfunctions in terms of standard physical arguments since there is no oscillating singularity at the crack tip.

The isothermal problem of a composite with a crack normal to the interface has been studied by Hilton and Sih [28] for the case in which the crack does not extend to the interface, and by Cook and Erdogan [29] and Gupta [30] for the limiting case where the crack ends at the interface. In each case, the method of solution uses integral transform techniques to extract the stress intensity factors for different material combinations.

In our approach, we consider the relative importance of two thermal loading effects, those induced by dissimilar thermal diffusivities and dissimilar thermal expansions. In performing these parametric studies we are able to use the same techniques as those developed for the homogeneous case. Finite difference approximations will be derived for the temperature fields, which now depend on the ratio of the thermal diffusivities of the two materials. Finite element approximations will be obtained for the stress and displacement vectors which now depend on the ratio of the thermal expansions and the elastic moduli of the two materials. Finally, a path independent integral will be used to extract the stress intensity factors from the appropriate stress, displacement and temperature fields.

Formulation

In order to investigate the effects of transient thermal loadings on crack tip stress fields in composite materials, we follow Okajima [31] in formulating the following set of problems. First we consider the rectangular region in the x, y plane illustrated in Figure

15. By virtue of the symmetry of this configuration, we are able to limit the analysis to the region R : which is composed of two subregions R_1 and R_2 :

$$\begin{aligned} R &= R_1 \cup R_2, \\ R_1 &= \{(x,y) \mid -W < x < 0, 0 < y < L\} \\ R_2 &= \{(x,y) \mid 0 < x < W, 0 < y < L\} \end{aligned} \quad (63)$$

Once again we seek the two-dimensional thermoelastic stress and displacement vectors satisfying the plane uncoupled quasi-static equations of thermoelasticity. Reiterating the earlier formulation, we have the following equations for bimaterials. First, the temperature, $T(x,y,t)$ is defined by the heat conduction equation

$$\nabla^2 T(x,y,t) = \frac{1}{D_i} \frac{\partial T}{\partial t}(x,y,t) - H(x,y,t) \quad (64)$$

on R_i , $i = 1,2$, and boundary conditions which will be discussed later. Secondly, the stress vector satisfies the plane equations of equilibrium on R in the absence of a body force field (Equations (7)), and the stress and displacement vectors satisfy the plane-strain stress displacement relations:

$$\begin{aligned} \sigma_x &= \frac{2\mu_i}{(1-2\nu_i)} [(1-\nu_i) u_{,x} + \nu_i v_{,y}] - \beta_i T \\ \sigma_y &= \frac{2\mu_i}{(1-2\nu_i)} [(1-\nu_i) v_{,y} + \nu_i u_{,x}] - \beta_i T \\ \tau_{xy} &= \mu_i (u_{,y} + v_{,x}) \end{aligned} \quad (65)$$

on R_i , $i = 1,2$. The stress and displacement vectors satisfy traction-free boundary conditions on the outer edges and along the crack face:

$$\begin{aligned} \sigma_x &= \tau_{xy} = 0 \text{ on } x = \pm W, (0 < y < L) \\ \sigma_y &= \tau_{xy} = 0 \text{ on } y = L, (-W < x < W) \\ \sigma_y &= \tau_{xy} = 0 \text{ on } y = 0, (-W < x < 0) \end{aligned} \quad (66)$$

and symmetry conditions along the positive x -axis:

$$v = \tau_{xy} = 0 \quad \text{on } y = 0, (0 < x < W) \quad (67)$$

Finally, the two regions are considered perfectly bonded and so must obey continuity requirements at the interface:

$$\lim_{x \rightarrow 0^+} \sigma_x = \lim_{x \rightarrow 0^-} \sigma_x, \quad \lim_{x \rightarrow 0^+} \tau_{xy} = \lim_{x \rightarrow 0^-} \tau_{xy} \quad (0 < y < L), \quad (68)$$

and

$$\lim_{x \rightarrow 0^+} u = \lim_{x \rightarrow 0^-} u, \quad \lim_{x \rightarrow 0^+} v = \lim_{x \rightarrow 0^-} v \quad (0 < y < L) \quad (69)$$

where 0^+ implies $x > 0$, and 0^- implies $x < 0$.

Again, we refer to the stress intensity factor for evaluating the importance of transient temperature fields on crack tip stresses. Herein we deviate from homogeneous behavior. For cracked non-homogeneous solids with different elastic moduli the eigenvalue is no longer equal to 1/2. If we denote λ as the singular eigenvalue characterizing the only singular stress field at the crack tip, the stress intensity factor for composite materials, K_λ is defined as

$$K_\lambda = \lim_{x \rightarrow 0^+} \sqrt{2\pi} x^{1-\lambda} \sigma_y \quad \text{on } y = 0 \quad (70)$$

Evaluation of the eigenvalues and eigenfunctions

In order to determine the eigenvalues for the present case, we refer to the analysis of Dempsey and Sinclair [32] and specialize to our geometry. Substituting $\theta_1 = \pi/2$ and $\theta_2 = \pi$ into Equation 1-A-4 on page 323 of their analysis, we obtain the transcendental equation for λ as a function of material constants μ_i and v_i , $i = 1, 2$:

$$\sin^2 \frac{\lambda\pi}{2} (\beta^2 - 1) + \lambda^2 (\beta - \beta^2 - \alpha + \alpha\beta) + \frac{1+\alpha}{2} = 0 \quad (71)$$

In (71), α and β are defined as combinations of μ_i and v_i ,

$$\alpha = \frac{\mu_2 m_1 - \mu_1 m_2}{\mu_2 m_1 + \mu_1 m_2} , \quad \beta = \alpha - 2 \frac{\mu_2 - \mu_1}{\mu_2 m_1 + \mu_1 m_2} \quad (72)$$

In plane strain, $m_i = 4(1-v_i)$. The composite material parameters were first defined in this way by Zak and Williams [33]. It is noted that Equation (71) is identical to the transcendental equation derived in the analysis of Cook and Erdogan. The limiting values of α and β are determined by the physical restrictions of v_i ($0 < v_i < 0.5$), and μ_i ($0 < \mu_i < \infty$). Substituting these values into (72) gives $-1 < \alpha < 1$, and $(\alpha-1) < 4\beta < (\alpha+1)$. Several eigenvalues satisfying (71) for this range of material parameters are shown in Figure 16.

To determine the eigenfunctions associated with the eigenvalues, we turn to the work of Williams [4]. The results, best presented in the cylindrical coordinate system ($x = r \cos \theta$, $y = r \sin \theta$), are reported here.

$$\begin{aligned} \sigma_r^i &= \frac{K_\lambda r^{\lambda-1}}{\sqrt{2\pi} \lambda (\lambda+1) b} [f_i''(\theta; \lambda) + (\lambda+1) f_i'(\theta; \lambda)] \\ \sigma_\theta^i &= \frac{K_\lambda r^{\lambda-1}}{\sqrt{2\pi} \lambda (\lambda+1) b} [\lambda (\lambda+1) f_i(\theta; \lambda)] \\ \tau_{r\theta}^i &= \frac{K_\lambda r^{\lambda-1}}{\sqrt{2\pi} \lambda (\lambda+1) b} [-\lambda f_i'(\theta; \lambda)] \\ u_r^i &= \frac{K_\lambda r^\lambda}{2\sqrt{2\pi} \lambda (\lambda+1) b \mu_i} [-(\lambda+1) f_i(\theta; \lambda) + \frac{1}{4} m_i g_i'(\theta; \lambda)] \\ u_\theta^i &= \frac{K_\lambda r^\lambda}{2\sqrt{2\pi} \lambda (\lambda+1) b \mu_i} [-f_i'(\theta; \lambda) + \frac{1}{4} m_i (\lambda-1) g_i(\theta; \lambda)] \end{aligned} \quad (73)$$

in R_i , $i = 1, 2$. The prime denotes differentiation with respect to θ and the functions, $f_i(\theta; \lambda)$ and $g_i(\theta; \lambda)$ are

$$f_i(\theta; \lambda) = b_{i1} \sin(\lambda+1)\theta + b_{i2} \cos(\lambda+1)\theta + b_{i3} \sin(\lambda-1)\theta + b_{i4} \cos(\lambda-1)\theta \quad (74)$$

$$g_i(\theta; \lambda) = \frac{4}{\lambda-1} [-b_{i3} \cos(\lambda-1)\theta + b_{i4} \sin(\lambda-1)\theta] \quad (75)$$

where $b = b_{22} + b_{24}$. and the constants b_{ij} , $i=1,2$, $j = 1,2,3,4$, are determined from the traction and displacement boundary conditions:

$$\begin{aligned}
 b_{21} &= b_{23} = 0 \text{ (from symmetry)} \\
 b_{24} &= 1 \\
 b_{22} &= B \\
 b_{14} &= \frac{1}{2A} \left\{ -(\lambda+1)[s^2(4s^2-3)-\lambda]b_{22} + [s^2(4\lambda s^2 - 5\lambda + 1) - \lambda^2 + \lambda]b_{24} \right\} \quad (76) \\
 b_{13} &= \frac{1}{2sc(2\lambda+1)} \left\{ [2(2\lambda+1)s^2 - 2\lambda]b_{14} + [2(\lambda+1)s^2 - \lambda - 1]b_{22} \right. \\
 &\quad \left. - (2\lambda s^2 - \lambda + 1)b_{24} \right\} \\
 b_{12} &= -4sc b_{13} - (1 - 4s^2)b_{14} + 2s^2(b_{22} - b_{24}) \\
 b_{11} &= \frac{s}{c} (b_{12} - b_{14} - b_{22} + b_{24}) + b_{13}
 \end{aligned}$$

for

$$\begin{aligned}
 A &= s^2 - \lambda^2 \\
 B &= \frac{[(2\beta+2)\lambda - 2\beta + 2]s^2 + 2(\alpha-\beta)\lambda^3 + (2\beta+\alpha-1)\lambda^2 - (\alpha+1)\lambda}{2(\beta+1)(\lambda+1)s^2 + 2(\alpha-\beta)\lambda^3 + (3\alpha-2\beta+1)\lambda^2 + (\alpha+1)\lambda} \\
 s &= \sin \frac{\lambda\pi}{2} \\
 c &= \cos \frac{\lambda\pi}{2}
 \end{aligned} \quad (77)$$

Finally, the path independent integral requires the divergence of the displacement eigenvectors, \mathbf{u}^i , $i=1,2$:

$$\nabla \cdot \mathbf{u}^i = \frac{r^{\lambda-1}}{\mu_i} \frac{K_\lambda}{\sqrt{2\pi}(\lambda+1)b} (m_i - 2) [b_{13} \sin(\lambda-1)\theta + b_{14} \cos(\lambda-1)\theta] \quad (78)$$

The complementary eigenfunctions, σ^i * and \mathbf{u}^i *, $i = 1,2$, are obtained by substituting $-\lambda$ for λ and a scaling factor, K_λ *, for K_λ in Equations (73) through (77).

We follow the procedure outlined in Section III for defining the appropriate path independent integral which extracts the stress intensity factor. By virtue of the continuity

requirements at the interface, the path independent integral is that of Equation (31) in which K is replaced by K_λ and the homogeneous complementary eigenfunctions are replaced by the complementary functions just developed:

$$K_\lambda = \sum_{i=1}^2 \left\{ \int_{\Sigma_i} [(\sigma_x u^{i*} + \tau_{xy} v^{i*} - \sigma_x^{i*} u - \tau_{xy}^{i*} v) n_x + (\sigma_y v^{i*} + \tau_{xy} u^{i*} - \sigma_y^{i*} v - \tau_{xy}^{i*} u) n_y] dS + \beta_i \int_{R_i} T(u^{i*},_x + v^{i*},_y) dA \right\} \quad (79)$$

where the integration paths, Σ_i , $i = 1, 2$, refer to the boundaries not including the crack faces, of the regions R_i , $i = 1, 2$, respectively. The scaling factors, K_λ^* , are determined by substituting the eigenfunctions themselves into (79), letting $T = 0$, and performing the integration.

To verify the accuracy of the established eigenfunctions and the path independent integral approach we analyze a check problem which utilizes the most strongly singular eigenvalue used in the intended application. We follow Okajima [31] in formulating the check problem which superimposes eigenfunctions, adjusting their participation so that a reasonable approximation of the boundary conditions used in the application results. The forms of the superposition are those of (73) with K_λ being replaced by the constants K_λ and C_2 corresponding to the eigenvalues λ_1 and λ_2 . Specifically, we choose the material combination corresponding to the most singular eigenvalue, the combination giving the ratio of elastic moduli of $E_2/E_1 = 0.14$. The first two eigenvalues associated with this combination are

$$\lambda_1 = 0.2816, \lambda_2 = 1.1077 \quad (80)$$

In combining the first two eigenfunctions to approximate a uniaxial tension loading on the region of interest, we take the participation of the first eigenvalue field, $K_\lambda = 1.0$ and the participation of the second, $C_2 = 0.25$. The traction conditions along the edge, then, are determined as the sum of these two eigenfunctions with the appropriate participation factor. The loading conditions for the check problem are shown in Figure 17.

To examine convergence of the solution we perform the analysis on three uniformly refined grids. A full description of the finite element grids used is contained in Appendix B. The results of the analysis demonstrate acceptable performance on the test problem. The value of K_λ for the coarse, medium and fine grids, are respectively 1.061, 1.029 and 1.018 (the exact value is 1.0).

Problem Definition

The goal of this analysis is to establish the importance of thermal diffusivity mismatches relative to mismatches in thermal expansion rates. In order to accomplish this, we pose two problems. In the first we consider the ratio of αE in each material to remain unity while the ratio of thermal diffusivity changes. In this case, a frequency dependence will be established. The eigenvalue will be limited to the case, $\lambda = 0.5$, since the the elastic moduli of the materials are equal. The heating conditions imposed are a uniform heat source varying as $h_0 \cos(\omega t)$ with all edges insulated. Although the static case ($\omega = 0$) gives an infinite temperature distribution, we will look at the behavior of the stress intensity factor as a function of frequency and study the limit as the frequency approaches zero. In the second problem we consider the ratio of thermal diffusivities of the two materials to be unity and evaluate the stress intensity factor for several ratios of thermal expansion and elastic moduli, since it is the combination of these material constants that gives rise to the magnitude of the thermal stresses in a material. In this problem, no frequency effects will result since the temperature is uniform throughout the composite. Once these preliminary relationships are established, we will evaluate the importance of diffusivity mismatches and expansion mismatches in some currently used composites.

Thus, in addition to the constraints imposed on the stress and displacement vectors presented in Equations (65) through (71), the following conditions on the temperature field satisfying Equation (63) will be imposed. First, the edges of rectangular geometry are taken to be thermally insulated.

$$\begin{aligned} T_x &= 0 \text{ on } x = 0 \text{ and on } x = W, \quad 0 < y < L \\ T_y &= 0 \text{ on } y = 0 \text{ and on } y = L, \quad 0 < x < W \end{aligned} \tag{81}$$

Secondly, either the heat generation term behaves harmonically and the ratio of thermal diffusivity varies between 0.1 and 10,

$$H(x,y,t) = h_0 \cos \omega t, \quad \alpha_1 E_1 / \alpha_2 E_2 = 1, \quad 0.1 < D_1 / D_2 < 10, \quad v_1 = v_2. \tag{82}$$

or the temperature remains uniform throughout the composite and the ratio of product of thermal expansion coefficient times the elastic modulus varies between the limits 0.1 and 10.

$$T(x,y,t) = T_0, D_1/D_2 = 1, 0.02 < \alpha_1 E_1 / \alpha_2 E_2 < 50, v_1 = v_2. \quad (83)$$

The limits on the ratios of material constants have been chosen to approximate to first order those of actual composite materials. Regardless of the material combination, we have taken Poisson's ratio to be the same in each material and equal to 0.3. This assumption simplifies the calculations required for determining the eigenvectors since their dependence is now reduced to one parameter: the ratio of the elastic moduli. In general, for the composite materials under consideration, Poisson's ratio varies very little between the two materials, ranging between 0.25 and 0.35.

Thermal Diffusivity Effects

Following the method of solution outlined in Section II, Equations (14) through (16), we represent the temperature, $T(x,y,t)$ as the sum of harmonic components in which ω is the frequency of the thermal excitation and $T_s(x,y)$ and $T_c(x,y)$ are the magnitudes of their respective components. The solution to the heat conduction Equation (63) with the imposed conditions of (81) and (82) for the limiting case, $D_2 = D_1 = D$, is straightforward:

$$T(x,y,t) = \frac{D}{W^2} \frac{1}{\omega} \sin \omega t \quad \text{for } \omega \neq 0, \text{ and} \quad (84)$$

$$T(x,y,t) = \frac{D}{W^2} t \quad \text{for } \omega = 0. \quad (85)$$

Clearly, T_s and T_c are undefined for the case the frequency is zero and are spatially constant for values of frequency not equal to zero ($T_s = D/(W^2\omega)$, $T_c = 0$). The resulting stress intensity factors, K_s and K_c , for this limiting case are zero since the plate is not restrained from uniform expansion.

For the general case of varying D_2/D_1 , the temperature solution is more complex. Finite difference solutions have been obtained for values of $D_2/D_1 = 0.1, 0.5, 5.0, 10.0$ for

a range of dimensionless frequencies from 0.03 to 2.55¹¹. These results are pictured in Figure 18 in which the temperature field is the amplitude of the harmonic components, $T = (T_s^2 + T_c^2)^{1/2}$ and has been normalized by the temperature amplitude at the crack tip, T_1 . Because of the insulation conditions on the y-faces of the plate, no temperature variation in the y-direction exists and the solutions illustrated in Figure 18 hold for all values of y. From these figures, a general trend of increasing temperature gradient with frequency is observed and as the frequency approaches zero, the temperature approaches a flat distribution. The variation of crack tip temperature with frequency for the different values of the diffusivity ratio is shown in Figure 19. Here, the dimensionless crack tip temperature has been normalized by the value $h_0 W^2$, h_0 is the magnitude of the heat source and W is the plate width. The crack tip temperature tends to increase to an unknown limit as the frequency approaches zero and its magnitude also increases with the diffusivity ratio.

From these temperature distributions, stress intensity factors were calculated using the same procedures detailed in Sections II and III. The finite element method was used to compute the stress and displacement fields associated with the temperature fields and the Mode I path independent integral (Equation (31)) was used to calculate the stress intensity factors from these fields. Uniform grid refinement was used for all calculations. The finite element grids are shown in Appendix B. Convergence behavior of the results was good and several paths of integration were used in the computations to demonstrate path independence. The results of the calculations are shown in Figure 20. In these figures, the stress intensity factor represented is the amplitude of the harmonic components: $K = (K_s^2 + K_c^2)^{1/2}$ and has been nondimensionalized by the crack tip temperature amplitude, T_1 :

$$K = \frac{K_I}{\frac{\alpha ET_1}{1-\nu} \sqrt{\pi a}} \quad (86)$$

The trend of increasing stress intensity with frequency follows from the temperature results: increasing thermal gradients with frequency. It is also noted that as the frequency approaches zero, so does the stress intensity.

Thermal Expansion Effects

¹¹ The dimensionless frequency, ω^* , is now normalized by the diffusivity of material 1 and thus is related to the frequency, ω , by the relation $\omega^* = \omega L^2/(D_1 \pi)$.

To investigate the effects of thermal loads in composite materials with mismatches in thermal expansion and elastic modulus, we first consider static, uniform temperature fields. Performing this preliminary study enables us to compare the importance of frequency effects relative to static loading effects since mismatches in expansion and elastic modulus do not affect the temperature field of the composite. Thus, we take the temperature in the composite, $T(x,y)$ to be a constant, T_0 , and the heat source, $H(x,y)$ to be zero. This field satisfies the heat conduction Equation (64) with the conditions of thermally insulated boundaries (Equations (81)) described in the problem definition. Further, we vary the ratio of the product of thermal expansion and elastic modulus between the limits of 0.02 to 50, as described in (83).

With this temperature field, stress intensity factors were calculated using the finite element method to compute the stress and displacement fields and the path independent integral of Equation (79). The case of uniform elastic modulus ($E_2 = E_1$) is interesting because the corresponding eigenvalue is 1/2. Results of the stress intensity calculations are shown in Figure 21 for this case. The results show that the stress intensity factor is linearly related to the difference in the thermal expansion coefficients of the two materials and is zero when the expansion coefficients are equal. From these data, the stress intensity factor is calculated to be

$$K_I = 0.28 \frac{E T_0}{1-v} (\alpha_1 - \alpha_2) \sqrt{\pi a} \quad (87)$$

For the case of equal thermal expansion and varying elastic modulus, no stress intensity exists since this corresponds to the case of uniform, unrestrained expansion. When the expansion coefficient is not uniform, however, the stress intensity factor can become quite large. Results of these calculations are shown Figure 22 along with the eigenvalues associated with each elastic modulus ratio used in the computations. The stress intensity values are normalized to the properties of material 1, the material containing the crack, and the uniform temperature in the plate:

$$K = \frac{K_\lambda}{-\frac{\alpha_1 E_1 T_0}{1-v} \sqrt{\pi} a^{1-\lambda}} \quad (88)$$

From Figure 22, we find that when the thermal expansion coefficient is larger in the uncracked material ($\alpha_2/\alpha_1 > 1$) the normalized stress intensity is greater than zero, in the crack-opening mode and is less than zero (crack closure) when the coefficient is larger in the cracked material.

Summary and Discussion of Results

In this section we have extended our approach of estimating thermal fatigue stress intensity factors to a composite material by performing a pilot study of bimaterial composite with a crack normal to the interface. Comparing the effects of diffusivity and expansion from these preliminary studies indicate that frequency effects are an order of magnitude lower than those induced by variations in elastic modulus and expansion. In order to investigate this further, we have chosen two composite systems which are currently being considered for use in thermal fatigue environments. These are composites of titanium with silicon carbide fibers and glass with silicon carbide fibers. Material properties for titanium, a high temperature glass trademarked VYCOR, and silicon carbide fibers are listed in Table 16. We consider two separate cases for each composite: the crack located in the matrix (Ti or glass) and the crack located in the SiC fiber. Ratios of the material parameters and the associated eigenvalues for these four cases are listed in Table 17. We have combined the thermal diffusivity problem now with the thermal expansion problem and have calculated the stress intensity factors induced by cyclic temperature fields where the heat source varies as $h_0 \cos \omega t$ and the elastic materials properties (E and α) are different for the two materials. Results of these calculations are shown in Figures 23 and 24. The stress intensity factors in these figures have been normalized by the amplitude of the crack tip temperature, T_1 , and elastic properties of the material with the crack, material 1 (Equation (88) with T_0 replaced by T_1). These figures illustrate that for higher frequencies, the effect of frequency on the stress intensity amplitude can be quite high. In the composite of titanium matrix composite, cyclic temperature fields reduce the stress intensity regardless of the location of the crack while different behavior is observed in the composite with the glass matrix. In this case, low frequencies cause the stress intensity factor to increase above the static value. This behavior continues at higher frequencies if the crack is located in the fiber while the stress intensity decreases at higher frequencies if the crack is located in the matrix material.

If we consider actual fatigue test frequencies of the order of 1 cycle per minute, the stress intensity relative to the static value can be estimated. These results are listed in Table 18. The effect at this frequency can be as great as increasing the stress intensity by 18 per

cent (for glass-SiC systems with the crack located in the SiC) or decreasing the stress intensity by 45 per cent (for Ti-SiC systems with the crack located in the Ti) or as small as a 2 per cent decrease (for glass-SiC systems with the crack in the glass).

Table 16
Material properties for example composites¹²

Material	Heat capacity (C _p)	Density (ρ)	Thermal		Elastic Modulus (E)
			(k)	Expansion (α)	
	$\frac{\text{cal}}{\text{g} \cdot ^\circ\text{C}}$	$\frac{\text{g/cc}}{\text{cm} \cdot \text{s} \cdot ^\circ\text{C}}$	$\frac{\text{cal}}{\text{cm} \cdot \text{s} \cdot ^\circ\text{C}}$	$10^6 \frac{\text{in}}{\text{in} \cdot ^\circ\text{C}}$	10^6 psi
Titanium	0.125	4.50	0.0052	8.5	16.8
Silicon Carbide	0.186	3.22	0.0400	5.0	70.0
VYCOR	0.180	2.18	0.0033	0.75	9.6

¹²The diffusivity, D, is related to the heat capacity, density and thermal conductivity by the relation, $D = k / (\rho C_p)$.

Table 17

Ratios of material properties and the associated eigenvalue for example composites

Material 1- Material 2	$\frac{D_2}{D_1}$	$\frac{\alpha_2}{\alpha_1}$	$\frac{E_2}{E_1}$	λ
Ti - SiC	7.23	0.59	4.17	0.6225
SiC - Ti	0.14	1.70	0.24	0.3419
Glass - SiC	7.95	6.67	7.29	0.6538
SiC - Glass	0.13	0.15	0.14	0.2793

Table 18

Stress intensity increase at a frequency of 1 cycle/min for example composites.

Composite	Crack location	Frequency, ω^*	Normalized ΔK
Ti - SiC	Ti	23.3	-17%
SiC - Ti	SiC	1.24	-45%
Glass - SiC	Glass	25.6	-2%
SiC - Glass	SiC	1.24	+18%

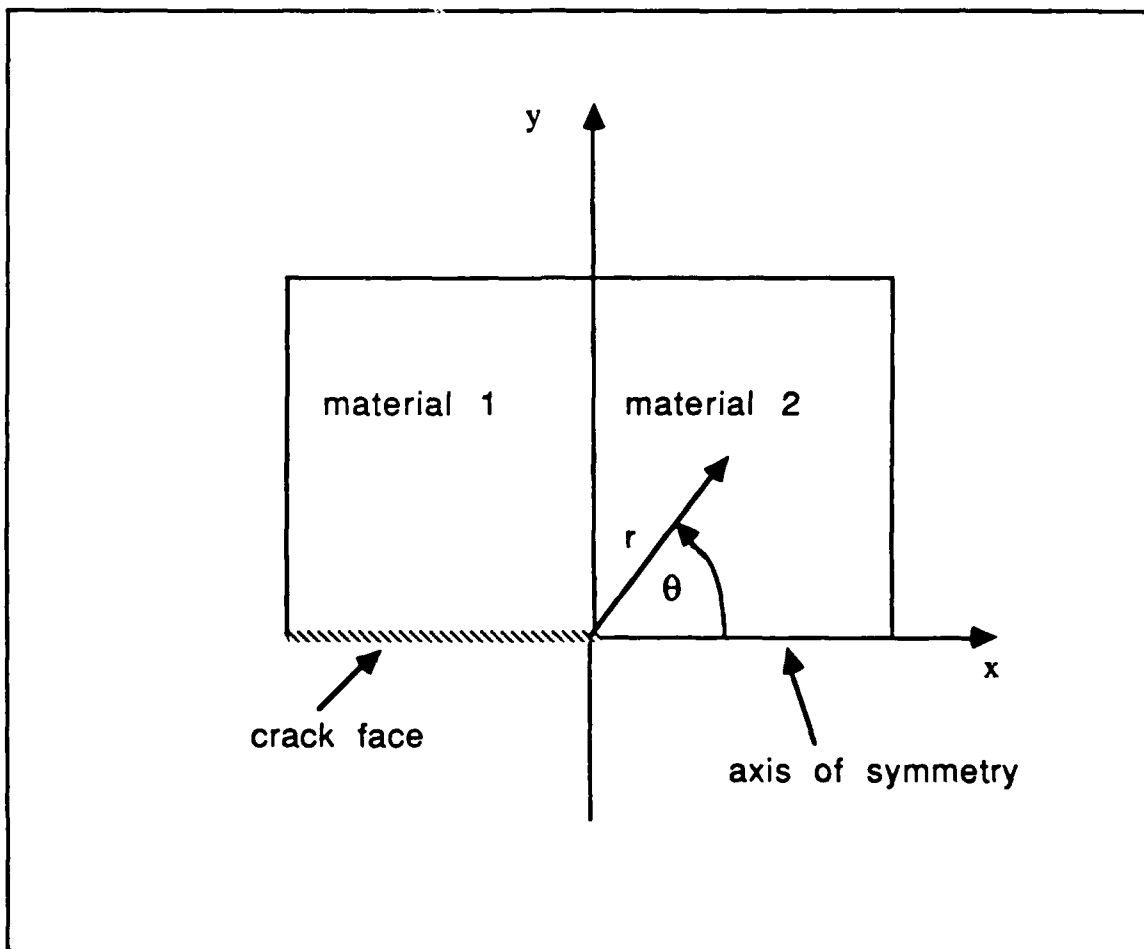


Figure 15. Geometry of the composite problem.

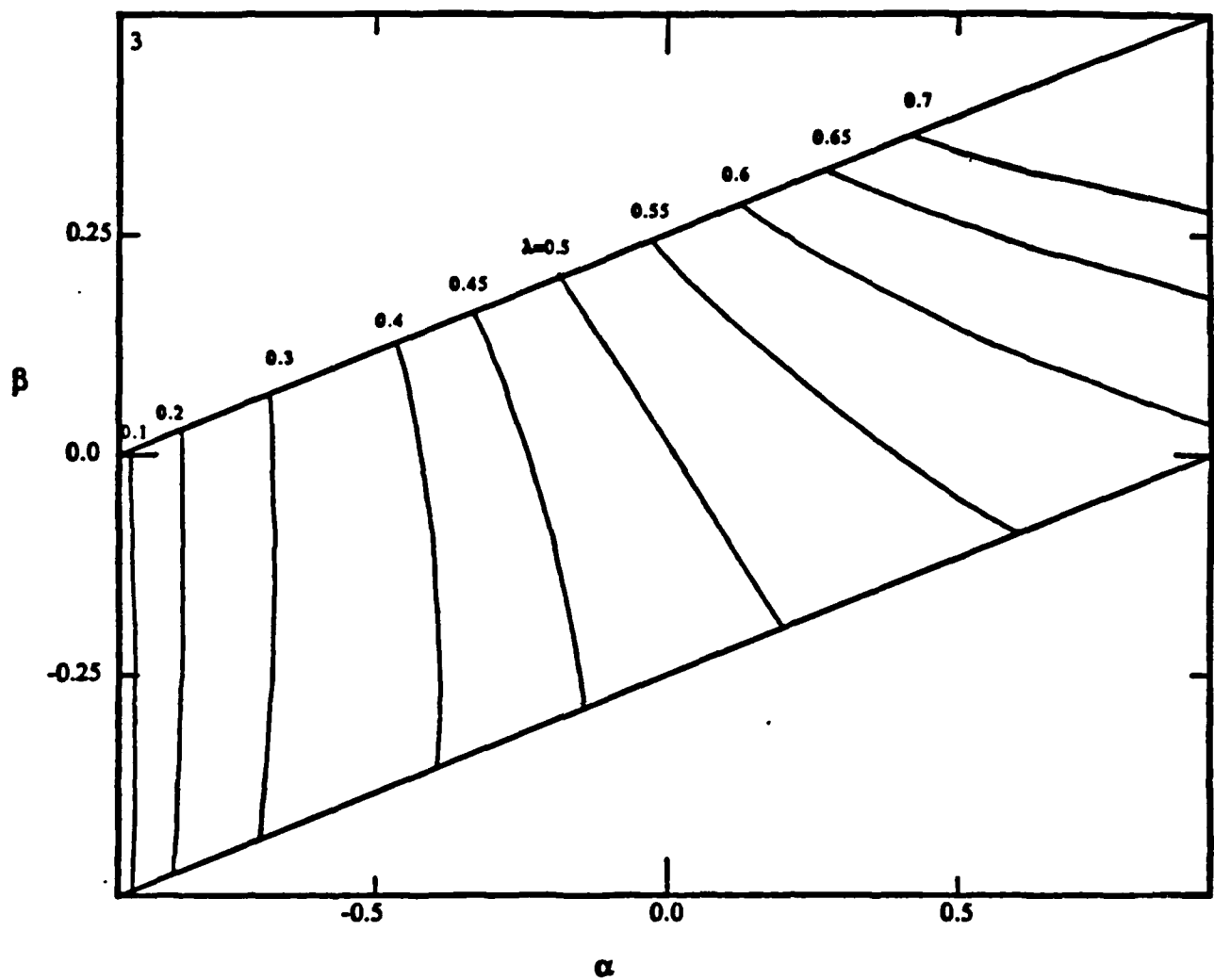


Figure 16. Dependence of the eigenvalue, λ , on material constants, α and β .

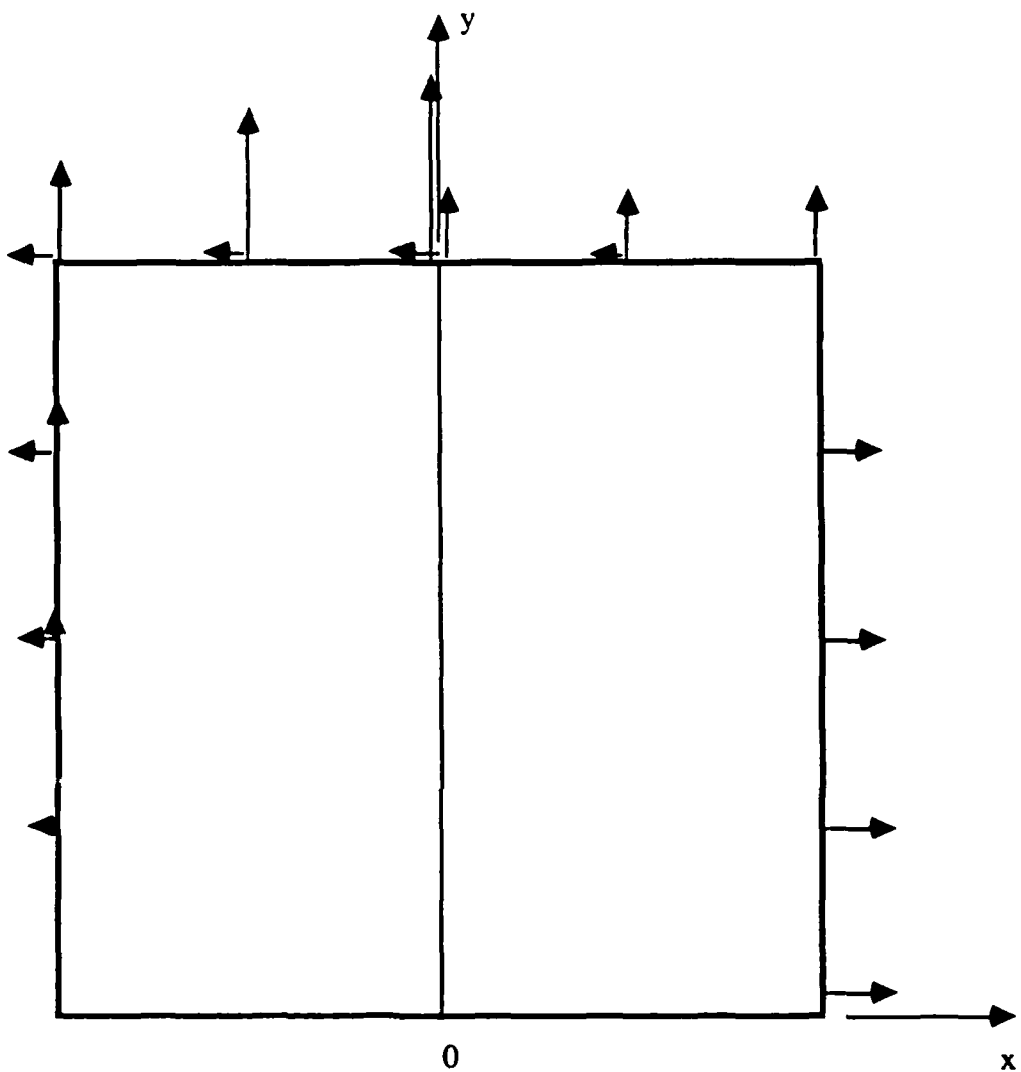


Figure 17. Traction conditions for the test problem.

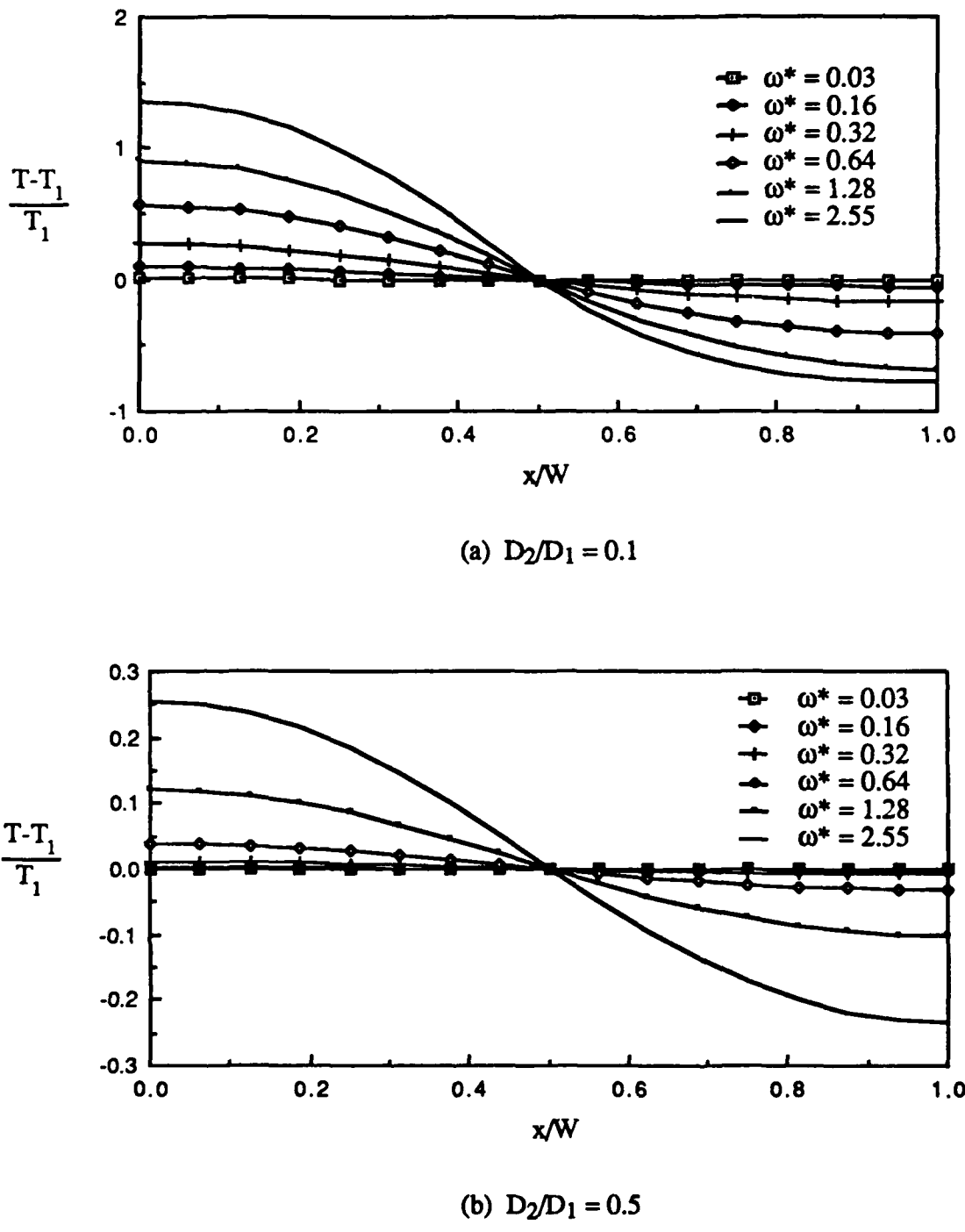


Figure 18. Temperature magnitude as a function of dimensionless frequency and diffusivity ratio for the composite problem.

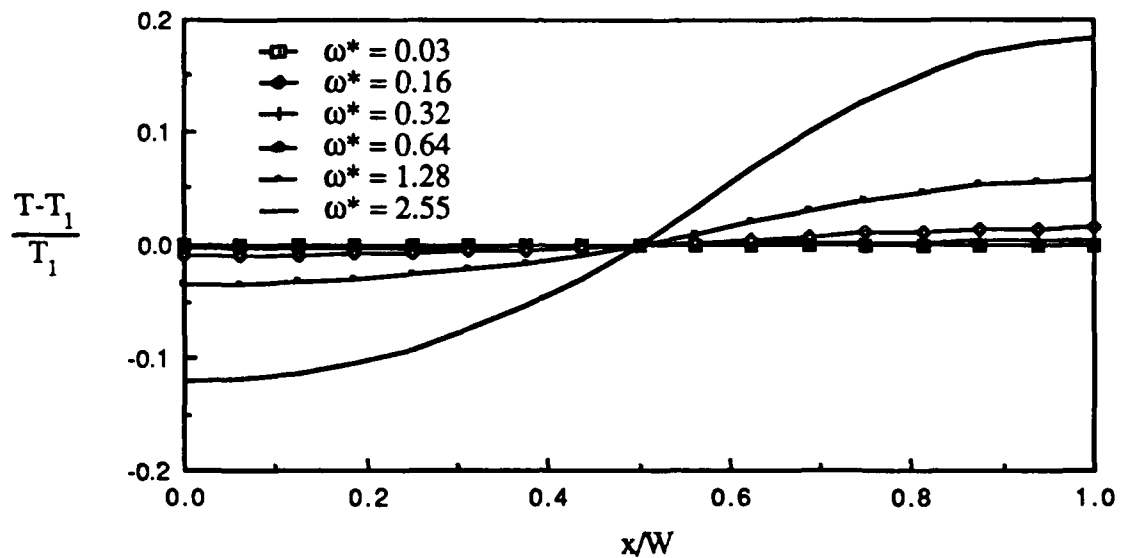
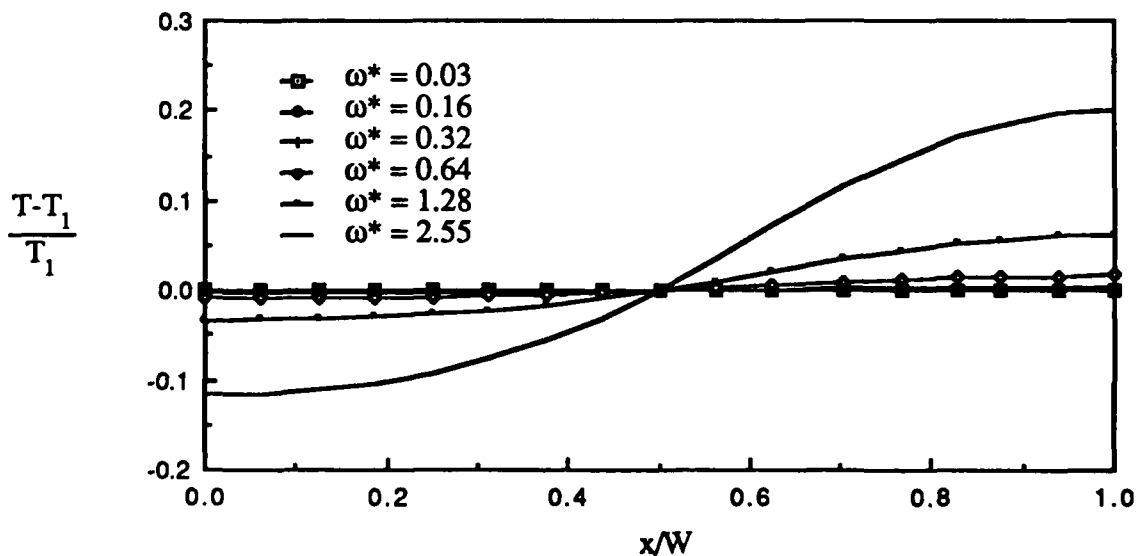
(c) $D_2/D_1 = 5.0$ (d) $D_2/D_1 = 10.0$

Figure 18. (continued).

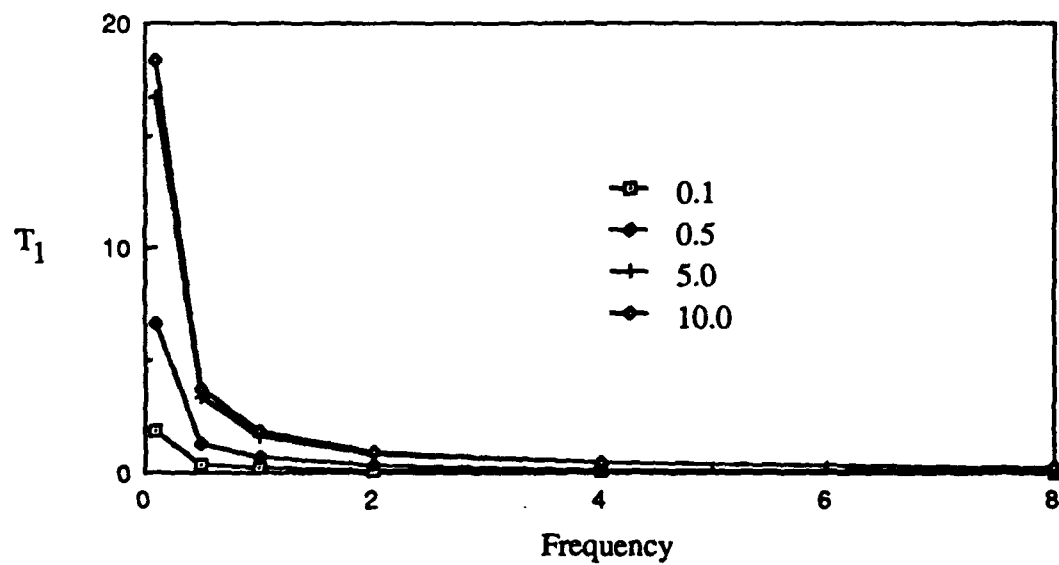


Figure 19. Variation of the crack tip temperature with frequency for the composite problem
for ratios of the diffusivity: $D_2/D_1 = 0.1, 0.5, 5.0, 10.0$.

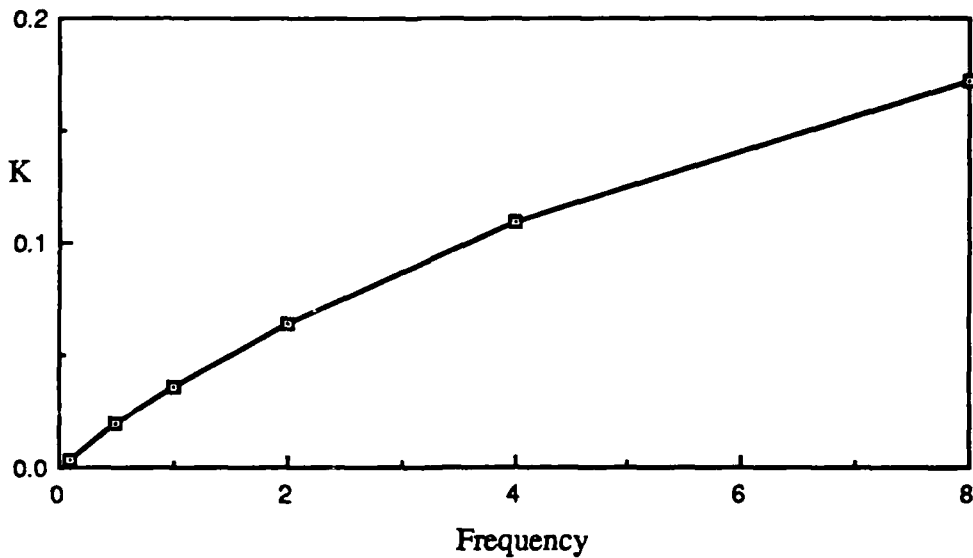
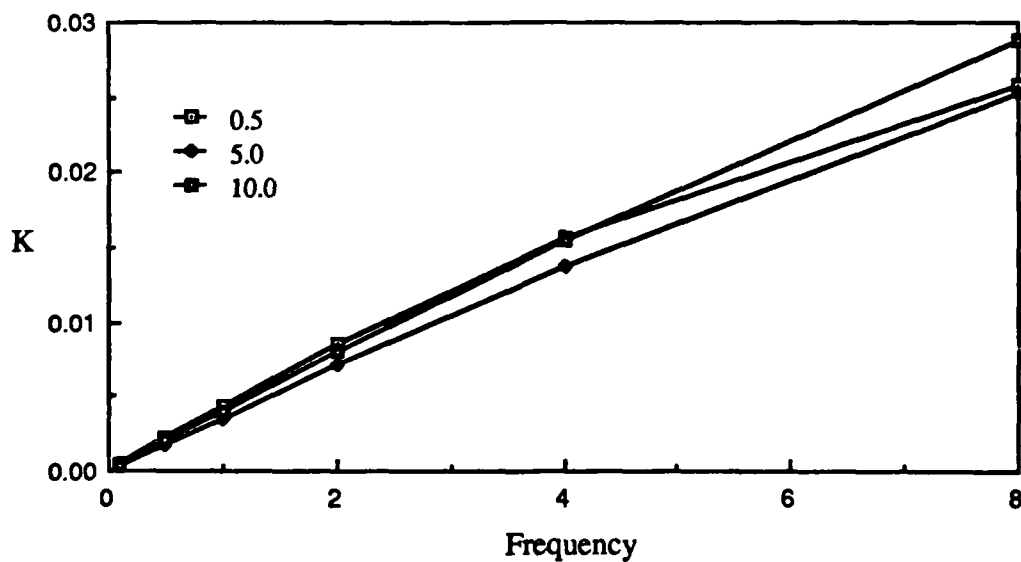
(a) $D_2/D_1=0.1$ (b) $D_2/D_1=0.5$, $D_2/D_1=5.0$, and $D_2/D_1=10.0$.

Figure 20. Stress intensity factor variation with frequency and diffusivity ratio.

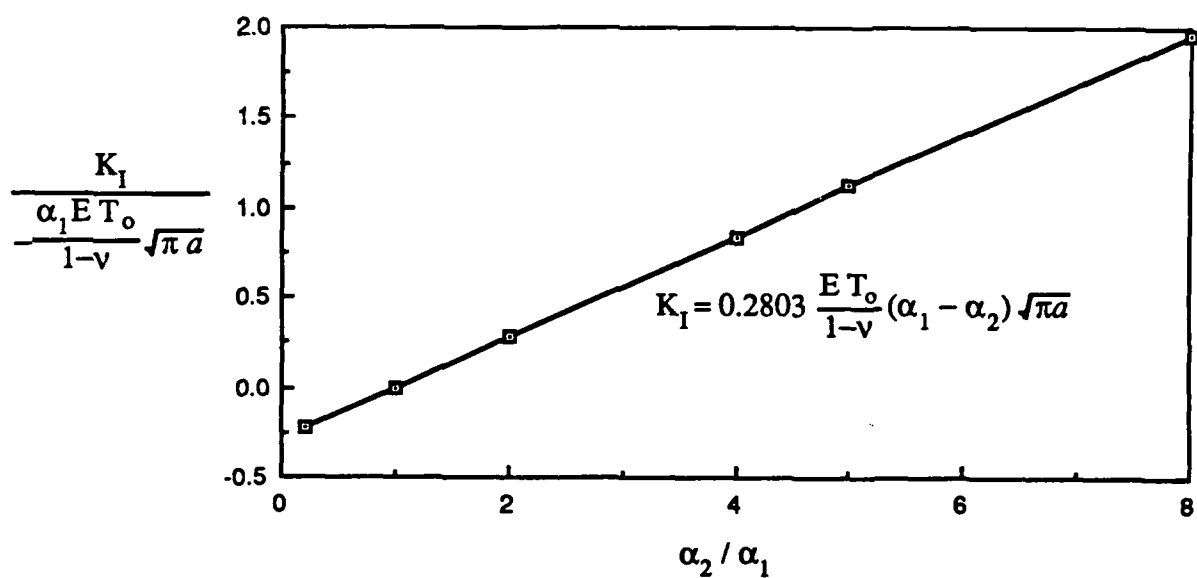


Figure 21. Stress intensity variation with expansion ratio for the degenerate case, $E_2 = E_1$.

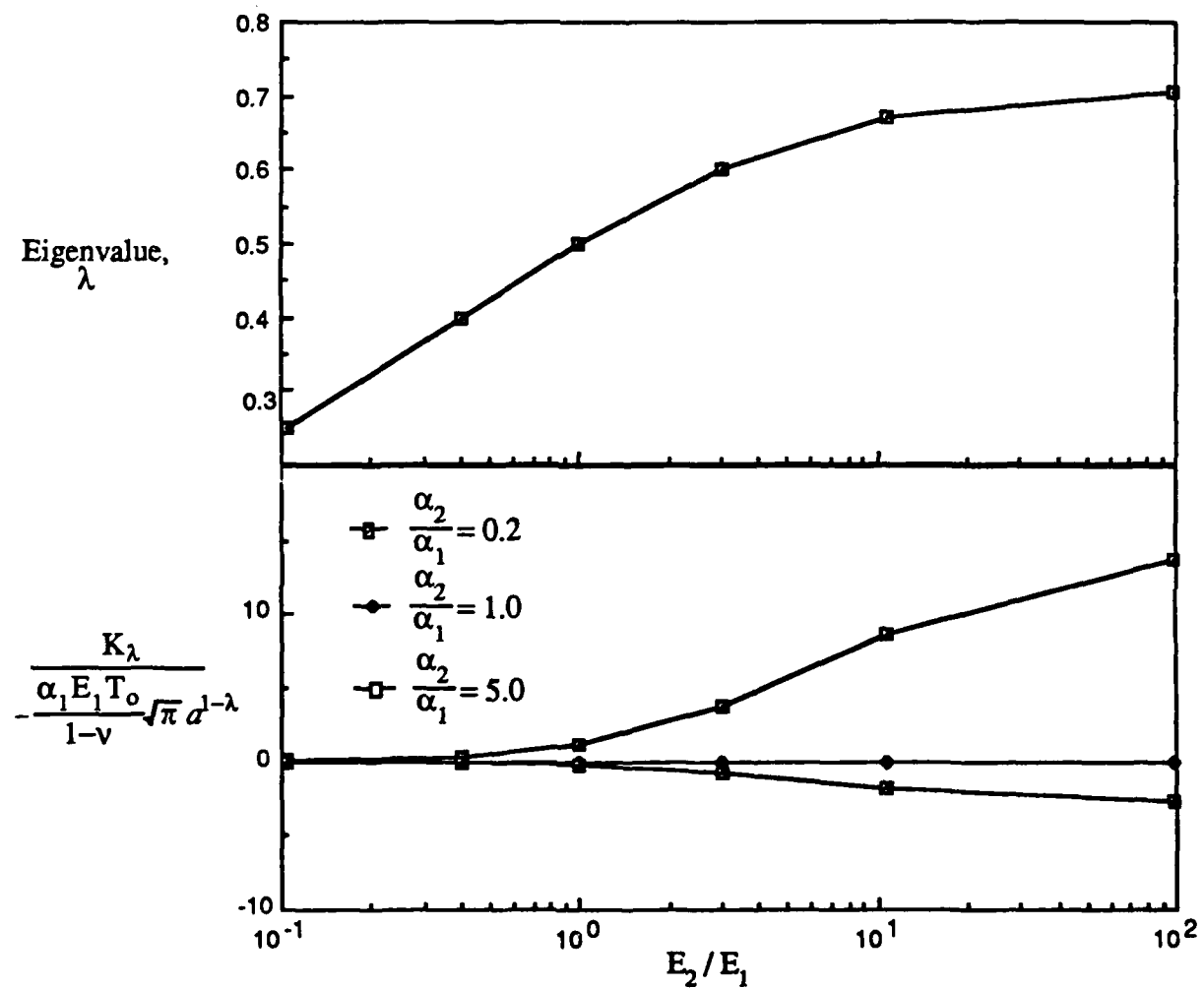


Figure 22. Variation of the stress intensity and eigenvalue with ratio of the elastic modulus.

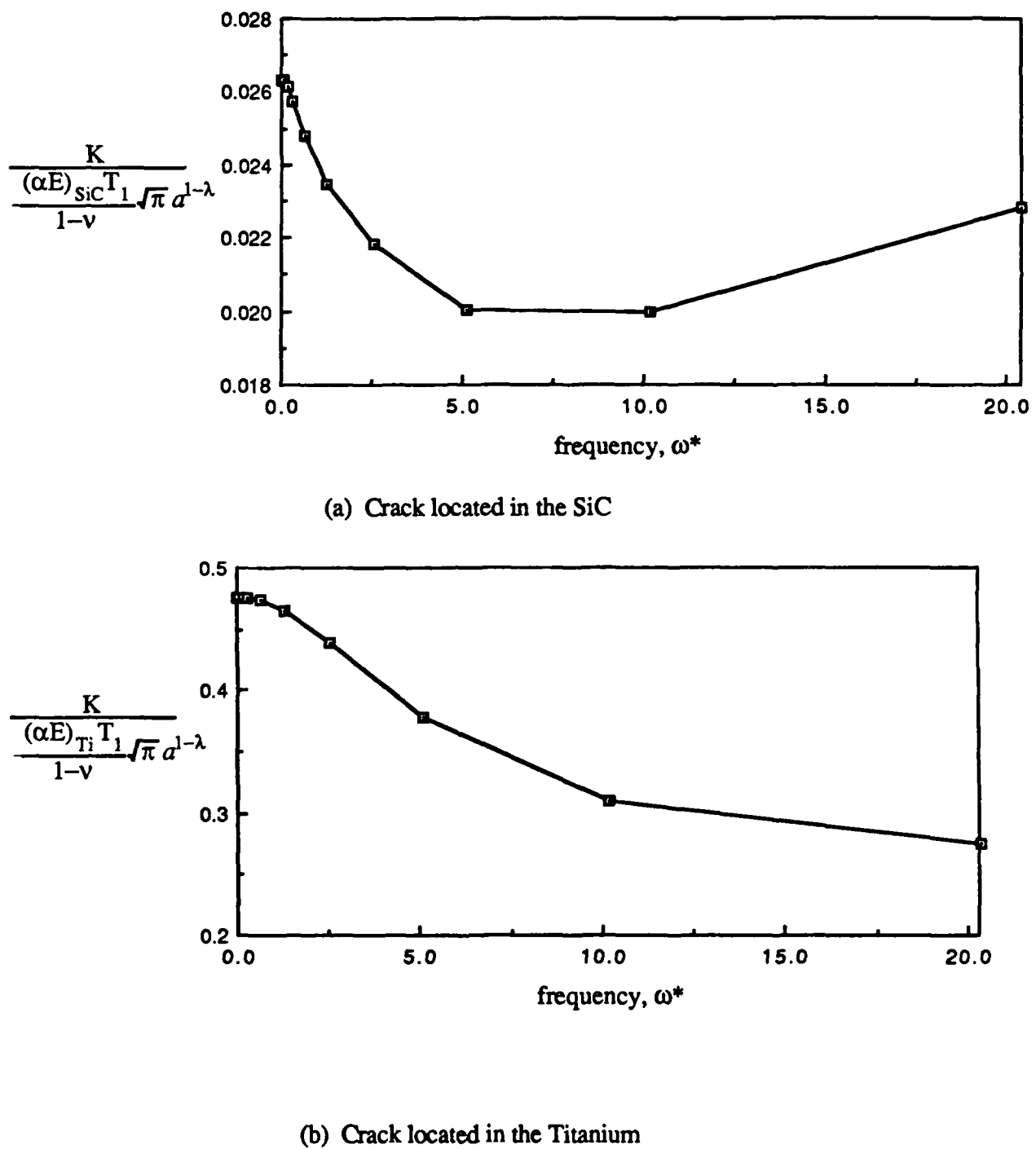


Figure 23. Stress intensity variation with frequency for composites of Titanium and SiC.

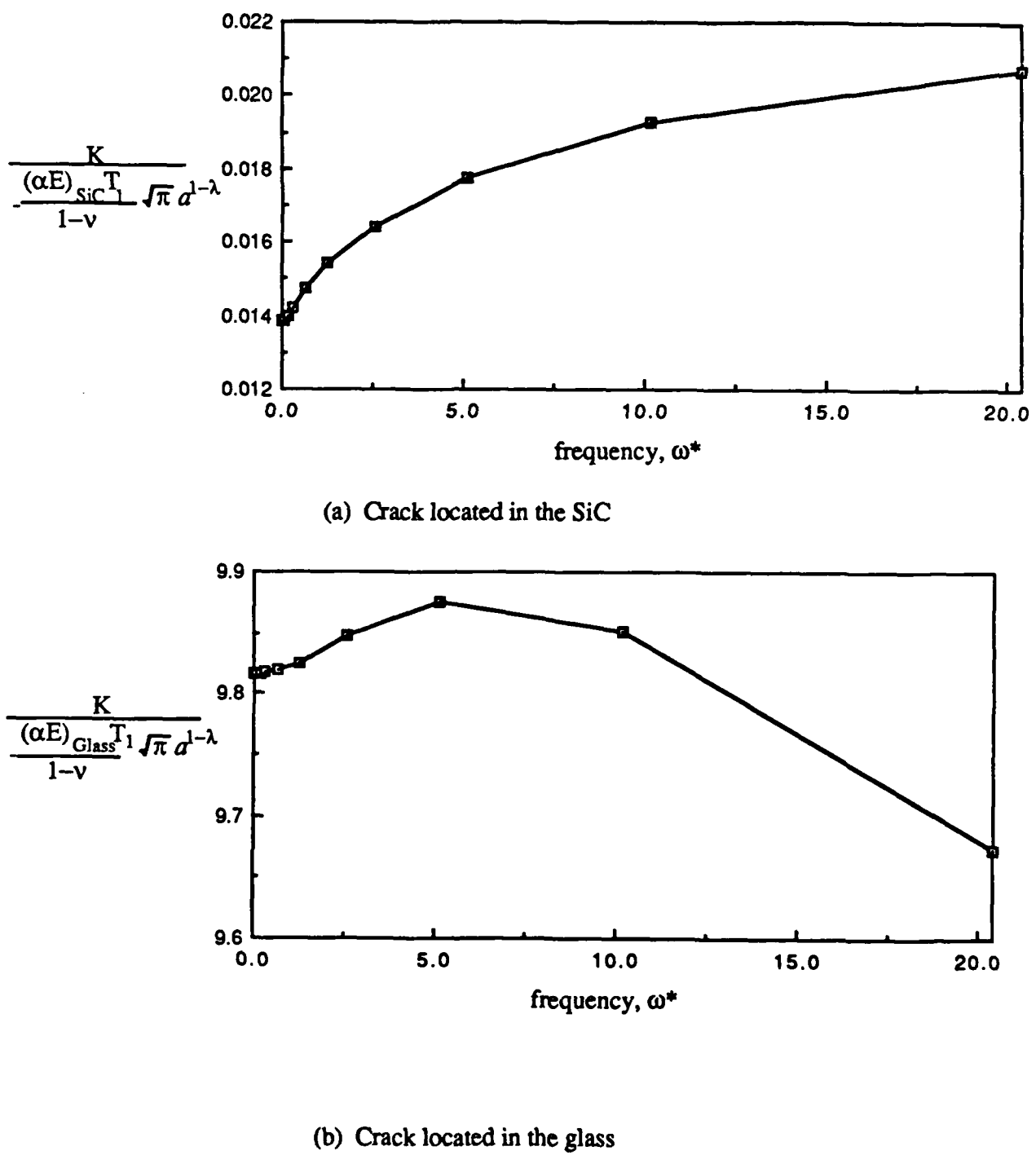


Figure 24. Stress intensity variation with frequency for composites of Glass and SiC.

VII. CONCLUSIONS AND RECOMMENDATIONS

In conclusion, we have shown that the mathematical techniques presented can be used to evaluate the stress intensity factors of components subjected to thermal fatigue. The applicability of the evaluation method has been demonstrated to be quite broad. Conditions of asymmetric temperature distributions, varying geometries and differing heat sources can be simulated through the use of this method. Because of the wide range of applicable conditions, it is possible that we can use these results in laboratory testing situations to approximate the contribution of the thermal fatigue loading in thermal mechanical fatigue. Further, we can extend this method to approximate stress intensities in composite materials. An example is the case of periodically occurring cracks in fibers of a bimaterial composite.

The results presented indicate that thermal fatigue loading has the potential to cause significant stress intensities in general cases of thermo-mechanical fatigue, and the method of electric resistance heating results in increasing stress intensity factors with frequency. These results are significant enough to warrant some experimental verification of these data. A much needed set of data is the temperature values (magnitude and phase) at near-crack and far-field locations, induced by both the electric resistance and hot lamp heating methods. With these values one could evaluate the magnitude of the stress intensities induced in actual applications.

REFERENCES

1. G. C. Sih, "On the Singular Character of Thermal Stresses near a Crack Tip," *Journal of Applied Mechanics*, **29**, 587-589 (1962).
2. A. L. Florence and J. N. Goodier, "Thermal Stresses due to Disturbance of Uniform Heat Flow by an Insulated Ovaloid Hole," *Journal of Applied Mechanics*, **27**, 635-639 (1960).
3. G. R. Irwin, "Fracture," in *Handbuch der Physik*, volume VI, S. Fluegge, ed., Springer-Verlag, 551-589 (1958).
4. M. L. Williams, "Stress Singularities Resulting from Various Boundary Conditions in Angular Corners of Plates in Extension," *Journal of Applied Mechanics*, **19**, 526-528 (1952).
5. Y. Konishi and A. Atsumi, "The Linear Thermoelastic Problem of Uniform Heat Flow Disturbed by a Two-Dimensional Crack in a Strip," *International Journal of Engineering Science*, **11**, 1-7 (1973).
6. H. Sekine, "Thermal Stress Singularities at Tips of a Crack in a Semi-infinite Medium under Uniform Heat Flow," *Engineering Fracture Mechanics*, **7**, 713-729 (1975).
7. H. Sekine, "Thermal Stresses near Tips of an Insulated Line Crack in a Semi-infinite Medium under Uniform Heat Flow," *Engineering Fracture Mechanics*, **9**, 499-507 (1977).
8. H. Sekine, "Crack Problem for a Semi-Infinite Solid with Heated Bounding Surface", *Journal of Applied Mechanics*, **44**, 637-642 (1977).
9. R. Shail, "Some Steady State Thermoelastic Stress Distributions in the Vicinity of an External Crack in an Infinite Solid," *International Journal of Engineering Science*, **6**, 685-694 (1968).
10. B. R. Das, "Some Axially Symmetric Thermal Stress Distributions in Elastic Solids Containing Cracks - I. An External Crack in an Infinite Solid," *International Journal of Engineering Science*, **9**, 469-478 (1971).

11. B. R. Das, "A Note on Thermal Stresses in a Long Circular Cylinder Containing a Penny-Shaped Crack," *International Journal of Engineering Science*, **7**, 667-676 (1969).
12. K. Herrmann and K. Kuemmerling, "A Crack-Thermal Stress Problem in a Doubly-Connected Solid," *Archives of Mechanics*, **28**, 171-188 (1976).
13. G. B. Sinclair, M. Okajima and J. H. Griffin, "Path Independent Integrals for Computing Stress Intensity Factors at Sharp Notches in Elastic Plates," *International Journal for Numerical Methods in Engineering.*, **20**, 999-1008 (1984).
14. M. E. Gurtin, "On a Path-Independent Integral for Thermoelasticity," *International Journal of Fracture*, **15**, R169-R170 (1979).
15. W. K. Wilson and I.-W. Yu, "The Use of the J-Integral in Thermal Crack Problems," *International Journal of Fracture*, **15**, 377-387 (1979).
16. S. Aoki, K. Kishimoto and M. Sakata, "Energy Release Rate in Elastic-Plastic Fracture Problems," *Journal of Applied Mechanics*, **48**, 825-829 (1981).
17. S. Aoki, K. Kishimoto and M. Sakata, "On the Path Independent Integral-J," *Engineering Fracture Mechanics*, **13**, 841-850 (1980).
18. S. Aoki, K. Kishimoto and M. Sakata, "Elastic-Plastic Analysis of Crack in Thermally Loaded Structures," *Engineering Fracture Mechanics*, **16**, 405-413 (1982).
19. A.-Y. Kuo and P. C. Riccadella, "Path-Independent Line Integrals for Steady-State, Two-Dimensional Thermoelasticity," *International Journal of Fracture*, **35**, 71-79 (1987).
20. Y. C. Fung, *Foundations of Solid Mechanics*, Prentice-Hall, Inc., p. 389 (1965).
21. D. A. Wilson and J. R. Warren, "Thermal Mechanical Crack Growth Rate of a High Strength Nickel Base Alloy," ASME Transactions, paper no. 85-GT-12, 30th International Gas Turbine Conference and Exhibit, Houston, TX, March 18-21, 1985.
22. F. B. Hildebrand, *Advanced Calculus for Applications*, 2nd Edition, Prentice-Hall, Inc., 484-490 (1976).
23. R. W. Hornbeck, *Numerical Methods*, Prentice-Hall, Inc., 148 (1975).

24. W. H. Press, B. P. Flannery, S. A. Teukolsky and W. T. Vetterling, *Numerical Recipes*, Cambridge University Press, 121-126 (1986).
25. W. H. Beyer, ed., *CRC Standard Mathematical Tables, 27th Edition*, CRC Press, Inc., 459 (1984).
26. H. Tada, P. C. Paris and G. R. Irwin, *The Stress Analysis of Cracks Handbook*, Del Research Corporation, Hellertown PA, p. 2.2 (1973).
27. N. Marchand, D. M. Parks and R. M. Pelloux, "K_I-solutions for Single Edge Notch Specimens under Fixed End Displacements," *International Journal of Fracture*, **31**, 53-65 (1986).
28. P. D. Hilton and G. C. Sih, "A Laminate Composite with a Crack Normal to the Interfaces," *International Journal for Solids and Structures*, **7**, 913-930 (1971).
29. T. S. Cook and F. Erdogan, "Stresses in Bonded Materials with a Crack Perpendicular to the Interface," *International Journal of Engineering Science*, **10**, 677-697 (1972).
30. G. D. Gupta, "A Layered Composite with a Broken Interface," *International Journal for Solids and Structures*, **9**, 1141-1154 (1973).
31. M. Okajima, *Analysis of Tensile Testing Configurations for Assessing the Strength of Butt Joints*, Ph. D Dissertation, Carnegie-Mellon University (1985).
32. J. P. Dempsey and G. B. Sinclair, "On the Singular Behavior at the Vertex of a Bimaterial Wedge," *Journal of Elasticity*, **11**, 317-327 (1981).
33. A. R. Zak and M. L. Williams, "Crack Point Stress Singularities in a Two-Material Wedge," *International Journal of Applied Mechanics*, **30**, 142-143 (1963).
34. L. G. Loitsyanskii, *Mechanics of Liquids and Gases*, Pergamon Press, 291-294 (1966).
35. S. E. Cunningham, J. H. Griffin and G. B. Sinclair, "On Stress Intensities Induced by Direct Resistance Heating," *International Journal of Fracture*, **33**, 135-144 (1987).

APPENDIX A

HEAT SOURCE INDUCED BY AN ELECTRIC CURRENT IN A CRACKED PLATE

Here we present the derivation of a heat source in a cracked plate induced by electric potential heating. The derivation follows the method of Loitsyanskii [34] who developed the solution to the analogous problem of irrotational flow of an incompressible fluid with no circulation flowing past an infinite cascade of plates (see Figure A1). The solution to the complex velocity of the fluid is derived in [34] and the main points are reiterated here. Upon integration of the velocity we acquire the complex potential of the fluid. The electric potential in the cracked plate is analogous to the real part of the complex potential. Once the real part of the complex potential is found, the heat source is obtained by taking the square of the gradient of the electric potential.

We consider the complex coordinate, $z=x+iy$. According to the geometry of Figure A1, the edges of the plates which impede fluid flow are located at positions in the complex plane:

$$z = a \pm 2kW, \quad z = -a \pm 2kW, \quad k = 0, 1, 2, \dots \quad (\text{A1})$$

We know the complex velocity of flow past a single plate in an infinite medium is

$$V(z) = u_{\infty} - i v_{\infty} \frac{z}{\sqrt{z^2 - a^2}} \quad (\text{A2})$$

where u_{∞} and v_{∞} are the far-field components of the applied velocity in the x and y directions, respectively.

If there are $2k + 1$ plates, then z in the numerator of (A2) is replaced by the product

$$\prod_{k=-k}^{k} (z + 2kW) = z \prod_{k=1}^{k} (z^2 - 4k^2 W^2) \quad (\text{A3})$$

Replacing similar expressions for $(z+a)$ and $(z-a)$ in the denominator, taking the limit as $\kappa \rightarrow \infty$, and considering the identity

$$\lim_{\kappa \rightarrow \infty} \frac{\pi}{2W} z \prod_{k=1}^{\kappa} \left[1 - \left(\frac{\pi z}{2W} \right)^2 - \frac{1}{k^2 \pi^2} \right] = \sin \frac{\pi z}{2W} \quad (A4)$$

gives the resulting complex velocity of fluid flowing around an infinite cascade of plates:

$$V(z) = u_{\infty} - i v_{\infty} \frac{\sin \frac{\pi z}{2W}}{\sqrt{\cos^2 \frac{\pi a}{2W} - \cos^2 \frac{\pi z}{2W}}} \quad (A5)$$

The complex potential, $\Phi(z)$, is obtained by integrating the complex velocity:

$$\Phi(z) = \int V(z) dz = u_{\infty} z - \frac{2W}{\pi} v_{\infty} \log \left[\cos \frac{\pi z}{2W} + \sqrt{\cos^2 \frac{\pi z}{2W} - \cos^2 \frac{\pi a}{2W}} \right] + C \quad (A6)$$

We take the constant of integration to be zero without loss of generality.

The complex potential can be written as the sum of real and imaginary parts which represent the velocity potential and stream function, respectively:

$$\Phi(z) = \phi(x,y) + i \psi(x,y) \quad (A7)$$

In the electric potential analog to the flow problem, the velocity potential, ϕ , is the electric potential and $\mathbf{I} = -\nabla \phi/\rho$ (where ρ is the electrical resistivity) is the current. The electric potential, then, is obtained by finding the real part of Equation (A6) when the far-field velocity components are replaced by the potential drop, ϕ_0 , across the plate length. If the current flow is assumed normal to the crack this gives $u_{\infty} = 0$ and $v_{\infty} = \phi_0/2L$.

$$\phi(x,y) = \frac{2W}{\pi} \frac{\phi_0}{2L} \operatorname{Re} \left[\log \left(\cos \frac{\pi z}{2W} + \sqrt{\cos^2 \frac{\pi z}{2W} - \cos^2 \frac{\pi a}{2W}} \right) \right] \quad (A8)$$

Obtaining the real part of the above expression requires some algebra. We write

$$Z = \cos \frac{\pi z}{2W} + \sqrt{\cos^2 \frac{\pi z}{2W} - \cos^2 \frac{\pi a}{2W}} = Re^{i\Theta} \quad (A9)$$

Then

$$\log(Z) = \ln R + i\Theta \quad (A10)$$

To find R, we invoke the trigonometric identity,

$$\cos \frac{\pi z}{2W} = \cos \frac{\pi x}{2W} \cosh \frac{\pi y}{2W} - i \sin \frac{\pi x}{2W} \sinh \frac{\pi y}{2W} = \alpha - i\beta \quad (A11)$$

where α and β are introduced for brevity. In addition, we introduce α_0 :

$$\cos \frac{\pi a}{2W} = \alpha_0 \quad (A12)$$

Then

$$Z = \alpha - i\beta + \sqrt{(\alpha - i\beta)^2 - \alpha_0^2} \quad (A13)$$

Letting

$$\xi e^{i\eta} = (\alpha - i\beta)^2 - \alpha_0^2 \quad (A14)$$

then the square root portion of (A13) is equal to $\pm \sqrt{\xi} e^{i\eta/2}$, for

$$\xi = \sqrt{(\alpha^2 - \beta^2 - \alpha_0^2)^2 + 4\alpha^2\beta^2}, \quad \eta = \arctan \frac{-2\alpha\beta}{\alpha^2 - \beta^2 - \alpha_0^2} \quad (A15)$$

Combining these expressions gives

$$Z = \alpha - i\beta \pm \sqrt{\xi} e^{i\eta/2} = R e^{i\theta} \quad (A16)$$

Since R^2 is equivalent to the sum of the squares of the real and imaginary parts of Z , $\ln(R)$ is equal to

$$\ln(R) = \frac{1}{2} \ln \left\{ [\operatorname{Re}(Z)]^2 + [\operatorname{Im}(Z)]^2 \right\} \quad (A17)$$

where

$$\operatorname{Re}(Z) = \alpha \pm \sqrt{\xi} \cos \frac{\eta}{2} \quad (A18)$$

and

$$\operatorname{Im}(Z) = -\beta \pm \sqrt{\xi} \sin \frac{\eta}{2} \quad (A19)$$

Thus, the electric potential solution is given by:

$$\phi = \frac{W}{\pi} \frac{\phi_0}{2L} \ln \left[\alpha^2 + \beta^2 + \xi \pm 2\sqrt{\xi} (\alpha \cos \frac{\eta}{2} - \beta \sin \frac{\eta}{2}) \right] \quad (A20)$$

The plus sign in \pm gives solutions for positive y (+) while the minus sign results in solutions for negative y (-), the solution being symmetric about the y -axis.

We obtain the heat source term in the heat conduction equation by taking the square of the gradient of the electric potential and multiplying by the electrical conductivity and dividing by thermal conductivity:

$$h(x,y) = \frac{\sigma}{k} (\nabla \phi \cdot \nabla \phi) = \frac{\sigma}{k} \left[\left(\frac{\partial \phi}{\partial x} \right)^2 + \left(\frac{\partial \phi}{\partial y} \right)^2 \right] \quad (A21)$$

We express the partial derivatives in closed form and compute the heat source with the aid of a computer for specific points. Near the crack tip, the heat source behaves asymptotically as $1/r$ where r is the distance from the tip of the crack. Consistent with the condition that the complex velocity approaches a constant velocity in the far-field, the heat source also approaches a constant value at far-field points.

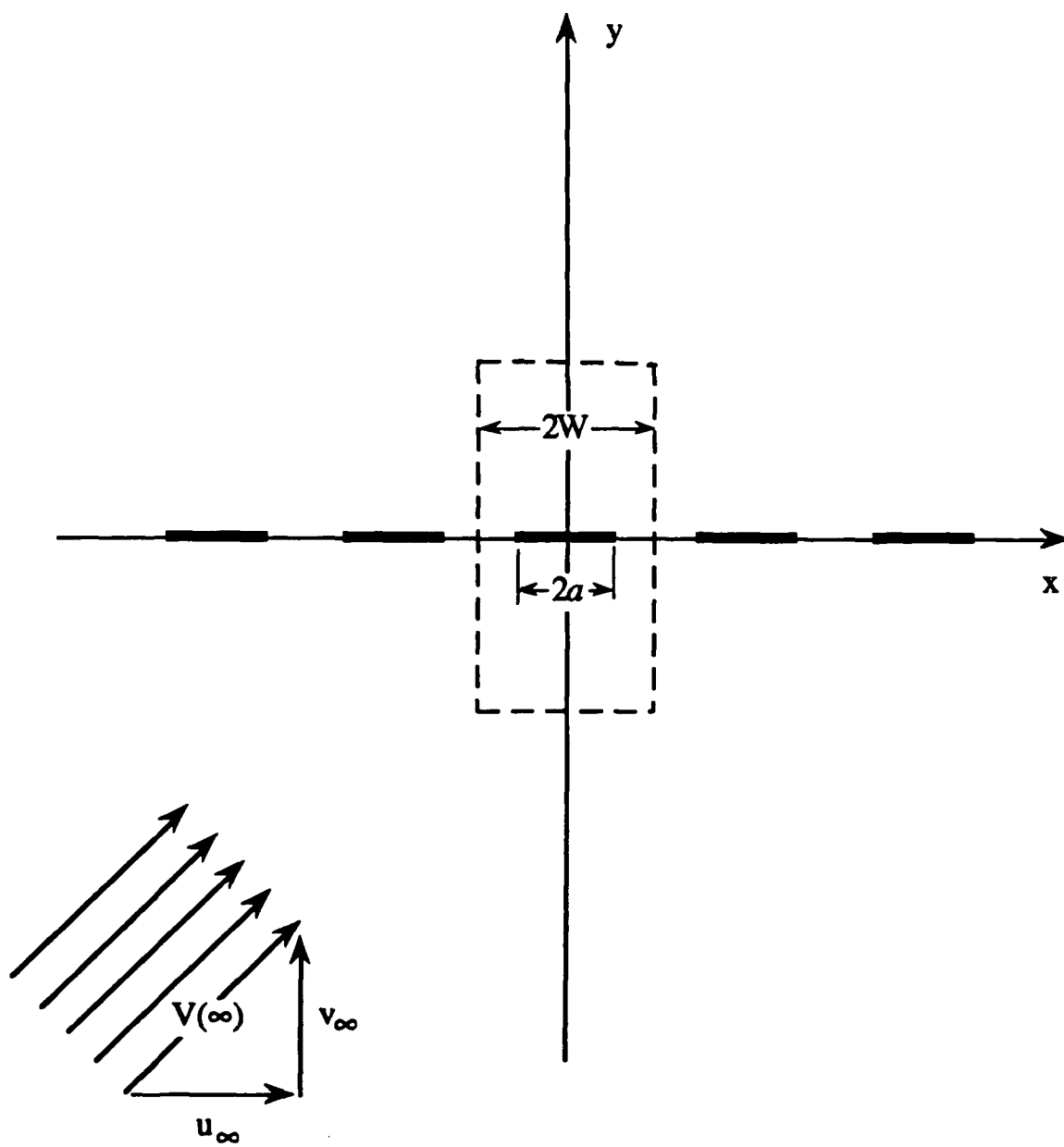


Figure A1. Flow past an infinite cascade of plates

APPENDIX B

GRIDS FOR FINITE ELEMENT ANALYSIS

Here we present the grids used in the finite element analysis. The number of elements and degrees of freedom for the homogeneous grids are listed in Table B1. Figures B1 through B3 illustrate the grids used in the homogeneous problems. Table B2 lists the number of elements and degrees of freedom for the grids used in the composite analysis and the grids are illustrated in Figures B4 through B6.

Table B1
Finite element grids for the homogeneous problems.

Grid	Number of elements	Degrees of freedom
coarse	72	182
medium	288	750
fine	720	1562

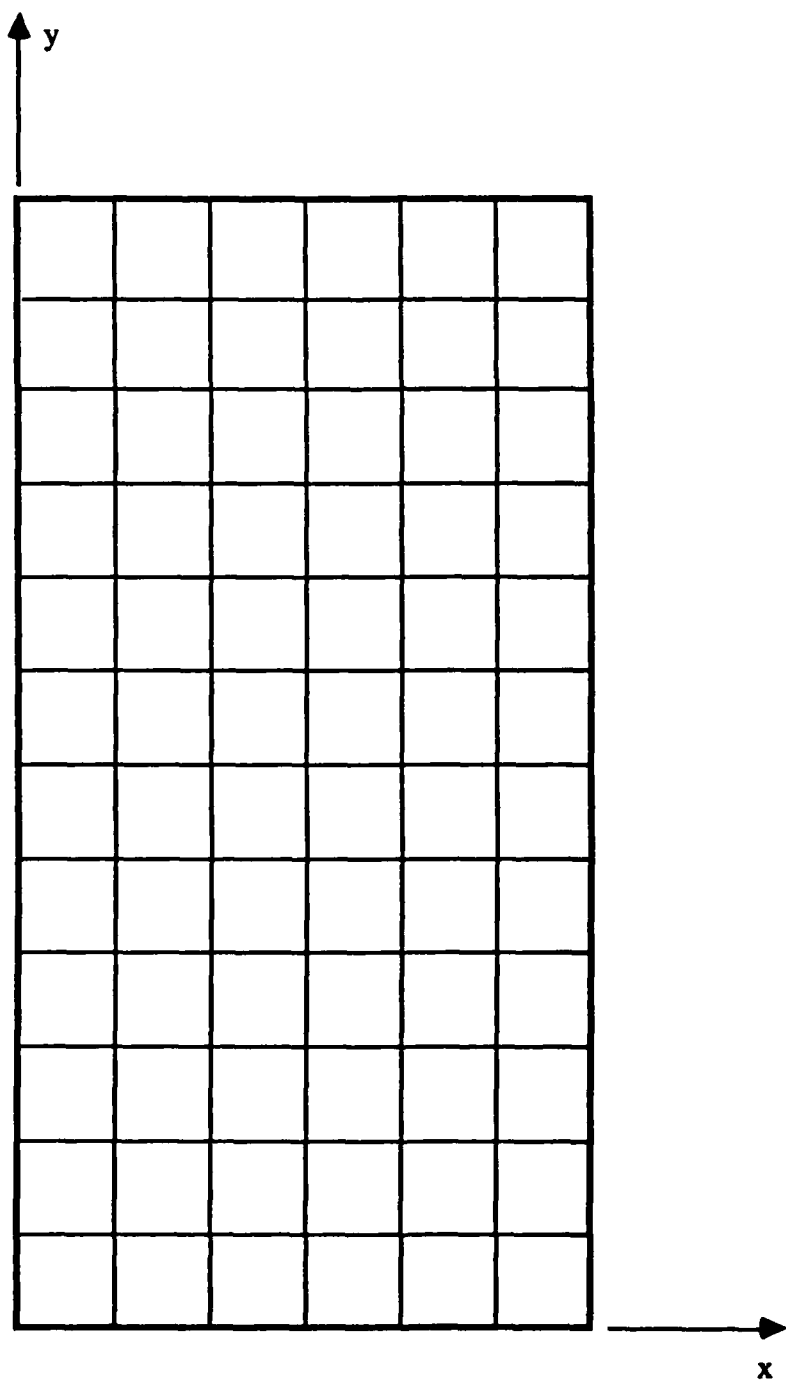


Figure B1. Finite element grid for homogeneous stress analysis, coarse.

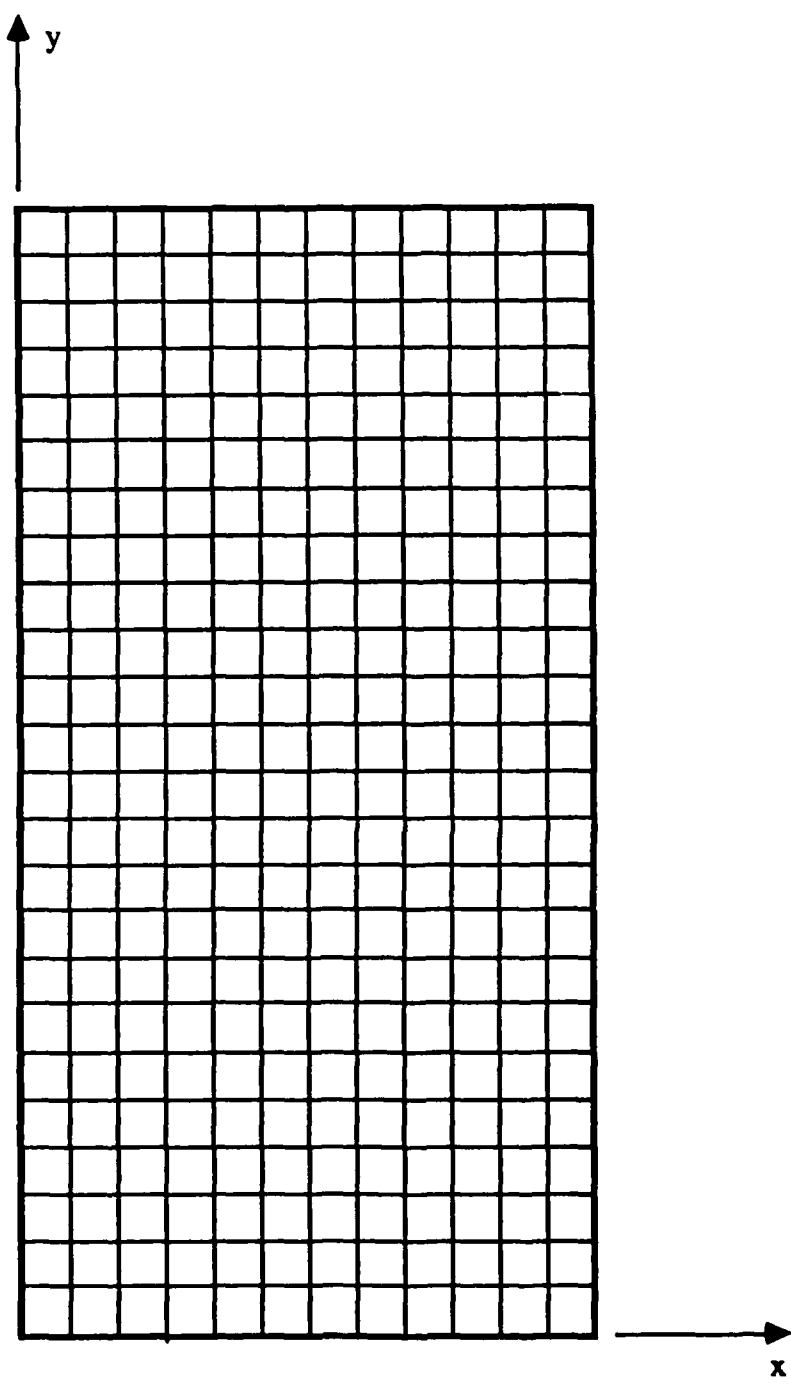


Figure B2. Finite element grid for homogeneous stress analysis, medium.

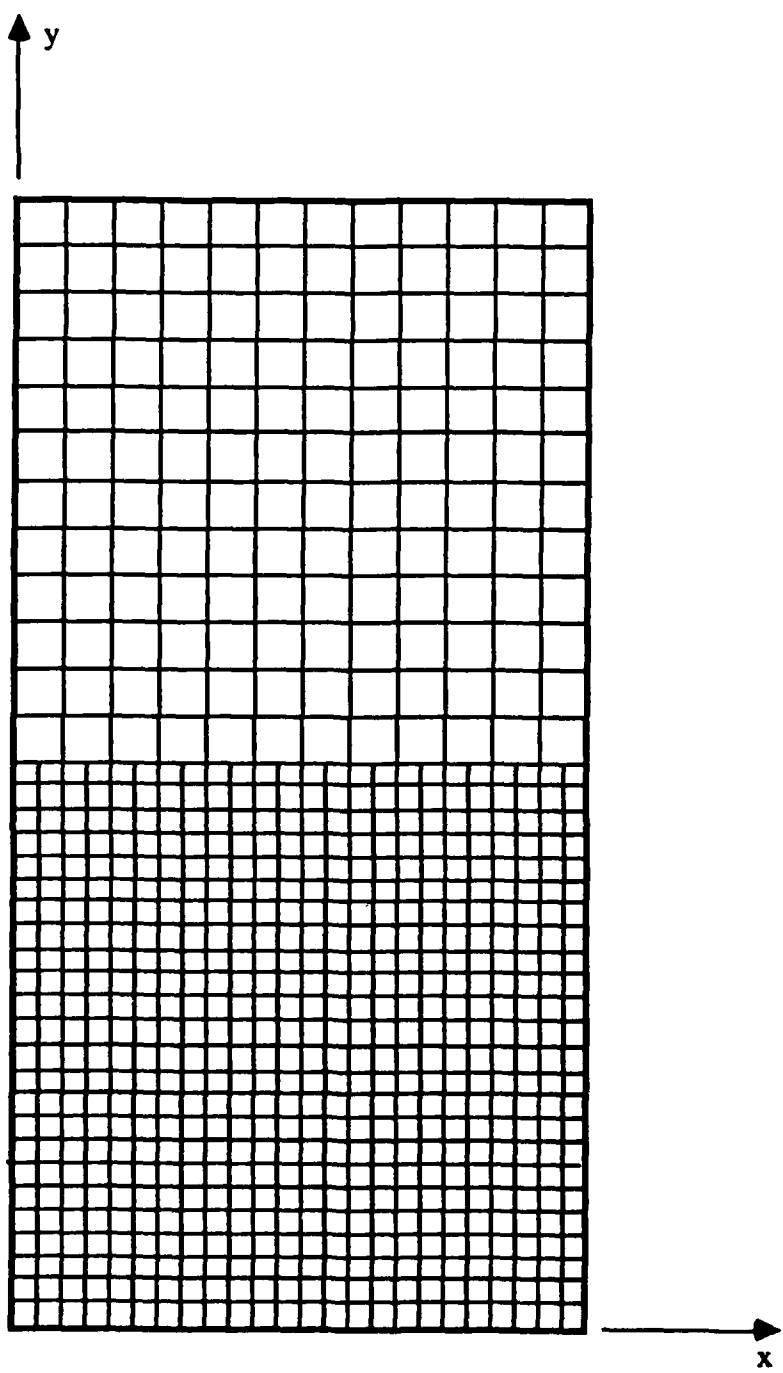


Figure B3. Finite element grid for homogeneous stress analysis, fine.

Table B2
Finite element grids for the composite problems.

Grid	Number of elements	Degrees of freedom
coarse	64	162
medium	256	578
fine	352	794

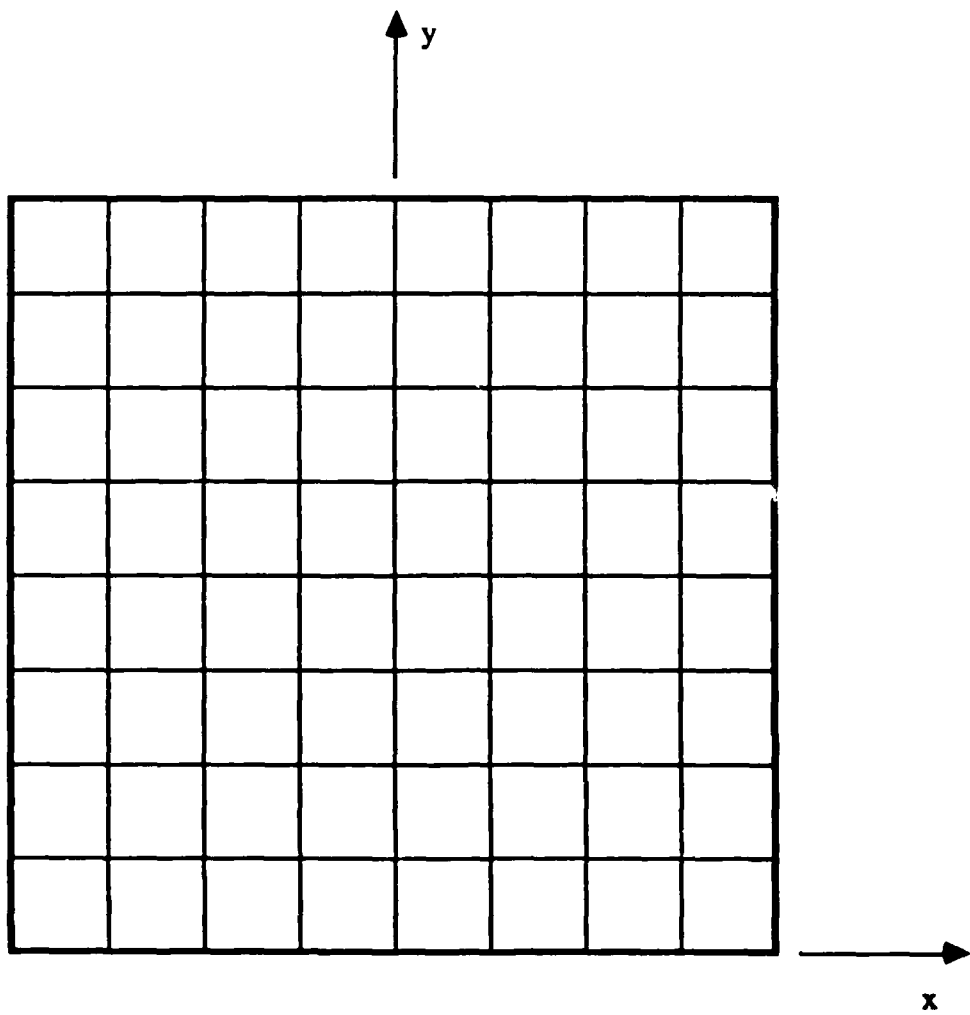


Figure B4. Finite element grid for composite analysis, coarse.

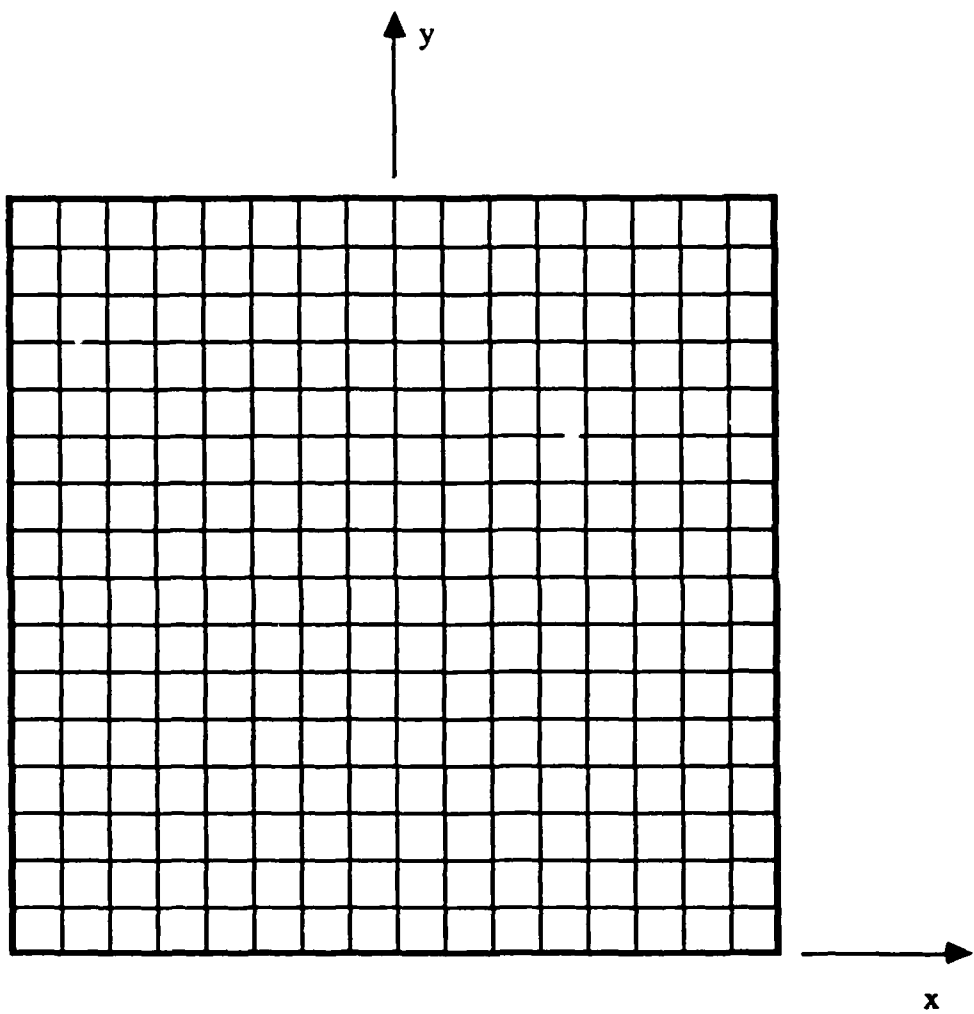


Figure B5. Finite element grid for composite analysis, medium.

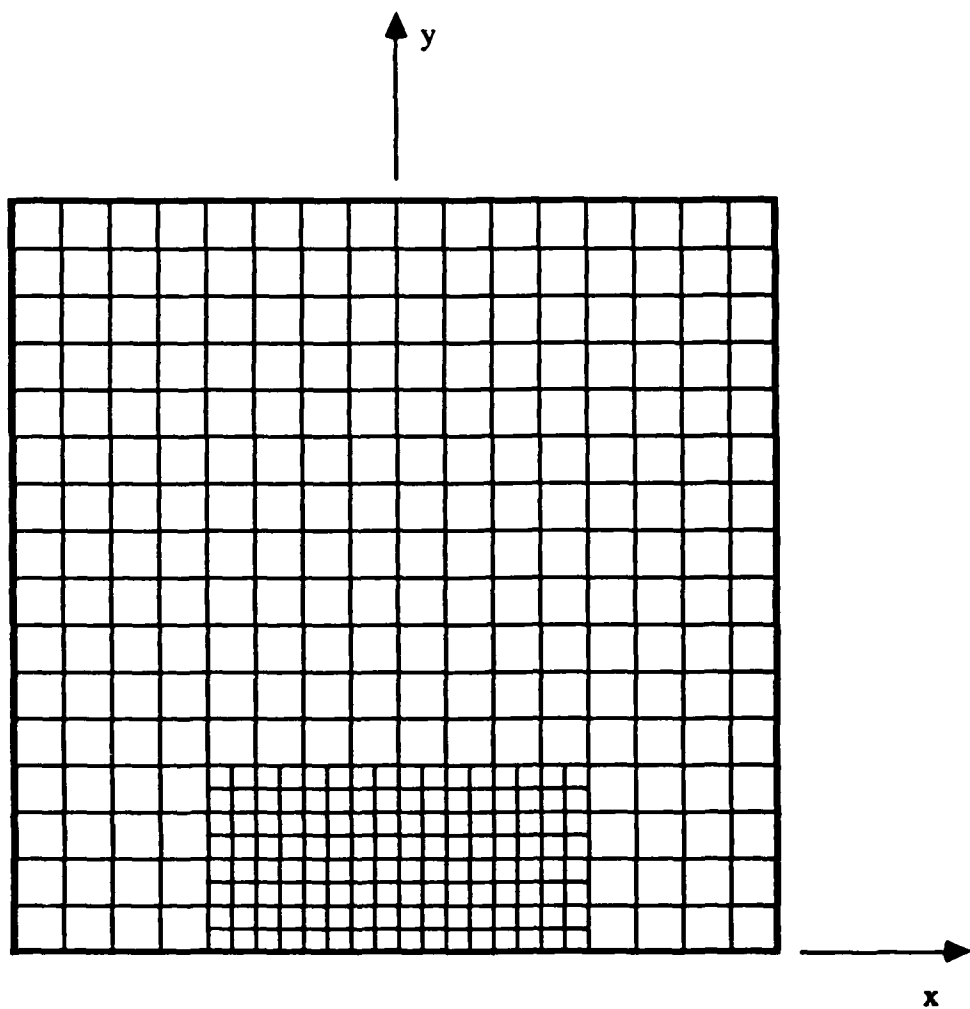


Figure B6. Finite element grid for composite analysis, fine.

APPENDIX C

COMPLEMENTARY EIGENFUNCTIONS FOR A CRACK.

Here we present the complementary eigenfunctions for the crack in an elastic plane. The eigenfunctions, established in polar co-ordinates with the origin at the crack tip, are taken from Sinclair et al. [13] and are specialized to the crack geometry. The symmetric forms are:

$$\sigma_{rr}^* = \frac{\mu}{\sqrt{2\pi}(1+\kappa)} r^{-3/2} \left[\frac{7}{2} \cos \frac{3}{2}\theta - \frac{3}{2} \cos \frac{\theta}{2} \right]$$

$$\sigma_{\theta\theta}^* = \frac{-\mu}{\sqrt{2\pi}(1+\kappa)} r^{-3/2} \left[\frac{1}{2} \cos \frac{3}{2}\theta - \frac{3}{2} \cos \frac{\theta}{2} \right]$$

$$\tau_{r\theta}^* = \frac{\mu}{\sqrt{2\pi}(1+\kappa)} r^{-3/2} \left[\frac{3}{2} \sin \frac{3}{2}\theta + \frac{3}{2} \sin \frac{\theta}{2} \right]$$

$$u_r^* = \frac{-r^{1/2}}{\sqrt{2\pi}(1+\kappa)} \left[\left(\frac{1}{2} + \kappa \right) \cos \frac{3}{2}\theta - \frac{3}{2} \cos \frac{\theta}{2} \right]$$

$$u_\theta^* = \frac{-r^{1/2}}{\sqrt{2\pi}(1+\kappa)} \left[\left(\frac{1}{2} - \kappa \right) \sin \frac{3}{2}\theta + \frac{3}{2} \sin \frac{\theta}{2} \right]$$

The antisymmetric complementary fields are given by:

$$\sigma_{rr}^* = \frac{\mu}{\sqrt{2\pi}(1+\kappa)} r^{-3/2} \left[\frac{1}{2} \sin \frac{\theta}{2} - \frac{7}{2} \sin \frac{3}{2}\theta \right]$$

$$\sigma_{\theta\theta}^* = \frac{-\mu}{\sqrt{2\pi}(1+\kappa)} r^{-3/2} \left[\frac{1}{2} \sin \frac{\theta}{2} + \frac{1}{2} \sin \frac{3}{2}\theta \right]$$

$$\tau_{r\theta}^* = \frac{\mu}{\sqrt{2\pi}(1+\kappa)} r^{-3/2} \left[\frac{1}{2} \cos \frac{\theta}{2} + \frac{3}{2} \cos \frac{3}{2}\theta \right]$$

$$u_r^* = \frac{-r^{1/2}}{\sqrt{2\pi} (1+\kappa)} \left[\frac{1}{2} \sin \frac{\theta}{2} - \left(\frac{1}{2} + \kappa \right) \sin \frac{3}{2}\theta \right]$$

$$u_\theta^* = \frac{-r^{1/2}}{\sqrt{2\pi} (1+\kappa)} \left[\frac{1}{2} \cos \frac{\theta}{2} + \left(\frac{1}{2} - \kappa \right) \cos \frac{3}{2}\theta \right]$$

where

$$\kappa = 3 - 4v$$

in plane strain, and

$$\kappa = \frac{3-v}{1+v}$$

in plane stress.

APPENDIX D
WEIGHTS AND ABSCISSAS FOR THE GAUSS-TYPE QUADRATURE

$$\int_0^1 \frac{f(x)}{\sqrt{x}} dx = \sum_{i=1}^n w_i f(x_i)$$

	i	x_i	w_i
n=1	1	0.333333333333	2.000000000000
n=2	1	0.115587109997	1.304290309725
	2	0.741555747146	0.695709690275
n=3	1	0.056939115967	0.935827869145
	2	0.437197852751	0.721523146096
	3	0.869499394918	0.342648984758
n=4	1	0.033648268067	0.725367566757
	2	0.276184313872	0.627413291756
	3	0.634677476235	0.444762068907
	4	0.922156608492	0.202457072581
n=5	1	0.022163568807	0.591048449430
	2	0.187831567652	0.538533438620
	3	0.461597361496	0.438172725032
	4	0.748334628387	0.298902698301
	5	0.948493926288	0.133342688617
n=6	1	0.015683406607	0.498294091627
	2	0.135300011655	0.466985073077
	3	0.344942379427	0.406334853446
	4	0.592750127732	0.320156657087
	5	0.817428013267	0.213878651991
	6	0.963461278703	0.094350672773
n=8	1	0.009027377026	0.378901220910
	2	0.079300559811	0.365206830090
	3	0.209779368616	0.338313038790
	4	0.381771053397	0.299191977633
	5	0.570635820162	0.249257942511
	6	0.749317378547	0.190317023365
	7	0.892221974214	0.124507047877
	8	0.978914210162	0.054304918824

n=10	1	0.005856308437	0.305506774261
	2	0.051886393980	0.298345972945
	3	0.139656240743	0.284192218637
	4	0.260985093682	0.263377276898
	5	0.404564284766	0.236389063923
	6	0.557011314600	0.203860239634
	7	0.704117292400	0.166553483153
	8	0.832171652087	0.125344096668
	9	0.929241876580	0.081202859601
	10	0.986304414519	0.035228014278
n=12	1	0.004103285523	0.255876390693
	2	0.036526421504	0.251674912694
	3	0.099251890030	0.243340945856
	4	0.188176807259	0.231011336107
	5	0.297484581452	0.214888540232
	6	0.420025381681	0.195237304208
	7	0.547783818960	0.172380323064
	8	0.672403257001	0.146692962822
	9	0.785732486514	0.118597169831
	10	0.880359134936	0.088554877635
	11	0.950095757826	0.057062777258
	12	0.990397602845	0.024682459600
n=16	1	0.002333630564	0.193080177029
	2	0.020872147684	0.191277440159
	3	0.057258441734	0.187688798162
	4	0.110136769181	0.182347757392
	5	0.177536897897	0.175304186009
	6	0.256947517675	0.166623848454
	7	0.345409811309	0.156387791574
	8	0.439627699909	0.144691588218
	9	0.536090655003	0.131644445553
	10	0.631204502056	0.117368186957
	11	0.721425343258	0.101996118525
	12	0.803391614274	0.085671796045
	13	0.874049370825	0.068547725826
	14	0.930766209806	0.050784130618
	15	0.971430051691	0.032548789462
	16	0.994535210151	0.014037220019
n=24	1	0.001048475472	0.129475393625
	2	0.009409911669	0.128932328872
	3	0.025992648096	0.127848477169
	4	0.050518761473	0.126228384573
	5	0.082577199139	0.124078846320
	6	0.121630668223	0.121408878332
	7	0.167024640562	0.118229679397
	8	0.217998322465	0.114554584201
	9	0.273697405472	0.110399007400
	10	0.333188384403	0.105780378970

	11	0.395474202728	0.100718071108
	12	0.459510963069	0.095233316985
	13	0.524225422743	0.089349121713
	14	0.588532981170	0.083090165887
	15	0.651355857686	0.076482702132
	16	0.711641155150	0.069554445130
	17	0.768378506728	0.062334455666
	18	0.820617010337	0.054853019417
	19	0.867481167625	0.047141521679
	20	0.908185562375	0.039232320915
	21	0.942048039521	0.031158631446
	22	0.968501196288	0.022954469158
	23	0.987102203204	0.014655107803
	24	0.997543524928	0.006306692105
<i>n=48</i>			
	1	0.000264932423	0.065101228985
	2	0.002382707518	0.065032237428
	3	0.006609282769	0.064894327428
	4	0.012926746332	0.064687645137
	5	0.021308325370	0.064412409588
	6	0.031718499509	0.064068912464
	7	0.044113151374	0.063657517789
	8	0.058439753552	0.063178661542
	9	0.074637591201	0.062632851194
	10	0.092638019352	0.062020665173
	11	0.112364753820	0.061342752247
	12	0.133734194491	0.060599830842
	13	0.156655779610	0.059792688273
	14	0.181032369576	0.058922179916
	15	0.206760658608	0.057989228301
	16	0.233731612547	0.056994822130
	17	0.261830930934	0.055940015234
	18	0.290939531402	0.054825925452
	19	0.320934054339	0.053653733451
	20	0.351687385674	0.052424681471
	21	0.383069195575	0.051140072011
	22	0.414946490776	0.049801266445
	23	0.447184178188	0.048409683585
	24	0.479645637414	0.046966798172
	25	0.512193299734	0.045474139317
	26	0.544689231106	0.043933288878
	27	0.576995716721	0.042345879784
	28	0.608975844627	0.040713594309
	29	0.640494085946	0.039038162280
	30	0.671416869237	0.037321359255
	31	0.701613146562	0.035565004632
	32	0.730954948851	0.033770959729
	33	0.759317928231	0.031941125805
	34	0.786581884998	0.030077442054
	35	0.812631277024	0.028181883545
	36	0.837355709413	0.026256459134
	37	0.860650402358	0.024303209342

38	0.882416635207	0.022324204200
39	0.902562164861	0.020321541070
40	0.921001616744	0.018297342462
41	0.937656846722	0.016253753851
42	0.952457272490	0.014192941582
43	0.965340173199	0.012117091008
44	0.976250956557	0.010028405486
45	0.985143394070	0.007929108677
46	0.991979831560	0.005821463636
47	0.996731426993	0.003707921578
48	0.999379104174	0.001593584131